

UNIVERSITÉ DE LILLE

Doctoral School **ED ENGSYS-632**

University Department **Unité de Mécanique de Lille - Joseph Boussinesq ULR 7512**

Thesis defended by **Michael MAALOULY**

Defended on **December 6, 2024**

In order to become Doctor from Université de Lille

Academic Field **Fluid Mechanics**

Lagrangian Particle Dynamics in Ocean Submesoscale Turbulence

Thesis supervised by Stefano BERTI
Gilmar MOMPEAN

Committee members

<i>Referees</i>	Basile GALLET	Director of Research at CEA Saclay
	Ivana VINKOVIC	Professor at Université Claude Bernard Lyon 1
<i>Examiners</i>	Cristóbal LÓPEZ	Professor at Universitat de les Illes Balears
	Martín OBLIGADO	Professor at Centrale Lille
<i>Supervisors</i>	Stefano BERTI	HDR Associate Professor at Université de Lille
	Gilmar MOMPEAN	Professor at Université de Lille

UNIVERSITÉ DE LILLE

École doctorale ED ENGSYS-632

Unité de recherche Unité de Mécanique de Lille - Joseph Boussinesq ULR 7512

Thèse présentée par Michael MAALOULY

Soutenue le 6 décembre 2024

En vue de l'obtention du grade de docteur de l'Université de Lille

Discipline Mécanique des Milieux Fluides

Dynamique lagrangienne dans la turbulence océanique à sous-mésoéchelle

Thèse dirigée par Stefano BERTI
Gilmar MOMPEAN

Composition du jury

<i>Rapporteurs</i>	Basile GALLET Ivana VINKOVIC	directeur de recherche au CEA Saclay professeure à l'Université Claude Bernard Lyon 1
<i>Examineurs</i>	Cristóbal LÓPEZ Martín OBLIGADO	professeur à l'Universitat de les Illes Balears professeur à Centrale Lille
<i>Directeurs de thèse</i>	Stefano BERTI Gilmar MOMPEAN	MCF HDR à l'Université de Lille professeur à l'Université de Lille

This thesis has been prepared at

Unité de Mécanique de Lille - Joseph Boussinesq ULR 7512

Polytech' Lille, Bâtiment ESPRIT
Avenue Paul Langevin
59650 Villeneuve-d'Ascq
France

Web Site <https://uml.univ-lille.fr>



To my parents, Elizabeth and Antoun.

To My siblings, Rony, Rina, and Maya.

I also dedicate this work to all those who have supported me throughout this journey.

LAGRANGIAN PARTICLE DYNAMICS IN OCEAN SUBMESOSCALE TURBULENCE**Abstract**

Turbulent flows at the ocean surface deviate from geostrophic equilibrium at scales smaller than 10 km, which are important for vertical transport, heat distribution, and plankton dynamics. Although measuring velocity fields at these small scales is challenging, new high-resolution satellite altimetry is beginning to detect them. However, since the satellite-derived velocities primarily represent the geostrophic flow component, understanding the influence of unresolved ageostrophic motions on particle dispersion is essential for accurately characterizing Lagrangian transport properties. This study uses numerical simulations to explore fine-scale ocean turbulence with a model accounting for ageostrophic corrections based on a Rossby-number expansion of the primitive equations, reducing to the surface quasi-geostrophic model at zero Rossby numbers. Additionally, we analyze Lagrangian particle trajectories using LLC4320 velocity fields, a high-resolution general circulation model that captures both low- and high-frequency ocean processes. First, we examine the effect of ageostrophic dynamics on the pair-dispersion and clustering properties of Lagrangian tracer particles for varying Rossby numbers. The results show that while long-term pair separation is weakly affected by ageostrophic motions, these motions drive temporary particle aggregation, with its intensity increasing with the Rossby number. Lagrangian tracers preferentially accumulate in cyclonic frontal regions, consistent with observations and other modeling studies. Second, we focus on the predictability of particle dynamics by comparing trajectories advected by the full flow and its geostrophic component, analogous to the velocity field derived from satellites. We find that geostrophic-only advection overestimates the pair-separation rate and introduces trajectory bias, with the effect increasing with the Rossby number. Moreover, clustering induced by ageostrophic motions can be significant, even for small flow compressibility, due to the interplay between compressibility and persistent flow structures. Third, we examine particle advection in the Kuroshio Extension, a region characterized by energetic fine scales, during February and August 2012, using LLC4320 velocity fields. In February, dispersion is local and driven by mesoscale and submesoscale motions. The geostrophic approximation effectively captures the kinetic energy spectra from sea surface height, with a slight overestimation of energy. In August, the situation is more complex, but our analysis suggests that dispersion becomes nonlocal while still being driven by mesoscale and submesoscale motions. Although internal gravity waves are energetically significant during summer, they do not appear to affect dispersion. Both the wave dispersion relation and geostrophic approximation are required for an accurate approximation of kinetic energy spectra from sea surface height. These findings provide insights into turbulent transport at ocean fine scales and are particularly relevant given the recent availability of new high-resolution satellite data on surface velocity fields.

Keywords: Lagrangian transport, turbulence, ocean submesoscales, numerical models

Unité de Mécanique de Lille - Joseph Boussinesq ULR 7512

Polytech' Lille, Bâtiment ESPRIT – Avenue Paul Langevin – 59650 Villeneuve-d'Ascq – France

DYNAMIQUE LAGRANGIENNE DANS LA TURBULENCE OCÉANIQUE À SOUS-MÉSOÉCHELLE**Résumé**

Les écoulements turbulents de surface dévient de l'équilibre géostrophique à des échelles inférieures à 10 km, essentielles pour le transport vertical, la distribution de la chaleur et le plancton. Bien que mesurer ces vitesses soit difficile, de nouvelles altimétries satellitaires haute résolution commencent à les capter. Toutefois, comme elles reflètent surtout l'écoulement géostrophique, comprendre l'impact des mouvements agéostrophiques non résolus est crucial pour bien caractériser le transport Lagrangien. Cette étude utilise des simulations numériques pour explorer la turbulence à petite échelle à l'aide d'un modèle tenant compte des corrections agéostrophiques, basé sur une expansion du nombre de Rossby des équations primitives, se réduisant au modèle quasi-géostrophique pour des nombres de Rossby nuls. De plus, nous analysons les trajectoires des particules lagrangiennes avec les champs de vitesse LLC4320, un modèle de circulation générale haute résolution capturant les processus océaniques de basse et haute fréquence. Premièrement, nous analysons l'impact des dynamiques agéostrophiques sur la dispersion par paires et le regroupement des particules pour différents nombres de Rossby. Les résultats montrent que, bien que la séparation des paires à long terme soit peu affectée, ces dynamiques provoquent une agrégation temporaire, dont l'intensité augmente avec le nombre de Rossby. Les particules s'accumulent préférentiellement dans les régions frontales cycloniques, en accord avec les observations et d'autres études. Deuxièmement, nous comparons les trajectoires advectées par l'écoulement complet et sa composante géostrophique, analogue au champ de vitesse dérivé des satellites. L'advection géostrophique surestime le taux de séparation des paires et introduit un biais dans les trajectoires, cet effet augmentant avec le nombre de Rossby. De plus, le regroupement induit par les dynamiques agéostrophiques peut être significatif, même avec une faible compressibilité, en raison de l'interaction avec des structures d'écoulement persistantes. Troisièmement, nous examinons l'advection des particules dans l'extension du Kuroshio en février et août 2012 avec les champs de vitesse LLC4320. En février, la dispersion est locale et dominée par les mouvements à mésoéchelle et sous-mésoéchelle, et l'approximation géostrophique capture bien les spectres d'énergie cinétique de la hauteur de la surface de la mer, avec une légère surestimation de l'énergie. En août, la situation est plus complexe, mais notre analyse suggère que la dispersion devient non-locale, tout en restant dominée par les mouvements à mésoéchelle et sous-mésoéchelle. Bien que les ondes de gravité internes soient importantes en été, elles n'affectent pas la dispersion. La relation de dispersion des ondes et l'approximation géostrophique sont nécessaires pour une approximation précise des spectres d'énergie cinétique à partir de la hauteur de la surface de la mer. Ces résultats fournissent de nouvelles perspectives sur le transport turbulent à petite échelle et sont pertinents avec l'arrivée de données satellitaires haute résolution sur les champs de vitesse de surface.

Mots clés : transport Lagrangien, turbulence, sous-mésoéchelles océaniques, modèles numériques

Acknowledgements

First and foremost, I would like to express my heartfelt gratitude to my family for their unwavering support throughout my academic journey. Their encouragement, patience, and belief in me have been the foundation upon which I've reached this milestone. I am deeply thankful for their continuous presence and guidance during this challenging and rewarding experience.

I would also like to sincerely thank my supervisor, Stefano Berti, for his invaluable guidance and meticulous attention to detail. His mentorship has shaped my growth as a researcher and played a crucial role in making me the academic I am today. His dedication and expertise have been instrumental throughout this journey.

In addition, I would like to thank my co-supervisor, Gilmar Mompean, for his administrative guidance and support. His assistance, especially with practical matters, has been invaluable throughout my research.

Finally, I thank Guillaume Lapeyre and Aurélien Ponte for their collaboration and valuable input throughout this project. I am also grateful to Enrico Calzavarini for always being willing to answer my questions whenever I showed up at his office door.

Table of Contents

Abstract	ix
Acknowledgements	xi
Table of Contents	xiii
List of Figures	xv
Introduction	1
I Ocean Scales and Modeling	5
1 Ocean Fine Scales: Mesoscales and Submesoscales	7
1.1 Ocean Scales	8
1.2 Ocean Submesoscales	10
2 Ocean Modeling	19
2.1 2D Turbulence	20
2.2 Quasi-Geostrophic (QG) Theory	24
2.3 Surface Quasi-Geostrophic (SQG) Theory	29
2.4 Next order in Rossby Submesoscale Model	32
2.5 Lagrangian Dispersion in Turbulent Flows	34
II Methodology	41
3 Numerical Method	43
3.1 Eulerian Implementation	43
3.2 Lagrangian Implementation	47

III Results	53
4 Particle dispersion and clustering in surface ocean turbulence with ageostrophic dynamics	55
4.1 Turbulent flow properties	56
4.2 Lagrangian dynamics	59
4.3 Conclusions	74
5 Impact of ageostrophic dynamics on the predictability of Lagrangian trajectories in surface-ocean turbulence	77
5.1 Eulerian properties	79
5.2 Lagrangian dispersion	85
5.3 Small-scale particle dynamics and clustering	92
5.4 Conclusions	100
6 Particle dispersion in a general circulation model	103
6.1 Model description	104
6.2 Internal Gravity Waves	107
6.3 Lagrangian Properties	110
6.4 Eulerian Properties	119
6.5 Conclusions	128
Conclusions	131
Bibliography	135
A Lyapunov exponents' spectrum	149
B Compressibility ratio	151
C Further Data and Figures	153

List of Figures

1	Picture of oil gathering above the Deepwater Horizon wellhead taken on May 6, 2010 by Daniel Beltrá and published in <i>The New Yorker</i>	2
2	Schematic of the SWOT data cycle, illustrating how satellite observations capture oceanic and inland water properties, which are then transformed into high-resolution data products. These products are essential for addressing critical societal challenges, such as water resource management and climate monitoring (source: NASA)	3
1.1	Multiple phytoplankton blooms off the coast of the Falkland Islands (South Atlantic Ocean) captured by one of the Copernicus Sentinel-3 satellites on 26 November 2022.	8
1.2	Stages in the oceanic general circulation from planetary-scale forcing to microscale dissipation and mixing (adapted from [3]).	10
1.3	Global simulation snapshot of ocean surface relative vorticity (s^{-1}) at ~ 2 km resolution. Panel (a) and (b) show the relative vorticity on the first day of March and September, respectively. Each panel includes a global map with two zoomed-in views: one on a region in the Northern Hemisphere and the other on a region in the Southern Hemisphere (adapted from [13]).	12
1.4	Landsat 8 false-color image of large cyanobacteria bloom in the Baltic Sea on 11 August 2015. Panel (b) is a zoomed-in view of the indicated box region in (a). The reference length bars for panels (a) and (b) are 10 km and 1 km, respectively (source: <i>Landsat Image Gallery</i> and [3]).	13
1.5	Comparison of the observations made by a combination of 7 radar altimeters [panel (a)] with the observations made by SWOT [panel (b)] over a stretch of the ocean in the Gulf Stream region off Cape Hatteras [16]. The reference length bars for panels (a) and (b) are 50 km.	14

1.6	Evolution of a drifter array in the northern Gulf of Mexico in February 2016 over 24 days. Panels A to F show the drifter positions at selected times. Inset E zooms in on a 60 m-wide cluster of 127 drifters (in magenta). Each panel is centered on the magenta drifters. Drifters in white eventually exit the frame. The grey tails (solid grey lines) show a 125-minute trail of the drifters' motion [18].	16
1.7	Sketches of surface-layer frontogenesis induced by a large-scale deformation flow: for a front [panel (a)] and a dense filament [panel (b)]. The along-axis flow $v(x, z)$ is partly geostrophic, and the secondary circulation (u, w) is ageostrophic (adapted from [3]).	17
1.8	Scale-dependent dispersion rates as a function of separation distance, shown for real and synthetic drifter launches. Solid points represent real drifter data, while empty points indicate synthetic drifter data from a 3-km resolution simulation corresponding to the real launches. The $r^{-2/3}$ scaling law is the dimensional expectation in the Richardson regime (adapted from [26]).	18
2.1	Sketch of the energy spectrum of a 2D turbulent flow in log-log scale. The green and blue arrows represent the inverse cascade of energy and the direct cascade of enstrophy, respectively. The red arrow represents the energy injection into the system.	23
2.2	Variance power spectra of wind and potential temperature near the tropopause from Global Atmospheric Sampling Program (GASP) aircraft data. The meridional wind and temperature spectra are shifted one and two decades to the right, respectively. [36]. . . .	24
3.1	Kinetic energy spectra, temporally averaged over several flow realizations in the statistically steady state for $Ro = 0.075$ at resolutions $N^2 = 256^2, 512^2, 1024^2$	46
3.2	Kinetic energy (a) and enstrophy (b) as a function of time for the different Rossby numbers.	47
3.3	Illustration of a grid for bicubic interpolation. Blue dots are the 4×4 grid used to interpolate a value within the smaller 2×2 grid in red dots.	48
3.4	(a) Lagrangian acceleration criterion and (b) its relative error ε_r , both averaged over all particles, for different Rossby numbers. In panel (a), for $Ro \leq 0.0375$, $\langle L \rangle$ is sufficiently small and overshadowed by the larger Rossby numbers.	49
3.5	Relative dispersion, in the x and y direction, as a function of time for $Ro = 0.075$	50

3.6	Relative dispersion as a function of time for $Ro = 0.075$ for different numbers of pairs.	51
4.1	Kinetic energy, E , as a function of Ro . Here, the kinetic energy spectra, $E(k)$, are temporally averaged over several flow realizations in the statistically steady state.	57
4.2	Kinetic energy spectra, temporally averaged over several flow realizations in the statistically steady state for $Ro = 0$ and $Ro = 0.075$. The dashed black line in the main panel corresponds to the expectation for SQG dynamics. Inset: the same spectra compensated by k^{-2} and rescaled with a coefficient such that, in both cases, the scaling range corresponds to the wavenumbers for which $E(k)k^2 \simeq 1$	58
4.3	Probability density function of vorticity ζ (rescaled by its rms value s_ζ), temporally averaged over several flow realizations in the statistically steady state, for $Ro = 0$ (empty black points) and $Ro = 0.075$ (filled red points), with different point types indicating $\zeta > 0$ and $\zeta < 0$. For reference, the standard Gaussian distribution is also shown (dashed gray curve). Inset: vorticity skewness S_ζ as a function of the Rossby number; the solid green line corresponds to $S_\zeta \sim Ro^{1.87}$	60
4.4	Vorticity normalized by its rms value for $Ro = 0$ (a) and $Ro = 0.075$ (c) at a fixed instant of time in statistically stationary conditions. Panels (b) and (d) show a closeup view of the region in the black rectangle in the main panels (a) and (c), respectively, including the particle distribution at that time.	61
4.5	Root-mean-square of vorticity (ζ_{rms}) as a function of the Rossby number, averaged over several flow realizations in statistically steady conditions. The error is computed as the difference between the average over the full dataset and over half the dataset.	62
4.6	FSLE (rescaled by the flow integral time scale) for different Rossby numbers. Inset: the same without rescaling the FSLE. The $\delta^{-1/2}$ scaling law is the dimensional prediction for a kinetic energy spectrum $E(k) \sim k^{-2}$. The scale amplification factor is $r = 1.2$, and it was verified that the results are robust with respect to the choice of this parameter value.	64

- 4.7 Kurtosis of particle relative displacements (main panel) and relative dispersion (inset) as a function of time for different Rossby numbers. The t^3 (Richardson dispersion) and t^4 scaling laws in the inset are the expectations for a kinetic energy spectrum $E(k) \sim k^{-5/3}$ and $E(k) \sim k^{-2}$, respectively. 64
- 4.8 Velocity divergence sampled by particles, averaged over time and over all particles, as a function of the Rossby number. Here the error bars correspond to the standard deviation of the temporal statistics. The black dashed line is proportional to $-Ro^\alpha$, with $\alpha \simeq 2.07$ from a best fit. 65
- 4.9 Probability density function of the Eulerian flow divergence $\nabla \cdot \mathbf{u}$, temporally averaged over several flow realizations in the statistically steady state, for different values of Ro 66
- 4.10 Probability density function of Voronoï cell areas, normalized by the averaged cell area, $P(A/\langle A \rangle_{x_i})$, at an instant of time in the statistically steady flow state, for different values of the Rossby number. The curve labeled by $(Ro = 0.075)_g$ has been obtained from particles advected by the geostrophic flow only. The solid gray line is the theoretical prediction for uniformly distributed particles $f_{2D}(A/\langle A \rangle_{x_i})$ (see text). 68
- 4.11 Correlation dimension D_2 as a function of Ro , obtained from data in several statistically steady flow realizations. Uncertainties are estimated from the standard deviations of best fits over the range of small distances r_p where $C(r_p) \sim r_p^{D_2}$. The empty blue point is for particles advected by the geostrophic flow component only at $Ro = 0.075$. The black dashed line corresponds to the second-order Taylor expansion $D_2 \simeq 2 + aRo + bRo^2$, with $a \simeq -2.9$ and $b \simeq -50.2$ from a fit. 69
- 4.12 Mean divergence $\overline{\Delta}^{\zeta\sigma}$ conditionally averaged over vorticity (ζ) and strain (σ), from Eulerian (a) and Lagrangian (b) statistics, at a fixed instant of time in the statistically steady state of the flow, for $Ro = 0.075$. For the Lagrangian estimate, the subscript x_i indicates that Δ , ζ and σ are computed at particle positions. In both (a) and (b) the dashed lines correspond to $\sigma = |\zeta|$ 71
- 4.13 Sketch of an ideal straight front. The red and green vectors represent the velocity $u(x)$ and $v(x)$ respectively. \hat{x} is unit vector in the x direction and \hat{y} is unit vector in the y direction. The velocity components in an ideal straight front are independent of y 73

- 5.1 Rossby number estimated by $Ro\zeta^{\text{rms}}$ as a function of Ro for the full SQG⁺¹ simulations. 79
- 5.2 (a) Vorticity field ζ_f for the SQG⁺¹ system for $Ro = 0.0625$ at a specific time t_* during the statistically stationary state. (b) Difference field $\Delta\zeta = \zeta_f - \zeta_g$, where ζ_g is the geostrophic component of vorticity. Panels (c) and (d) show the distribution of particles at time t_* in the region corresponding to the black rectangle in (a), for advection realized by either the full flow (c), or its geostrophic component (d). In (c) and (d), the full and geostrophic vorticity fields are shown in color, respectively. In all panels, vorticity is normalized by the rms value of ζ_f 81
- 5.3 Kinetic energy spectra, temporally averaged over several flow realizations in the statistically steady state for $Ro = 0$, $Ro = 0.0625$ and $(Ro = 0.0625)_g$ (i.e., for the geostrophic component of the simulation at $Ro = 0.0625$). The dashed black line corresponds to $k^{-5/3}$, the expected spectrum for SQG turbulence. Inset: absolute value of the relative difference of kinetic energy between the full and filtered flow as a function of Ro 82
- 5.4 Normalized correlation between the geostrophic and ageostrophic flow components as a function of Ro (where $u_g^{\text{rms}} = \sqrt{\langle |u_g|^2 \rangle}$ and similarly for u_{ag}^{rms}). Here, the average is over several flow realizations in statistically steady conditions, and errors bars are computed as the difference between the average over the full dataset and over half the dataset. 83
- 5.5 Skewness of vorticity ($S_\zeta = \langle \zeta^3 \rangle / \langle \zeta^2 \rangle^{3/2}$) as a function of the Rossby number for SQG⁺¹ (filled red points) and (SQG⁺¹)_g (empty blue points), averaged over several flow realizations in statistically steady conditions. The error is computed as the difference between the average over the full dataset and over half the dataset. Inset: Probability density function of vorticity ζ (rescaled by its rms value s_ζ), temporally averaged over several flow realizations in the statistically steady state for $Ro = 0.0625$. Here, the red and blue colors correspond to the SQG⁺¹ and (SQG⁺¹)_g cases, respectively. The dashed and solid lines are for $\zeta < 0$ and $\zeta > 0$, respectively. The shaded areas correspond to the standard deviation of the temporal statistics. For comparison, the long-dashed gray line represents a Gaussian distribution. 84

- 5.6 (a) Relative dispersion (after subtraction of the initial value) $\langle R^2(t) \rangle - R_0^2$ as a function of time. The t^3 (Richardson dispersion) scaling law is the expectation for a kinetic energy spectrum $E(k) \sim k^{-5/3}$, and the t^2 one is the short-time ballistic expectation. Inset: early growth of relative dispersion $\langle R^2(t) \rangle$ versus time in semilogarithmic scale. (b) Kurtosis of separation as a function of time on a semilogarithmic scale. The horizontal dashed line is the expectation $ku = 2$ in the diffusive regime. The inset shows the same in logarithmic scales. In both (a) and (b) $Ro = 0.0625$, the filled red points correspond to advection by the full SQG⁺¹ flow and the empty blue ones to advection by its geostrophic component only. 87
- 5.7 FSLE of the first kind $\lambda(\delta)$ for $Ro = 0.0625$; the filled red points correspond to advection by the full SQG⁺¹ flow and the empty blue ones to advection by its geostrophic component only (i.e., by the filtered flow). The δ^{-2} scaling law is the dimensional expectation in the diffusive regime. Inset: the relative difference between the plateau value (at small separations) of $\lambda(\delta)$ for particles advected by either the full flow or the filtered one, as a function of Ro 89
- 5.8 FSLE of the second kind $\tilde{\lambda}(\delta)$ for different Rossby numbers. The filled black points correspond to the FSLE-I $\lambda(\delta)$, averaged over the values obtained at the different Rossby numbers. The uncertainty is here quantified by the standard deviation computed using the latter values. Inset: FSLE-II rescaled by the Rossby number and the rms value of the ageostrophic velocity. 90
- 5.9 (a) Lyapunov exponents of the Lagrangian dynamics (red squares for λ_1 and black circles for λ_2) for varying Rossby number. (b) Mean Lagrangian strain, $s = \lambda_1 - \lambda_2$, and divergence, $d = \lambda_1 + \lambda_2$ versus Ro . In both (a) and (b) the filled and empty points are calculated from SQG⁺¹ flows and their filtered counterpart (SQG⁺¹)_g, respectively. Uncertainties, estimated as the standard deviation of $\lambda_{1,2}$ over their time series (at large times), are mostly of the order of point size. 94
- 5.10 Lyapunov dimension D_L , for particles advected by the full flow, as a function of compressibility \mathcal{C} ; the solid red line is the expectation $D_L = 2/(1 + 2\mathcal{C})$ in the compressible Kraichnan model. Inset: compressibility versus Ro and the prediction $\mathcal{C} \sim Ro^2$ (dashed line). Uncertainties on D_L and \mathcal{C} are estimated from the standard deviation using the values taken over their time series (at large times). 96

- 5.11 Fractal dimension D_F as a function of Rossby number; D_2 and D_L are the correlation dimension and Lyapunov dimension, respectively. The error bars for D_L are of the order of points size and are obtained from the standard deviation of the temporal statistics, while for D_2 , they are obtained from the standard deviation of best fits over the range of small distances r where $C(r) \sim r^{D_2}$. The filled and empty points are for SQG^{+1} and $(\text{SQG}^{+1})_g$, respectively. 98
- 6.1 Sketch of the initial configuration of a triplet. Black dots are the particles. The red dot is the center of mass of the triplet. 105
- 6.2 SWOT orbit during the fast-sampling phase (adapted from [110]). The red point indicates the location of the Kuroshio study zone . 106
- 6.3 Snapshot of the SST field from the LLC4320 simulation of the Kuroshio zone on February 1, 2012, and 30 days later, in panels (a) and (b), respectively. Each panel includes black points representing the particles selected for the Lagrangian analysis. The white box in panel (a) outlines the initial sampling domain, where these particles were initially seeded. The green box in panel (b) marks the studied domain, which encompasses all particles at the final time of the study. 107
- 6.4 Images of the Andaman Sea captured by the Operational Land Imager (OLI) on Landsat 8 on November 29, 2019. Panel (a) shows a comprehensive view of the sea and coast, while panel (b) shows a detailed view of the area within the white box shown in panel (a). The sunglint effect enhances the visibility of internal waves, with color enhancements helping to distinguish detailed water features. Lighter and darker tones indicate variations in water depth (darker is deeper) and suspended sediments from nearby rivers (from the [NASA Earth Observatory](#)). 109
- 6.5 Schematic of the frequency-wavenumber spectrum showing the different dynamical regimes in the ocean: the low-frequency mesoscale/submesoscales, the high-frequency submesoscales, and IGWs. The dispersion relations for the first 4 baroclinic modes (dashed lines) and the 10th mode (solid line) are plotted. f and M_2 are the Coriolis and semidiurnal tidal frequencies, respectively. M_2 is related to the direct gravitational effect of the Moon on the tides (adapted from [115]). 111

- 6.6 (a) Absolute dispersion $\langle A^2 \rangle$, for February and August, as a function of time. $\sigma_L^2 t^2$ is the expectation in the short-time ballistic regime, represented by the cyan and black short-dashed lines for February and August, respectively. The t scaling law (long-dashed line) is the expectation in the diffusive regime. Uncertainties, estimated as the 95% confidence interval, are mostly of the order of the point size. Inset: Lagrangian velocity autocorrelation function $C(\tau)$ versus time. The dashed black line corresponds to a decreasing exponential function. (b) Lagrangian frequency spectrum of the kinetic energy $E(\omega)$ for February and August. The ω^{-2} scaling law corresponds to an exponential decay of the Lagrangian velocity autocorrelation function [17]. 113
- 6.7 Absolute diffusivity K_{abs} , for February and August, as a function of time. $\sigma_L^2 t$ is the expectation in the short-time ballistic regime, represented by the cyan and black short-dashed lines for February and August, respectively. In the diffusive regime, K_{abs} converges to a constant value. Uncertainties, estimated as the 95% confidence interval, are mostly of the order of the point size. 114
- 6.8 Relative dispersion normalized by its initial value (after subtracting the initial value) $(\langle R^2 \rangle - R_0^2)/R_0^2$, for February and August, as a function of time. Zt^2 is the expectation in the short-time ballistic regime, represented by the cyan and black short-dashed lines for February and August, respectively. The t^3 scaling law is the Richardson expectation for a kinetic energy spectrum $E(k) \sim k^{-5/3}$. The t scaling law (long-dashed line) is the expectation in the diffusive regime. Uncertainties, estimated as the 95% confidence interval, are mostly of the order of the point size. . . 115
- 6.9 Relative diffusivity K_{rel} , for February and August, as a function of time. The $R^{3/2}$ and R^2 scaling laws (short-dashed and long-dashed lines) correspond to $\beta = 2$ and $\beta > 3$, respectively. In the diffusive regime, the relative diffusivity is constant such that $K_{rel} \sim 2K_{abs}$, represented by the cyan and black solid lines for February and August, respectively. Uncertainties are estimated as the 95% confidence interval. 116
- 6.10 Kurtosis of separation ku , for February and August, as a function of time. The horizontal short-dashed line is the expectation $ku = 5.6$ in the Richardson regime, while the horizontal long-dashed line is the expectation $ku = 2$ in the diffusive regime. Uncertainties are estimated as the 95% confidence interval. 117

- 6.11 FSLE $\lambda(\delta)$, for February and August, as a function of separation. The $\delta^{-1/2}$ scaling law (short-dashed line) corresponds $\beta = 2$. In the diffusive regime, the FSLE scales as δ^{-2} (long-dashed line). Uncertainties are estimated as the 95% confidence interval. . . . 118
- 6.12 Frequency-wave number spectra of kinetic energy $E(k, \omega)$ corresponding to the Kuroshio Extension during February (a) and August (b). The spectra are multiplied by k and ω , indicating the spectra are variance preserved [113]. The solid and dashed lines represent the Coriolis and tidal frequencies, respectively, while the dashed-dotted line represents the dispersion relation of mode-10. 120
- 6.13 Wavenumber spectra of kinetic energy, calculated from the $\omega - k$ kinetic energy spectrum, where $E(k) = \int E(k, \omega) d\omega$, for February (blue) and August (red). The scaling laws k^{-2} and $k^{-2.3}$ represent the fitted slopes for February and August, respectively. 121
- 6.14 Wavenumber spectra of kinetic energy $E(k)$ derived from surface velocities: total kinetic energy (KE in black), and filtered using the mode-10 dispersion relation to isolate mesoscale/submesoscale motions (in green) and IGWs (in blue), for February (a) and August (b). In (a), the scaling laws k^{-2} and $k^{-1.8}$ represent the fitted slopes for mesoscale/submesoscale motions and IGWs, respectively. In (b), the scaling laws k^{-3} and $k^{-2.3}$ represent the fitted slopes for mesoscale/submesoscale motions and IGWs, respectively. 122
- 6.15 Wavenumber spectra of kinetic energy $E(k)$ derived from surface velocities: total kinetic energy KE (in black), the solenoidal component of kinetic energy KE_{ζ} (filled points), and the divergent component KE_{Δ} (empty points), partitioned based on $\omega^2 < f^2(1 + L_R^2 k^2)$ and $\omega^2 > f^2(1 + L_R^2 k^2)$, represented by superscripts “-” and “+”, respectively. Panels (a) and (b) correspond to February, and panels (c) and (d) to August. In (a) and (b), the scaling law k^{-2} represents the fitted slope for KE_{ζ}^- . In (c) and (d), the scaling laws k^{-3} and $k^{-2.3}$ represent the fitted slopes for KE_{ζ}^- and KE_{Δ}^+ , respectively. . 124
- 6.16 Snapshot of the vorticity, normalized by the Coriolis parameter ζ/f , for the studied zone in the Kuroshio Extension, for February 15, 2012 (a) and August 15, 2012 (b). 125

- 6.17 Wavenumber spectra of kinetic energy $E(k)$ derived from surface velocities: total kinetic energy (KE in black), from sea surface height η (geostrophic kinetic energy; green), and the kinetic energy of IGWs (blue), for February (a) and August (b). In (a), the scaling laws $k^{-1.6}$ and $k^{-1.7}$ represent the fitted slopes for the geostrophic kinetic energy and the IGWs kinetic energy, respectively. In (b), the scaling laws k^{-3} and $k^{-2.3}$ represent the fitted slopes for the geostrophic kinetic energy and the IGWs kinetic energy, respectively. 126
- 6.18 Schematics of sea level shape and force balance for cyclonic (a) and anticyclonic (b) Gaussian eddies of the same size (adapted from [120]). The dashed line indicates the geostrophic case. F_{cor} (pink arrows), F_{centr} (blue arrows), and F_{press} (green arrows) represent the Coriolis, centrifugal, and pressure forces, respectively. 127
- 6.19 Probability density function of vorticity ζ (normalized by the Coriolis parameter f), temporally averaged over 30 days, for February (a) and August (b), with blue dots and red squares indicating $\zeta < 0$ and $\zeta > 0$, respectively. The shaded areas correspond to the standard deviation of the temporal statistics. 128
- B.1 Velocity-gradient correlations $\langle \partial_x u \partial_y v \rangle$ (filled points) and $\langle \partial_x v \partial_y u \rangle$ (empty points) as a function of time for the full SQG⁺¹ turbulent flow and different Rossby numbers (different point types). Inset: $\langle \partial_x u \partial_y v \rangle - \langle \partial_x v \partial_y u \rangle$, temporally averaged in the statistically steady state of the flow, as a function of the Rossby number. 152
- C.1 Eulerian mean divergence $\overline{\Delta}^{\zeta\sigma}$ conditionally averaged over vorticity (ζ) and strain (σ), averaged over several flow realizations in statistically steady conditions, for $Ro = 0.0125$ (a), $Ro = 0.0375$ (b), $Ro = 0.05$ (c) and $Ro = 0.075$ (d). 154
- C.2 Lagrangian Mean divergence $\overline{\Delta}_{x_i}^{\zeta\sigma}$ conditionally averaged over vorticity (ζ_{x_i}) and strain (σ_{x_i}) at particle positions x_i , averaged over several flow realizations in statistically steady conditions, for $Ro = 0.075$ 155

- C.3 Kinetic energy spectra temporally averaged over several flow realizations in the statistically steady state for SQG, SQG^{+1} and $(SQG^{+1})_g$ (i.e., for the geostrophic component of the SQG^{+1} simulation). Panels (a) to (f) show the spectra for Rossby numbers from 0.0125 to 0.075. The dashed black line corresponds to $k^{-5/3}$, the expected spectrum for SQG turbulence. Inset: the same spectra compensated by the best-fit power law $k^{-\beta}$ and rescaled with a coefficient such that the scaling range corresponds to the wavenumbers for which $E(k)k^\beta \simeq 1$ 156

Introduction

“How inappropriate to call this planet Earth when clearly it is Ocean” remarked Arthur C. Clarke, the renowned fiction and science writer, emphasizing the vastness of the ocean. In fact, the ocean covers around 71% of Earth’s surface. It plays a significant role on the Earth’s climate. Notably, it is responsible for storing and redistributing heat and carbon via ocean circulation. This occurs through various processes interacting across vastly different spatial and temporal scales. However, our knowledge of these processes is still incomplete. What complicates our understanding of this body of water is its inherent turbulent nature and the interactions between its different scales. Turbulence is a widely studied phenomenon that governs the behavior of most, if not all, fluids in nature. Richard Feynman described turbulence as "the most important unsolved problem of classical physics".

In this thesis, we particularly focus on the transport of Lagrangian particles in ocean submesoscale turbulence. Our study can be divided into two key areas of interest: Lagrangian transport and ocean submesoscales. The former is essential for our understanding of transport in the ocean, whether of physical properties such as temperature and salinity or material transport like nutrients, plankton, and pollutants. For example, after the Deepwater Horizon oil spill in 2010, oil spread across the Gulf Coast of the United States (as shown in Fig. 1), impacting the coastline from Louisiana to Florida. This endangered a vast amount of marine life and disrupted ecosystems. Consequently, efforts to extract and clean up the oil began, making it crucial to understand how the Gulf of Mexico currents transported it. Ocean submesoscale processes significantly influenced the oil’s movement and spread [1]. These submesoscale structures, occurring at horizontal scales between $O(1)$ and $O(10)$ km with a temporal



Figure 1: Picture of oil gathering above the Deepwater Horizon wellhead taken on May 6, 2010 by Daniel Beltrá and published in [The New Yorker](#).

variation of about 1 day, have been the focus of many oceanographic studies due to their significant role in ocean dynamics, mixing, and transport. Characterized to some extent by quasi-two-dimensional turbulent dynamics, they represent scales where conventional balances that apply at larger scales break down. This breakdown gives rise to important vertical velocities and other phenomena that influence Lagrangian transport properties.

This work is also motivated by the Surface Water Ocean Topography (SWOT) mission, a satellite launched at the end of 2022, which has started to provide sea surface height at unprecedented spatial resolution, capturing submesoscales (Fig. 2). However, as mentioned earlier, motions become unbalanced at the submesoscale level, rendering the geostrophic approximation, typically used

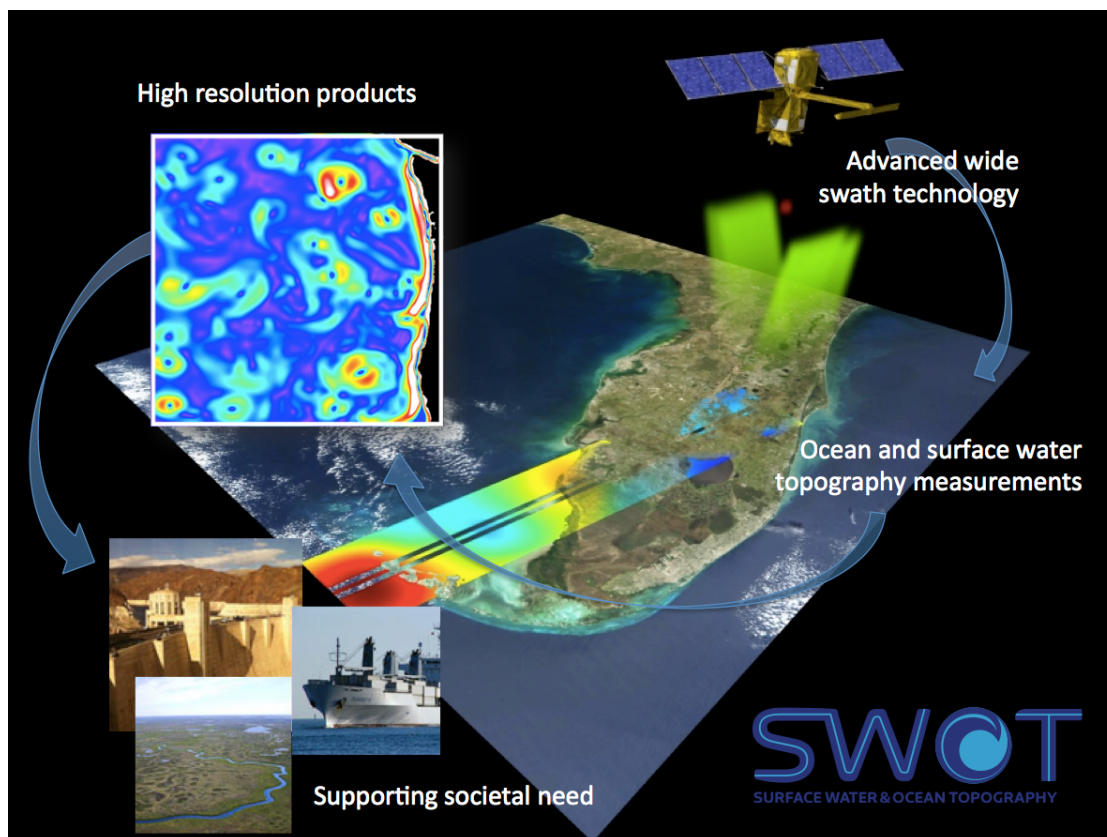


Figure 2: Schematic of the SWOT data cycle, illustrating how satellite observations capture oceanic and inland water properties, which are then transformed into high-resolution data products. These products are essential for addressing critical societal challenges, such as water resource management and climate monitoring (source: NASA)

to derive surface currents, inadequate or, at least, questionable. Therefore, evaluating the accuracy of SWOT signals is essential. The main question we seek to answer in this thesis is: how do ageostrophic (non-geostrophic) motions affect Lagrangian particle transport at the ocean submesoscale?

To that end, we use numerical simulations to investigate the spreading of Lagrangian tracer particles at the ocean surface in a model of upper-ocean turbulence. The adopted model can be seen as an extension of the quasi-geostrophic framework, conceived to account for some ageostrophic processes and, then, to capture the dynamics at submesoscales more accurately. To complete the picture, we also use data from a high-resolution general circulation model to examine the effect of other, faster ageostrophic processes that the previous model

cannot describe. Using the first model, we aim to reproduce Lagrangian convergence events observed from drifters and quantify their significance. We also characterize the dispersion of Lagrangian tracers by increasing the intensity of non-geostrophic motions to evaluate their effects. Subsequently, we re-examine these questions using the general circulation model to assess the potential impacts of faster processes, such as internal gravity waves and tides.

This thesis is divided into three parts. Part I introduces ocean phenomena, focusing on meso and submesoscale turbulence and their modeling. In Chapter 1, we describe oceanic scales, ranging from the smallest to the largest, before delving into the details of ocean submesoscales, where we discuss their characteristics and review relevant numerical and experimental observations. In Chapter 2, we introduce several prominent models used to study oceanic flows and their turbulent properties, namely 2D turbulence and quasi-geostrophic dynamics. We then explore the Surface Quasi-Geostrophic model, a special case of the Quasi-Geostrophic approximation, which is particularly effective in describing energetic submesoscale processes. Afterward, we introduce the model used in this study, which is based on the Surface Quasi-Geostrophic but extends it to account for non-geostrophic motions, known as the SQG⁺¹ model. Finally, we introduce the main properties of Lagrangian dispersion in turbulent flows since our main interest is Lagrangian transport in upper-ocean turbulence. Part II outlines the methodology. In Chapter 3, we describe the numerical implementation of the SQG⁺¹ model and the Lagrangian particle dynamics. Part III contains the core results of this study. In Chapter 4, we examine the effect of slow non-geostrophic motion intensity on the Eulerian flow properties and Lagrangian statistics. In Chapter 5, we more directly compare Lagrangian statistics for tracer particles advected by either the full, ageostrophic flow or its geostrophic component. Then, in Chapter 6, we use data from a general circulation model to study the effects of seasonal variability and internal waves on Lagrangian particle transport within the Kuroshio Extension, characterized by energetic submesoscales. Finally, a comprehensive conclusion summarizing the main findings is presented.

Part I

Ocean Scales and Modeling

Ocean Fine Scales: Mesoscales and Submesoscales

The ocean contains about 97% of the Earth's water. It is home to about 242000 marine species to date. It produces more than half of our planet's oxygen, sustaining terrestrial and marine life. Its circulation plays a vital role in shaping marine ecosystems. Additionally, through its interactions with the atmosphere, the ocean contributes to regulating the Earth's climate, impacting the response to climate change. The ocean's vast resources and ecosystems are critical for food security, providing livelihoods for millions of people, and supporting biodiversity, making its preservation and sustainable management essential for our planet's and future generations' health. To achieve this, we must first understand the mechanisms and dynamics that govern the ocean's circulation.

This chapter will briefly introduce the stages of oceanic circulation, covering scales from planetary to microscale (see Sec. 1.1). Specifically, in Sec. 1.2, we will focus on ocean submesoscales, presenting examples of campaigns and simulations aimed at measuring their characteristics, discussing the associated limitations, and highlighting the importance of newly emerging technology.

1.1 Ocean Scales

Flow structures of different horizontal scales are present in the ocean. One common way to identify them is through satellite images of phytoplankton blooms, as shown in Fig. 1.1. In this image, we see structures of various sizes: some are bigger than the Falkland Islands, and others are smaller. For reference, the distance from coast to coast for this island is around 200 km. These structures appear in the form of eddies and filaments. This image reveals the complexity of the ocean scales but does not account for all scales involved in the general ocean circulation.



Figure 1.1: Multiple phytoplankton blooms off the coast of the Falkland Islands (South Atlantic Ocean) captured by one of the Copernicus Sentinel-3 satellites on 26 November 2022.

Figure 1.2 shows a schematic of all the intervening scales in the oceanic general circulation. Starting with the largest scales, the planetary scale of horizontal size of $O(10^3)$ km evolves at a temporal scale of $O(1)$ year. This scale is characterized by gyres, which are large rotating currents. They are mainly driven by global wind patterns, continental boundaries, and buoyancy forcing [2]. The planetary scale is also subjected to climate forcing, related to the energy balance in the

Earth's atmosphere [3]. The Rossby Number is a well-known dimensionless number used to characterize geophysical flows. It is the ratio of inertial force to the Coriolis force, defined as:

$$Ro = \frac{U}{Lf} \quad (1.1)$$

where U and L are the characteristic velocity and length scales, respectively, and f is the Coriolis frequency. At the largest scales, Ro tends to zero; the Coriolis force plays a vital role on the dynamics of the flows. Events at those scales are relatively easy to detect using satellite altimetry. This is evident through the propagation of Rossby waves (also known as planetary waves) that was observed in the Southern Ocean using altimetry from TOPEX/POSEIDON and ERS-1 [4] (two satellites launched in the 1990's). In addition to being measurable, they are modeled quite well using the Boussinesq Navier-Stokes equations in a rotating reference frame, which will be discussed in more detail in Chapter 2.

On the other end of the scale spectrum are the smallest scales, known as the microscale (see Fig 1.2). These scales are clearly understood and modeled by the 3D Navier-Stokes equations. Here, the Rossby number is very large, and the system does not feel the Coriolis force. At these scales, the viscous forces of the fluid dissipate the energy input into the global system. Their horizontal scale is of $O(1)$ mm with a very fast temporal evolution of $O(1)$ second.

The planetary and microscale are relatively well understood compared to the intermediary scale, named mesoscale and submesoscale. The primary energy sink of the large planetary scales is the mesoscale balanced instabilities; balance refers to the hydrostatic and geostrophic balances, which are present in scales larger than approximately 100 km due to the ocean's high vertical stratification and the Earth rotation [5]. The hydrostatic balance is the balance between the gravitational acceleration and the vertical component of the pressure gradient force, and the geostrophic balance is the balance between the Coriolis force and the horizontal component of the pressure gradient force. We will discuss these balances further in Chapter 2. We mainly see mesoscale structures in Fig. 1.1. They span $O(10 - 100)$ km, evolve over a few weeks, and manifest as eddies and

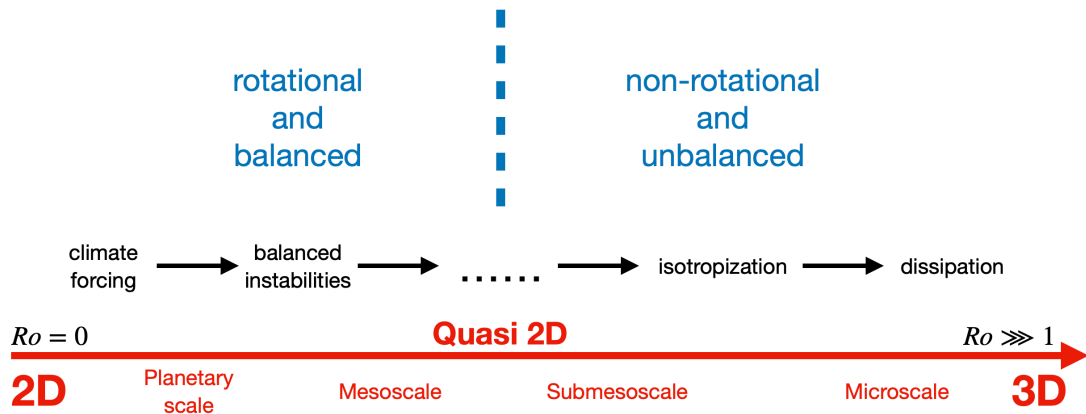


Figure 1.2: Stages in the oceanic general circulation from planetary-scale forcing to microscale dissipation and mixing (adapted from [3]).

fronts. Geostrophic eddies account for most of the total kinetic energy in the ocean [6–8]. These coherent mesoscale features have been carefully analyzed using sea-surface height (SSH) fields from satellite data by measuring their geographical distribution, lifespan, and size, among other characteristics [7]. An interesting conclusion of such studies is that these eddies can trap and advect water masses. These eddies and fronts not only confine water parcels but also stir their surroundings through horizontal advection. Consequently, they play a crucial role in mixing tracers, such as temperature, nutrients, and carbon. In addition, mesoscale processes impact the Earth’s response to climate change through the surface heat and momentum transfer between the ocean and atmosphere; this interaction influences both the ocean and the atmosphere [9]. Recent advancements in experimental and numerical technologies have significantly improved our understanding of oceanic mesoscale. However, the scales at the lower end of the mesoscale range remain less understood.

1.2 Ocean Submesoscales

Ocean submesoscales, named for their smaller size than larger mesoscale eddies, play an important role in ocean dynamics. These structures are characterized by a horizontal size of $O(1–10)$ km, and a vertical one of $O(10–100)$ m. They evolve

relatively rapidly, over time periods of $O(1)$ day [3, 10]. At these scales, Ro can reach values of $O(1)$. The inertial force becomes important, and the geostrophic balance breaks. They are characterized by intense vertical velocities reaching 100 m/day [10, 11]. These currents can be important in transporting nutrients from the deep ocean to the surface while transporting phytoplankton from the surface to deeper layers [12]. Additionally, they can transport heat with fluxes of $(20 - 100) \text{ W/m}^2$ in winter, which is more than 5 times larger than mesoscale vertical fluxes, contributing significantly to the global air-sea heat transfer [13]. Figure 1.3 shows a snapshot of the relative vorticity at the ocean surface, $\zeta = \partial_x v - \partial_y u$ where u and v are the velocity components of the horizontal flow, calculated from the LLC4320 simulation. The LLC4320 is a numerical simulation performed using the Massachusetts Institute of Technology general circulation model (MITgcm) on a Latitude-Longitude polar Cap (LLC) grid. It has a ~ 2 km resolution and can reasonably reproduce submesoscale dynamics. The model validation is achieved by comparing LLC4320 sea surface temperature (SST) with real SST observations [14]. Focusing on the zoomed-in views in Fig. 1.3, it becomes clear that seasonality influences the intensity of these small structures. As a quick reminder, when it is winter in the Northern Hemisphere, it is summer in the Southern Hemisphere, and vice versa. During winter, the flow is dominated by intense small eddies and filaments. Conversely, in summer, the flow is significantly smoother and characterized by larger eddies with smaller values of relative vorticity.

The flow structure observed in winter aligns with what is typically expected from submesoscale currents: strong vortices, elongated filaments, and, particularly, fronts [3]. A front is the boundary between two water masses with sharp differences in their properties, such as temperature, salinity, or nutrient content. For example, fronts can be observed in satellite SST images where cold and relatively hotter water meet. These structures are abundant in the submesoscale range and are also observed in chlorophyll concentration satellite data, as in Fig. 1.4. The visible patterns in the phytoplankton concentration field are formed by surface convergence lines, typical of submesoscales. These convergence zones significantly influence the concentration and distribution of biological material. Continuous observation is needed to track the development

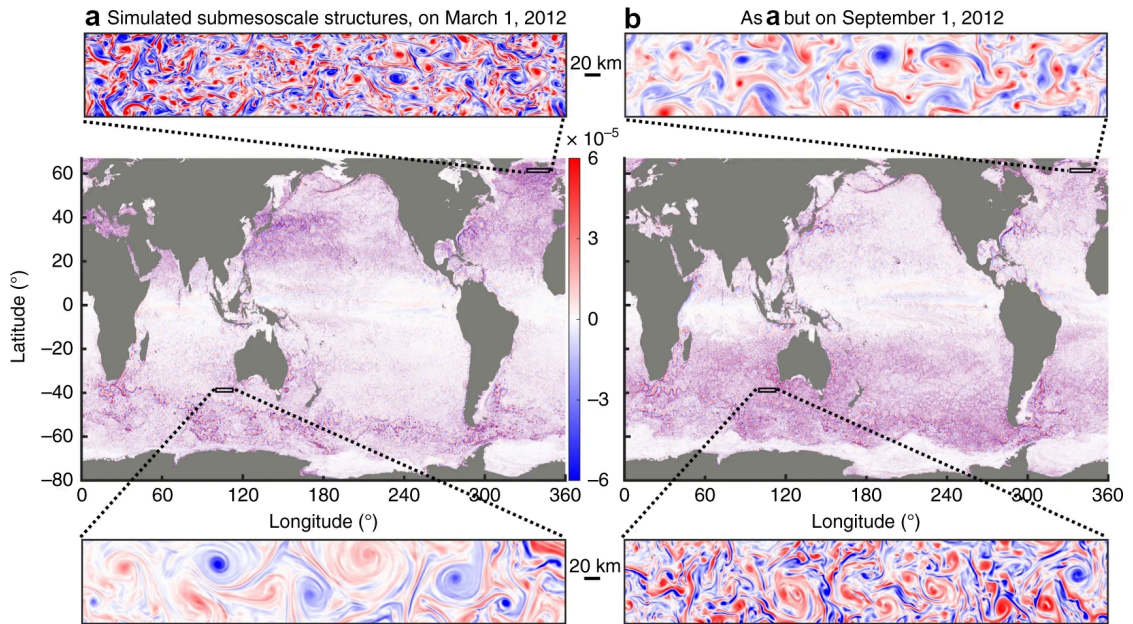


Figure 1.3: Global simulation snapshot of ocean surface relative vorticity (s^{-1}) at ~ 2 km resolution. Panel (a) and (b) show the relative vorticity on the first day of March and September, respectively. Each panel includes a global map with two zoomed-in views: one on a region in the Northern Hemisphere and the other on a region in the Southern Hemisphere (adapted from [13]).

of such events properly.

However, because of their small size and fast temporal evolution, submesoscales are notoriously challenging to measure. Conventional altimeter observations capture SSH for scales larger than 100 km. As mentioned previously (Sec. 1.1), these scales are in geostrophic balance; therefore, their velocity fields can be derived from SSH fields measured by satellites [5]. A key difference between mesoscale and submesoscale dynamics is the breakdown of the geostrophic balance in submesoscales. This presents two problems: first, conventional instruments cannot spatially resolve submesoscales, and second, there is no theoretical way to derive their velocity fields from SSH since they are not in geostrophic balance. Another general problem of remote sensing is cloud

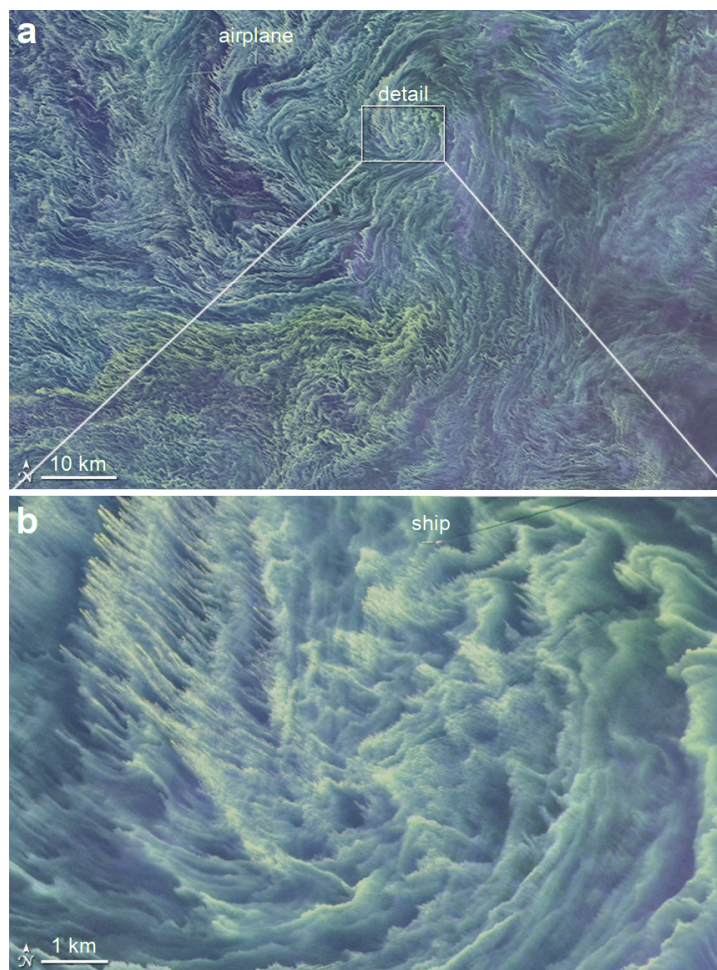


Figure 1.4: Landsat 8 false-color image of large cyanobacteria bloom in the Baltic Sea on 11 August 2015. Panel (b) is a zoomed-in view of the indicated box region in (a). The reference length bars for panels (a) and (b) are 10 km and 1 km, respectively (source: [Landsat Image Gallery](#) and [3]).

coverage [15]. Clouds hinder the satellite’s ability to capture high-resolution SST and chlorophyll measurements, as they rely on infrared electromagnetic radiation, which cannot penetrate clouds, leading to gaps in data and potential challenges in observing the fast-evolving submesoscale processes. In contrast, SSH, obtained via radar altimetry, is not impacted by cloud cover since radar signals can penetrate through clouds.

To address the shortcomings of conventional altimetry, the Surface Water and Ocean Topography (SWOT) satellite was launched on December 15, 2022. This

satellite is a collaborative mission between the National Aeronautics and Space Administration (NASA) and the National Center for Space Studies (CNES), with contributions from the Canadian Space Agency (CSA) and the UK Space Agency. SWOT is the first-ever instrument capable of globally monitoring volumetric changes in inland waters, providing data on freshwater. Additionally, it can measure SSH at an unprecedented resolution, resolving scales of about 1 km, which is a two-order-of-magnitude improvement. Its advanced sensors make this unique capability possible: a Ka-band radar interferometer (KaRIn) accompanied by two synthetic-aperture radar SAR antennas [16]. The SAR antennas provide 2D measurements across two wide swaths, supplementing the traditional 1D nadir measurement — a significant enhancement over traditional altimeters that offer only 1D data along the nadir track.

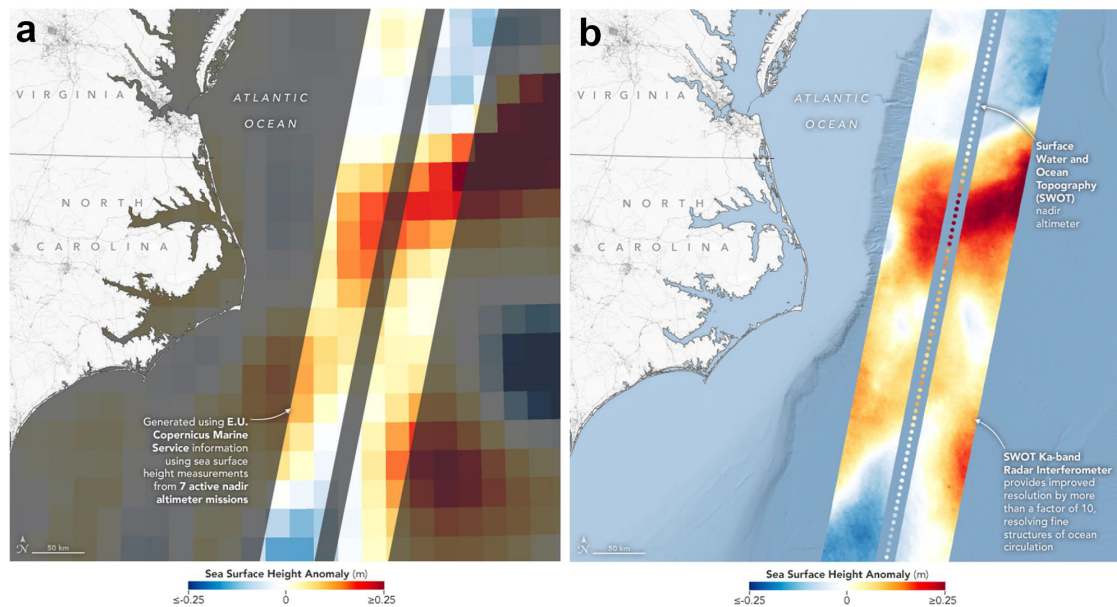


Figure 1.5: Comparison of the observations made by a combination of 7 radar altimeters [panel (a)] with the observations made by SWOT [panel (b)] over a stretch of the ocean in the Gulf Stream region off Cape Hatteras [16]. The reference length bars for panels (a) and (b) are 50 km.

This remarkable improvement is clearly seen in Fig. 1.5 where sea surface height anomaly (SSHA) measurements made by conventional altimetry are compared to those made by SWOT. In panel (a), the resulting SSHA field is quite pixelated and discrete; the combination of data from 7 altimeter mission barely resolves scales of 100 km, which is inadequate for detailed meso and submesoscale

observations. The details of the flows are hard to discern, with only the sharp differences in height being noticeable. In contrast, the SWOT measurements in panel (b) provide a much finer field image where the details of the flow are clear at scales smaller than 50 km. Based on what is observed in Fig. 1.5 and on along-track wavenumber spectra of SSH from SWOT data [16], it is evident that SWOT is capable of resolving submesoscales, revealing details of their characteristic eddies and fronts. However, these small scales evolve rapidly over time, making continuous data collection challenging since SWOT has a 21-day repeat period. It is worth noting that during its first six months, SWOT operated on a 1-day orbit to calibrate and validate its measurements. As mentioned previously, the geostrophic balance breaks down at fine enough scales, and determining the full flow field from SSH becomes challenging.

So far, we have only examined remote sensing Eulerian measurements at the ocean surface. However, due to the abovementioned difficulties, these measurements cannot fully resolve submesoscales or capture the complete flow. Complementary measurements, such as those from Lagrangian drifters and in-situ moorings, provide additional high-temporal-resolution data, aiding in the reconstruction of the full flow. Drifters are instruments that float freely on the ocean surface to investigate currents via location tracking. They can also be equipped with sensors to measure various quantities such as temperature, pressure, and salinity. These drifters provide wide spatial coverage and fast sampling, which serve as a basis for Lagrangian transport studies in the ocean [17]. Unlike drifters, moorings are fixed to maintain position by attachment to the sea floor or through other stabilizing methods; as they sample the flow (at different depths) at a fixed position in space, they fall under the Eulerian measurement category.

In this work, our primary focus is on Lagrangian transport at the ocean surface, making drifters particularly relevant to our study. While studying the trajectories of drifters deployed in the Gulf of Mexico, a remarkable phenomenon was observed: drifters spreading over 20 km (Fig. 1.6A) align following a filamental structure (Fig. 1.6C), and spiral in anti-clockwise direction until they gather into a 60 m wide cluster (Fig. 1.6D). This event takes about 10 days to unfold [18]. Such clustering events have also been observed in ocean general

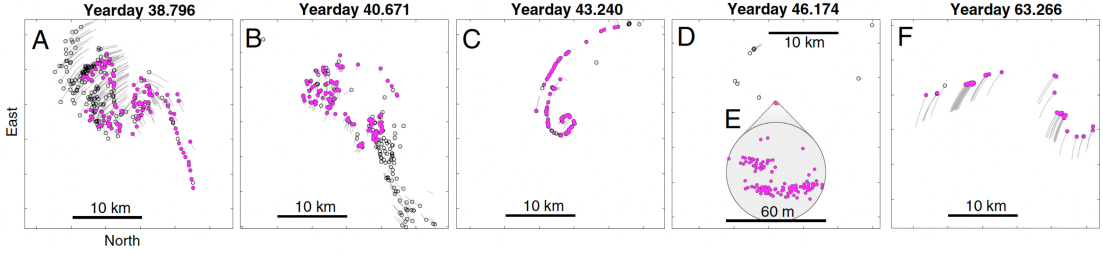


Figure 1.6: Evolution of a drifter array in the northern Gulf of Mexico in February 2016 over 24 days. Panels A to F show the drifter positions at selected times. Inset E zooms in on a 60 m-wide cluster of 127 drifters (in magenta). Each panel is centered on the magenta drifters. Drifters in white eventually exit the frame. The grey tails (solid grey lines) show a 125-minute trail of the drifters' motion [18].

circulation and primitive-equations-based simulations of submesoscales [19–21]. This means that while, globally, Lagrangian particles spread over time, every now and then, many of them are brought together in regions of very limited size. Such convergence events are associated with large vorticity (and divergence) values highlighting the departure from geostrophic balance - meaning that the Rossby number, roughly estimated by $Ro = \zeta/f$ (with ζ relative vorticity and f Coriolis frequency), is not negligibly small - and with the onset of important vertical velocities. Positive (cyclonic) vorticity is stronger in the surface layer due to finite Ro -effects of vortex stretching in the vorticity evolution equation $\partial_t \zeta \approx (f + \zeta) \partial_z w + \dots$ (with w the vertical velocity component), ageostrophic instabilities and loss of balance that limits anticyclonic vorticity amplitudes to $\zeta/f \gtrsim -1$ [3]. This leads to an asymmetry of vorticity statistics, with cyclones prevailing over anticyclones. This cyclone-anticyclone asymmetry, with a cyclonic dominance, has been observed in both in-situ measurements and numerical simulations of submesoscales [22–24]. The intensification of positive vorticity can be understood, to some extent, through frontogenesis, the dynamical process that generates sharp density gradients (including horizontal gradients of surface buoyancy) through the large-scale deformation field, thus forming and strengthening fronts [25]. Figure 1.7 shows sketches of strain-induced frontogenesis produced by a large-scale deformation flow for a buoyancy front and a dense filament. For a front (Fig. 1.7a), the flow features a circulation cell with upwelling and surface divergence on the lighter side and downwelling and

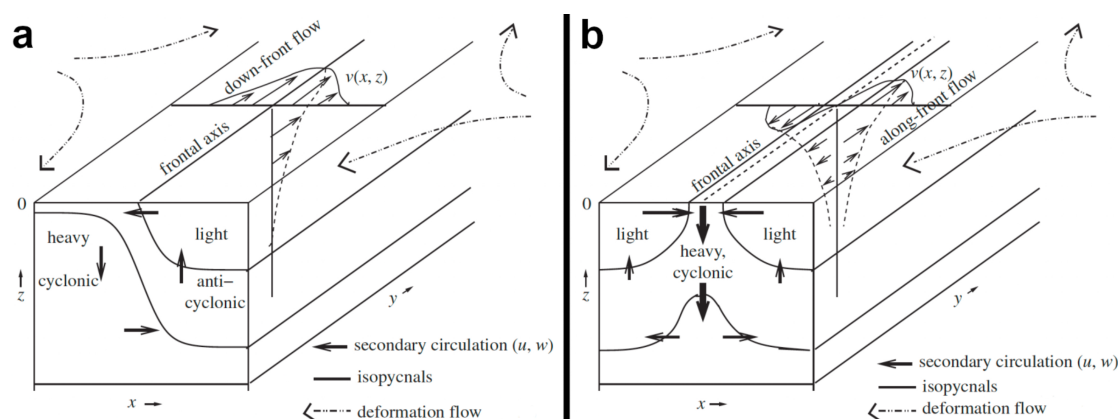


Figure 1.7: Sketches of surface-layer frontogenesis induced by a large-scale deformation flow: for a front [panel (a)] and a dense filament [panel (b)]. The along-axis flow $v(x, z)$ is partly geostrophic, and the secondary circulation (u, w) is ageostrophic (adapted from [3]).

surface convergence on the denser side. In the weakly stratified upper layer, where $\partial_z w < 0$ is most pronounced in z , vortex stretching generates anticyclonic vorticity on the light side of the front and cyclonic vorticity on the dense side. Due to the finite Ro of submesoscales, the combined effects of $\zeta \partial_z w$ (absent for vanishingly small Ro) and $f \partial_z w$ result in a greater amplification of cyclonic vorticity compared to anticyclonic vorticity. In the case of a dense filament (Fig. 1.7b), two counter-rotating secondary circulation cells generate intense downwelling and surface convergence along the frontal axis, which generates cyclonic vorticity and positively skews the vorticity statistics, similar to a front. Additionally, this figure highlights the role of frontogenesis in generating large vertical velocities and mixing the ocean's upper layer.

As a result of downwelling and surface convergence, Lagrangian tracers can be expected to cluster temporarily; however, similar to typical turbulent flows, they generally separate and disperse over long enough times [17, 26, 27]. At the submesoscale level, the flow can be highly energetic (especially in winter) [25]. Comparisons between actual drifter data and synthetic drifters from a simulation with a resolution of 3 km clearly demonstrate that at scales smaller than 10 km, synthetic drifters underestimate the rate of dispersion, as shown in Fig. 1.8. The real drifter data suggest that the dispersion process is primarily influenced by the energetic scales that match the separation distance of the drifters at these

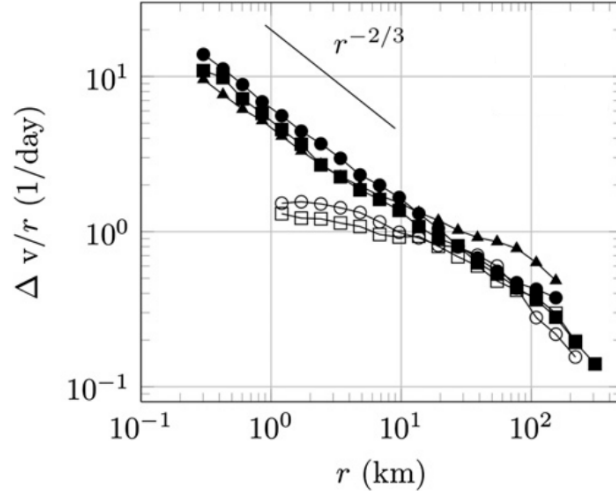


Figure 1.8: Scale-dependent dispersion rates as a function of separation distance, shown for real and synthetic drifter launches. Solid points represent real drifter data, while empty points indicate synthetic drifter data from a 3-km resolution simulation corresponding to the real launches. The $r^{-2/3}$ scaling law is the dimensional expectation in the Richardson regime (adapted from [26]).

scales [26]. This is missed by large-scale ocean numerical simulations, due to the high dissipation at the grid size the energy is drastically dumped leading to an underestimation of the energy content at submesoscales.

In conclusion, submesoscales are challenging to measure due to their small size and rapid evolution. Recent advancements in remote sensing technology allow us to achieve better-resolved Eulerian measurements of submesoscales. However, since the derived velocity fields are essentially geostrophic, an assessment is needed to determine how closely they represent the full velocity fields. A cyclone-anticyclone asymmetry with cyclonic dominance and a nonzero horizontal divergence characterizes these submesoscales. These flow features are crucial for vertical mixing, material transport, and heat transfer. This thesis aims to better understand the effect of submesoscale dynamics on horizontal Lagrangian transport properties through a minimal model based on the physical modeling of the flow.

Ocean Modeling

Ocean circulation is a combination of various flow types, with motions ranging from millimeters to kilometers in size and evolving over temporal scales from seconds to years (see Fig. 1.2). To study the dynamics from the basin to submesoscales, researchers use a combination of observations, theories, and high-resolution numerical models. A major challenge is understanding how energy is transferred from scales of thousands of kilometers, driven by large-scale atmospheric winds and heat fluxes, down to millimeter scales, where energy dissipates as heat. The first important energy transfer is from large-scale ocean currents to mesoscale eddies. Large-scale ocean currents are unstable due to baroclinic instability, generating eddies with scales $O(100)$ kilometers. These mesoscale eddies then interact, producing submesoscale turbulent filaments ranging from 10 kilometers to 1 kilometer. Planetary scales are primarily horizontal, constrained by ocean stratification and rotation, and resemble two-dimensional turbulent flows. Only around the lower mesoscale and submesoscale range does the turbulence become quasi-two-dimensional and eventually three-dimensional at microscales. Physically, as for any fluid, ocean dynamics are governed by the 3D Navier-Stokes equations. However, simulating them using the latter by means of Direct Numerical Simulation (DNS) is not feasible because of the magnitude of the Reynolds Number in the ocean, $Re = UL/\nu$ where U , L , ν are the characteristic velocity and length of the flow and the fluid kinematic viscosity, respectively. For example, if we consider ocean submesoscales where

$U \approx 0.05$ m/s [28], $L \approx 10$ km and $\nu \approx 10^{-6}$ m²/s, we retrieve $Re \approx 5 \times 10^8$. To resolve all the scales and given that the Kolmogorov scale is the scale at which $Re = 1$ [29], we would need $O(10^{19})$ grid points, given that $N_{min} \sim Re^{9/4}$, where N_{min} represents the minimum number of grid points required [30]. To that end, simpler models that require less computational power were conceptualized to help enhance our understanding of geophysical flows.

This chapter is organized as follows. In Sec. 2.1, we introduce two-dimensional (2D) turbulence and its application to modeling the ocean mesoscale range. We then discuss the Quasi-Geostrophic (QG) theory in Sec. 2.2, which is able to reproduce large mesoscale dynamics and can be seen as an extension of 2D Navier-Stokes turbulence to rotating stratified fluids. Next, we cover Surface Quasi-Geostrophic (SQG) theory in Sec. 2.3, a special case of QG that is often considered more appropriate for energetic submesoscales. However, SQG cannot fully reproduce all submesoscale features. To address these limitations, we go beyond QG theory and introduce the SQG⁺¹ model in Sec. 2.4. To understand Lagrangian particle behavior in such flows, we present theoretical expectations for tracer particle motion in turbulent flows in Sec. 2.5 covering both single particle (Sec. 2.5.1) and two-particle (Sec. 2.5.2) statistics.

2.1 2D Turbulence

Turbulence is everywhere in nature, from the blood flow in arteries to the formation of galaxies. It is typically three-dimensional, and 2D turbulence is never fully reproduced in nature or the laboratory. Nevertheless, some physical systems exhibit many features of 2D turbulence. For instance, large motions in the atmosphere and the ocean (planetary scale in Fig. 1.2) may be approximated as 2D turbulent flows since the large aspect ratio (the ratio of lateral to vertical length scales) of these systems allows for a first approximation of this type. Prominent features of 2D turbulence are present in the theory of geostrophic turbulence [31]. Moreover, vorticity filaments, characteristic of 2D turbulence, appear in different systems, such as numerical simulations of 2D Navier-Stokes equations, flowing soap film experiments, and global circulation simulations [32]. From a theoretical perspective, 2D turbulence is not merely a

reduced dimensional version of 3D turbulence because new conservation laws in two dimensions lead to a completely different phenomenology.

For a 2D incompressible flow, the motion is described by the Navier-Stokes equations, which are based on the conservation of momentum [Eq. (2.1)] and the conservation of mass [Eq. (2.2)] equations which can be written as

$$\frac{\partial \mathbf{u}}{\partial t} + \mathbf{u} \cdot \nabla_H \mathbf{u} = -\frac{1}{\rho} \nabla_H p + \nu \nabla_H^2 \mathbf{u}, \quad (2.1)$$

$$\nabla_H \cdot \mathbf{u} = 0, \quad (2.2)$$

where $\mathbf{u} = (u, v)$ is the velocity field, $\nabla_H = (\partial_x, \partial_y)$ is the gradient, p is the pressure in the fluid and ρ is the fluid density. What is interesting in the case of 2D flows is the fact that vorticity, defined as the curl of the velocity $\zeta = \nabla_H \times \mathbf{u}$, is a scalar quantity. By taking the curl of Eq. (2.1) and considering only the z -component, we retrieve the vorticity equation:

$$\frac{\partial \zeta}{\partial t} + \mathbf{u} \cdot \nabla_H \zeta = \nu \nabla_H^2 \zeta. \quad (2.3)$$

Since the flow is incompressible, the velocity and vorticity can be derived from a streamfunction, ψ , such that $\mathbf{u} = (-\partial_y \psi, \partial_x \psi)$ and $\zeta = \nabla_H^2 \psi$. A main feature of 2D turbulence is the absence of vortex stretching, as evident from Eq. (2.3).

In classical 3D turbulence, vortex stretching plays an important role in breaking up large structures, eventually leading to a direct cascade of energy toward small scales. This cascade was famously theorized in 1941 by considering homogeneous, isotropic 3D flows of an incompressible fluid [29]. To understand the energy cascade, it is helpful to analyze the energy spectrum $E(k)$, which is directly related to the mean flow kinetic energy, E :

$$E = \frac{1}{2} \langle \mathbf{u}^2 \rangle = \int_0^\infty E(k) dk, \quad (2.4)$$

where $\langle \cdot \rangle$ is the spatial average, $E(k)$ is the kinetic energy spectrum and k is the wavenumber. Energy can be injected at any scale, but here, we focus on large-scale energy injection (small wavenumbers), as external forcing often occurs at

these scales in many geophysical contexts. Note that from here on, whenever we refer to forcing, we mean localized forcing around a forcing wavenumber k_f . The energy is then transferred through intermediate scales without significant loss, eventually reaching small scales (large wavenumber), where it is dissipated as heat. This represents the process at microscales in Fig. 1.2. In the inertial range at intermediate scales, the energy flux is constant. As a result, through dimensional arguments, the energy spectrum scales as $E(k) \sim k^{-5/3}$, a behavior known as the direct energy cascade [29]. In this range, kinetic energy is an inviscid invariant (i.e., $\nu \rightarrow 0$).

In 2D turbulence, vortex stretching is absent, and energy is contained in eddies whose sizes continuously increase as the flow evolves [33]. Instead of flow structures stretching and breaking down, eddies merge to form larger eddies. Here, energy is not dissipated at small scales. Instead, an inverse cascade is observed, where energy is transferred from the forcing scale, k_f , to larger scales, k_l , defined as $k_l = \int_0^\infty E(k)dk / \int_0^\infty k^{-1}E(k)dk$. In the energy inertial range ($k_l \ll k \ll k_f$), $E(k) \sim k^{-5/3}$ [34, 35]. Another important feature is that the mean-squared vorticity, represented by enstrophy Z (Eq. (2.5)), in addition to the kinetic energy, becomes an inviscid invariant. The latter is directly related to the enstrophy spectrum, $Z(k)$, and the energy spectrum:

$$Z = \frac{1}{2}\langle \zeta^2 \rangle = \int_0^\infty Z(k) dk = \int_0^\infty k^2 E(k) dk. \quad (2.5)$$

Enstrophy is transferred from the forced scale k_f to the smaller dissipative scale k_η , which corresponds to the viscous scale $l_\nu = (\nu^3/\eta)^{1/6}$, where ν is the viscosity and η is the enstrophy cascade rate in a homogeneous, isotropic 2D turbulent flow. At these smaller scales, enstrophy is dissipated by viscous forces. In the enstrophy inertial range ($k_f \ll k \ll k_\eta$), $E(k) \sim k^{-3}$ [34, 35]. Thus, in 2D turbulence, two cascades exist: the inverse energy cascade and the direct enstrophy cascade. A typical energy spectrum as a function of wavenumber is sketched in Fig. 2.1.

Interestingly, the direct enstrophy cascade was observed by aircraft data near the tropopause [36]. As shown in Figure 2.2, there is evidence of k^{-3} scaling at large scales (> 500 km). Additionally, there is clear evidence of a $k^{-5/3}$ slope

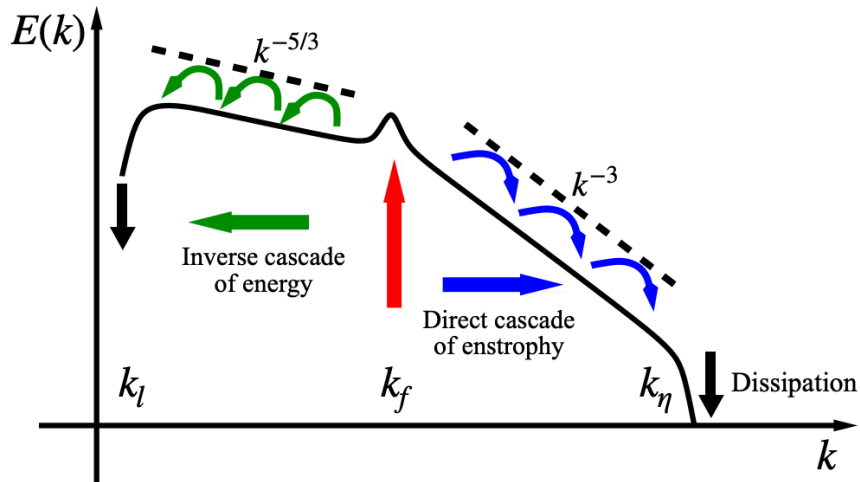


Figure 2.1: Sketch of the energy spectrum of a 2D turbulent flow in log-log scale. The green and blue arrows represent the inverse cascade of energy and the direct cascade of enstrophy, respectively. The red arrow represents the energy injection into the system.

between 3 – 300 km that is argued to be an energy cascade. This $k^{-5/3}$ spectral slope, at scales smaller than approximately 150 km, was also observed in kinetic energy spectra obtained from wind velocity data gathered from commercial flights between Chicago, Los Angeles and Honolulu [37].

After an extensive study, which included data from 5754 airplane flights as part of the Measurement of OZone by Airbus In-service airCRAFT (MOZAIC) program, where structure functions for 2D turbulence were derived and compared to the *in-situ* data, it was confirmed that the k^{-3} scaling can be explained by 2D turbulence and interpreted as a direct cascade of enstrophy. However, the $k^{-5/3}$ scaling cannot be explained by 2D turbulence alone, and we should not jump to conclusions too quickly by considering it an energy cascade [38]. At the mesoscale range [O(100) km], the flow dynamics are influenced by Earth's rotation and vertical density stratification, making 2D turbulence expectations insufficient to explain certain phenomena observed in empirical data. Therefore, quasi-2D turbulence models become necessary to understand mesoscale ocean dynamics better.

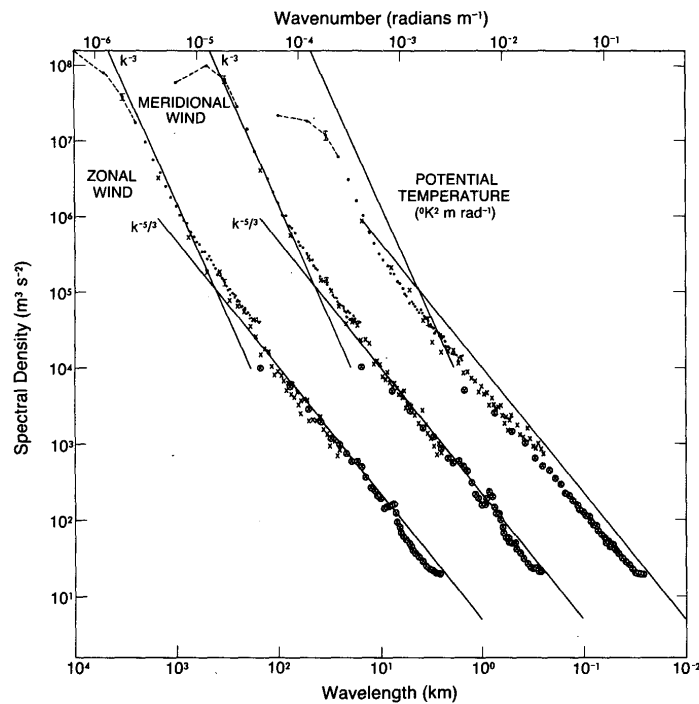


Figure 2.2: Variance power spectra of wind and potential temperature near the tropopause from Global Atmospheric Sampling Program (GASP) aircraft data. The meridional wind and temperature spectra are shifted one and two decades to the right, respectively. [36].

2.2 Quasi-Geostrophic (QG) Theory

QG theory is a simplified theoretical framework in geophysical fluid dynamics that describes the large-scale flow of the atmosphere and oceans, namely the large mesoscale [$O(100)$ km] regime. It is an approximation to the Navier-Stokes equations governing fluid motion. It provides extra levels of complexity that cannot be explored using 2D turbulence. Jule Charney developed the QG model based on the work of Carl-Gustaf Rossby [39]. Its primary use at that time was to forecast the weather.

The QG equations are derived from the primitive equations, which are based on the Boussinesq approximation, along with the hydrostatic and traditional approximations. The latter, less commonly known, neglects Coriolis terms in the horizontal momentum equations involving vertical velocity and smaller metric terms. In QG theory, the following assumptions are considered. First,

the deformation radius L_d , which is the length scale at which rotational effects become as important as buoyancy, should be of the same order as the horizontal characteristic length scale of the flow, such that $L/L_d \approx 1$. Consequently, the Rossby number is small, and the flow is near-geostrophic balance, i.e., $Ro \ll 1$. Second, variations in the Coriolis parameter f are small. Finally, the time scale of the flow is determined by the horizontal characteristic length and velocity. In this work, we prefer to show similarities between 2D turbulence and QG theory. Therefore, we will focus on deriving the potential vorticity q equation, which is analogous to the relative vorticity ζ equation in 2D turbulence in the absence of dissipation [Eq. (2.3) with $\nu = 0$]. A detailed derivation of the QG equation from the primitive equations can be found in [5].

Let us start by writing the horizontal momentum, the hydrostatic equation, the continuity, and the thermodynamic energy equation; these equations are known as the Boussinesq equation:

$$\frac{D\mathbf{u}}{Dt} + f\mathbf{k} \times \mathbf{u} = -\nabla_H \phi, \quad (2.6)$$

$$\frac{\partial \phi}{\partial z} = b, \quad (2.7)$$

$$\nabla_H \cdot \mathbf{u} + \frac{\partial w}{\partial z} = 0, \quad (2.8)$$

$$\frac{Db}{Dt} + N^2 w = 0, \quad (2.9)$$

where ϕ is a geopotential. $b = -g\delta\rho/\rho_0 = g\theta/\theta_0$ is the buoyancy with $\delta\rho$ and θ are small density and temperature fluctuations, respectively, and ρ_0 and θ_0 are reference density and temperature, respectively. w is the vertical velocity. $N^2 = \partial_z \bar{b}$ is the buoyancy frequency (i.e., Brunt–Väisälä frequency) with \bar{b} a mean vertical buoyancy profile. $D/Dt = \partial_t + \mathbf{u} \cdot \nabla + w \partial_z$ is the material derivative. To ease the derivation, a constant Coriolis parameter is assumed [$f = \text{constant}$]; this is known as the f -plane approximation. Other Coriolis parameter approximations can be used, such as the β -plane approximation, which considers meridional variations in f . The latter is used in [5] and leads to the same potential vorticity

(PV) equation.

As a result of the QG assumptions, the horizontal flow is nearly geostrophic. Since the horizontal flow is not in absolute geostrophic balance, we decompose the horizontal velocity into a geostrophic part (at lowest order in Ro) and ageostrophic parts, such that

$$\mathbf{u} = \mathbf{u}_g + Ro \mathbf{u}_{ag}^{(1)} + Ro^2 \mathbf{u}_{ag}^{(2)} + \dots, \quad (2.10)$$

where \mathbf{u}_g is the geostrophic part and $\mathbf{u}_{ag}^{(n)}$ is the ageostrophic part of $O(Ro^n)$. Similarly, the variables in Eqs. (2.6) to (2.9) can be expanded as a function of the Rossby number. The condition $Ro \ll 1$ allows us to retain only lowest order terms; therefore, to simplify the notation, we drop the superscript (n) for the ageostrophic part and the velocity becomes $\mathbf{u} = \mathbf{u}_g + Ro \mathbf{u}_{ag}$, with \mathbf{u}_{ag} the first order in Ro velocity component. All other variable notations follow the same convention.

To reduce the order of complexity of the system, we consider the typical scaling variables (denoted by capital letters), which are also a consequence of the QG assumptions:

$$(x, y) \sim L, \quad z \sim H, \quad (u, v) \sim U, \quad f \sim f_0, \quad Ro = \frac{U}{Lf},$$

$$t \sim \frac{L}{U} \sim (Ro f)^{-1}, \quad \rho \sim \frac{\rho_0 f_0 U L}{gH},$$

where L and H are the characteristic horizontal and vertical lengths of the flow, respectively, and U is its characteristic velocity. ρ_0 and f_0 represent the reference fluid density and Coriolis parameter, respectively.

At the lowest order, Eq. (2.8) becomes $\nabla_H \cdot \mathbf{u}_g = 0$ since the geostrophic velocity field is nondivergent. Therefore, w is clearly not at the lowest order in Ro . This requires the vertical velocity to only appear from the next order:

$$w \sim Ro \frac{HU}{L}.$$

As a consequence the material derivative becomes $D/Dt = \partial_t + \mathbf{u} \cdot \nabla + Ro w \partial_z$.

Using these relations, we can rewrite the non-dimensional Boussinesq equations:

$$Ro \frac{D\mathbf{u}}{Dt} + \mathbf{k} \times \mathbf{u} = -\nabla_H \phi, \quad (2.11)$$

$$\frac{\partial \phi}{\partial z} = b, \quad (2.12)$$

$$\nabla_H \cdot \mathbf{u} + Ro \frac{\partial w}{\partial z} = 0, \quad (2.13)$$

$$Ro \left[\frac{Db}{Dt} + w \right] = 0. \quad (2.14)$$

Eqs. (2.12) and (2.14) can be rewritten in terms of temperature instead of buoyancy:

$$\frac{\partial \phi}{\partial z} = \theta, \quad (2.15)$$

$$Ro \left[\frac{D\theta}{Dt} + w \right] = 0. \quad (2.16)$$

We will continue using the equations expressed as a function of temperature in the subsequent analysis.

The geostrophic velocity is derived from the geostrophic balance at the lowest order:

$$u_g = \frac{-\partial \phi_g}{\partial y}, \quad v_g = \frac{\partial \phi_g}{\partial x}, \quad (2.17)$$

with the geopotential playing the role of a streamfunction. The thermal-wind balance relates the lowest-order horizontal velocity and temperature:

$$\frac{\partial u_g}{\partial z} = -\frac{\partial \theta_g}{\partial y}, \quad \frac{\partial v_g}{\partial z} = \frac{\partial \theta_g}{\partial x}, \quad (2.18)$$

relating the vertical gradient of the horizontal geostrophic flow to the horizontal gradient of the temperature field.

Taking Eqs. (2.11), (2.13) and (2.16) at next order in Rossby gives the vorticity and temperature equations:

$$\frac{D_g \zeta_g}{Dt} - \frac{\partial w_{ag}}{\partial z} = 0, \quad (2.19)$$

$$\frac{D_g \theta_g}{Dt} + w_{ag} = 0, \quad (2.20)$$

where $D_g/Dt = \partial_t + \mathbf{u}_g \cdot \nabla_H$ and $\zeta_g = \nabla_H^2 \phi_g$.

Eliminating the vertical motion from the above equations and using Eqs. (2.18), we retrieve the conservation of potential vorticity:

$$\frac{D_g q_{ag}}{Dt} = 0, \quad (2.21)$$

where the first order potential vorticity q_{ag} :

$$q_{ag} = \zeta_g + \partial_z \theta_g = \nabla_H^2 \phi_g + \partial_z^2 \phi_g. \quad (2.22)$$

At zeroth order, potential vorticity is equal to f , which, in nondimensional units, is 1. In the case of a 2D flow, where the flow is independent of the vertical direction, the inviscid 2D vorticity equation is recovered [Eq. (2.3) without the right-hand side term]. In fact, the full potential vorticity is conserved along the geostrophic flow and can be shown through a longer derivation [$D_g q/Dt = 0$] [5]. Here lies the importance of QG theory: it wraps up the entire system into a single equation with a single unknown. Unlike the Navier-Stokes equations, which provide six nonlinear partial differential equations with six unknowns. Up to order Ro , the potential vorticity can be in non-dimensional form estimated as follows

$$q \approx q_g + Ro q_{ag} = 1 + Ro \left(\nabla^2 \phi_g + \partial_z^2 \phi_g \right). \quad (2.23)$$

The last term on the right-hand side is the vortex stretching term. QG motions are horizontal, yet they generally vary in the vertical. It is a consequence of vertical motions and stratification in a water column.

Considering a rigid lid at the upper surface ($z = 0$) and consequently no normal flow ($w_{ag} = 0$) along the geostrophic flow, we obtain the conservation of temperature from Eq. (2.20), which is directly related to the conservation of buoyancy, such that

$$\frac{\partial \theta_g^{(s)}}{\partial t} + \mathbf{u}_g^{(s)} \cdot \nabla_H \theta_g^{(s)} = 0, \quad (2.24)$$

where $\theta_g^{(s)}$ and $\mathbf{u}_g^{(s)}$ are the temperature and the velocity at the surface at the

lowest order, respectively.

In this system, the conservation of both the total energy and the potential enstrophy leads to an inverse total energy cascade and a direct potential enstrophy cascade, highlighting the connection to 2D turbulent characteristics. The total energy E_{tot} is defined as

$$E_{tot} = \frac{1}{2} \iiint \left[\left(\frac{\partial \psi}{\partial x} \right)^2 + \left(\frac{\partial \psi}{\partial y} \right)^2 + \left(\frac{\partial \psi}{\partial z} \right)^2 \right] dx dy dz, \quad (2.25)$$

where $\psi = \phi_g$. The total energy can be divided into the kinetic energy and potential energy. The kinetic energy is derived from the horizontal motion of the flow, while the potential energy is related to buoyancy effects.

The potential enstrophy is defined as

$$Z_{pot} = \frac{1}{2} \iiint q^2 dx dy dz. \quad (2.26)$$

Eqs. (2.25) and (2.26) are a consequence of the conservation of potential vorticity. Energy cascades towards larger scales [inverse cascade] with an energy spectrum $E_{tot}(k) \sim k^{-5/3}$. Conversely, the potential enstrophy cascades toward smaller scales [direct cascade] with an energy spectrum $E_{tot}(k) \sim k^{-3}$ [31]. The characteristics of QG turbulence are well documented, i.e. [40]. The latter study highlights similarities between 2D and QG turbulence, such as the presence of an inverse energy cascade, a direct enstrophy cascade, and the emergence of strong coherent eddies in both systems. This theory has been applied successfully to ocean interior dynamics and has proved very successful in understanding energy exchange between scales and the interaction between oceanic eddies (see [5]).

2.3 Surface Quasi-Geostrophic (SQG) Theory

SQG is a special case of the QG approximation, initially introduced in an atmospheric context [41]. However, it has proven particularly useful for studying ocean submesoscale processes. Despite its simplifications, the SQG model captures essential features of surface-driven flows and provides insights into the

complex interactions that govern geophysical fluid dynamics [25]. In this model, PV is assumed to be zero in the interior; therefore, the dynamics are controlled by the advection of buoyancy at the surface [$q = 0$ in the interior]:

$$\nabla_H^2 \psi + \partial_z^2 \psi = 0, \quad (2.27)$$

The flow is driven by the evolution of surface temperature (or, equivalently, buoyancy):

$$\frac{D_g \theta_g^{(s)}}{Dt} = 0, \quad (2.28)$$

with the superscript (s) denoting quantities at the surface.

In the case of the ocean, we impose vertical boundary conditions on the streamfunction at $z = 0$ (corresponding to the ocean surface) and $z = -\infty$ such that

$$\theta_g^{(s)} = \frac{\partial \psi}{\partial z} \Big|_{z=0}, \quad (2.29)$$

$$\lim_{z \rightarrow -\infty} \frac{\partial \psi}{\partial z} = 0, \quad (2.30)$$

with $\psi = \phi_g$.

Using Eq. (2.27) and the above boundary conditions, we can relate the streamfunction to the temperature in the horizontal Fourier domain:

$$\widehat{\psi} = \frac{\widehat{\theta}_g^{(s)}}{k} e^{kz}, \quad (2.31)$$

where the hat denotes the horizontal Fourier transform and k for the horizontal wavenumber modulus. Equation (2.31) indicates that, for each Fourier component, the streamfunction decreases exponentially with z (note that $z < 0$). Notably, this decrease becomes more rapid for smaller horizontal scales (large k).

At the surface, the relation between the temperature and the streamfunction in Fourier space becomes:

$$\widehat{\theta}_g^{(s)} = k \widehat{\psi}^{(s)}. \quad (2.32)$$

Similar to 2D and QG systems, SQG systems are characterized by two con-

served quantities: the generalized energy E_G (also called total energy) and the generalized enstrophy Z_G (also called potential energy) [25, 42], defined as

$$E_G = \frac{1}{2} \iiint \left[\left(\frac{\partial \psi}{\partial x} \right)^2 + \left(\frac{\partial \psi}{\partial y} \right)^2 + \left(\frac{\partial \psi}{\partial z} \right)^2 \right] dx dy dz = -\frac{1}{2} \iint \psi^{(s)} \theta_g^{(s)} dx dy, \quad (2.33)$$

and

$$Z_G = \frac{1}{2} \iint \theta_g^2 dx dy, \quad (2.34)$$

At the surface, the kinetic energy E is proportional to the generalized enstrophy via a horizontal Fourier transform using Eq. (2.31) at $z = 0$,

$$\begin{aligned} E(z=0) &= \frac{1}{2} \iint |\mathbf{u}_g^{(s)}|^2 dx dy = \frac{1}{2} \iint k^2 |\widehat{\psi}^{(s)}|^2 dk_x dk_y \\ &= \frac{1}{2} \iint |\widehat{\theta}_g^{(s)}|^2 dk_x dk_y = \frac{1}{2} \iint \left(\theta_g^{(s)} \right)^2 dx dy = Z_G. \end{aligned} \quad (2.35)$$

In SQG turbulence, generalized energy undergoes an inverse cascade to larger scales. The surface kinetic energy spectrum and, equivalently, the buoyancy variance spectrum (due to Eq. (2.35)), in their corresponding inertial range, is

$$E(k) \sim k^{-1}, \quad (2.36)$$

while the generalized enstrophy undergoes a direct cascade to small scales. The (surface) kinetic energy spectrum in its corresponding inertial range is

$$E(k) \sim k^{-5/3}. \quad (2.37)$$

As with 2D and QG turbulence, these predictions are based on dimensional arguments [25, 42]. The forward and inverse cascades were observed in free-decaying SQG simulations [43].

SQG dynamics produce energetic small-scale flows, leading to a shallower kinetic energy spectrum scaling as $k^{-5/3}$ in the direct cascade, compared to k^{-3} in QG. These small-scale flows are considered one of the possible mechanisms for submesoscale generation via mesoscale straining processes. SQG flows are characterized by the presence of eddies of different sizes and filamentary struc-

tures [25]. These structures play an important role on marine ecosystems. Indeed, using an SQG model coupled with a plankton ecosystem model, it was shown that phytoplankton preferentially develop in these filamental structures [44].

However, SQG, like QG, assumes a geostrophic and nondivergent velocity field [Eq. (2.28)]. Consequently, it fails to capture some of the main ocean submesoscale characteristics, such as a cyclone/anticyclone asymmetry [22–24] and a divergent horizontal flow [18–21] (see also Sec. 1.2).

2.4 Next order in Rossby Submesoscale Model

To overcome the limitations of the QG framework, an interesting approach is to extend it to include ageostrophic motions by developing the primitive equations to the next order in the Rossby number. This extension results in the QG^{+1} system, which includes ageostrophic corrections [45, 46] that can potentially account for the missing submesoscale flow features. When applied to surface-driven dynamics, this approach leads to the SQG^{+1} model. Initially introduced in an atmospheric context [47], simulations of freely decaying turbulence demonstrated that it produces the expected cyclone-anticyclone asymmetry.

In this study, we utilize the SQG^{+1} system to explore surface-ocean turbulence at fine scales, focusing on the direct kinetic energy cascade, a topic that has not previously been addressed. Our primary objective is to provide a minimal model based on fundamental dynamical equations that can account for these submesoscale features. Additionally, we aim to investigate the impact of ageostrophic flow on the spatial distribution of tracer particles.

Other models, such as the surface semi-geostrophic model [48], also extend primitive equations by considering the finite Rossby number effect and successfully reproduce both cyclone-anticyclone asymmetries and strong vertical velocities at fronts. However, we selected the SQG^{+1} model because many of its properties are well-documented [47].

The full derivation of the SQG^{+1} equations starts with the QG^{+1} model, from which the SQG^{+1} system is obtained by setting the interior PV to zero. This involves a Helmholtz decomposition of the vector $\mathbf{V} = (\mathbf{k} \times \mathbf{u}, \theta) = (v, -u, \theta)$ into divergent and rotational components, $\mathbf{V} = \nabla\phi + \nabla \times \mathbf{A}$, leading to the horizontal

flow $\mathbf{u} = \mathbf{k} \times \nabla_H \phi - \partial_z \mathbf{A}$ and the temperature field $\theta = \partial_z \phi + \nabla_H \cdot \mathbf{A}$. Substituting these into the Boussinesq equations and expanding in Ro yields the QG⁺¹ equations after extensive calculations. For detailed derivations, refer to [45] and [46].

This section will briefly introduce the mathematical formulation of the SQG⁺¹ model, adapting the original derivation [47] to oceanic conditions. Assuming the vertical coordinate ranges from $-\infty < z \leq 0$, the dynamics are driven by the lateral advection of temperature (buoyancy) at the surface ($z = 0$). The main governing equation retains the same form as in the SQG system (corresponding to $Ro = 0$) and expresses the conservation of surface temperature along the surface flow. This can be written as

$$\frac{\partial \theta^{(s)}}{\partial t} + \mathbf{u}^{(s)} \cdot \nabla \theta^{(s)} = 0, \quad (2.38)$$

where, again, the superscript (s) indicates quantities evaluated at the surface ($z = 0$). For simplicity of notation, we have dropped the subscript g from the temperature variable in the previous equation. We will continue using θ instead of θ_g , since the temperature is always taken at the lowest order. The total velocity field is the sum of the geostrophic component \mathbf{u}_g (computed at the lowest order in Ro) and an ageostrophic component \mathbf{u}_{ag} (at next order in Ro) as a consequence of the expansion of Eq. (2.10):

$$\mathbf{u} = \mathbf{u}_g + Ro \mathbf{u}_{ag}, \quad (2.39)$$

with the ageostrophic component calculated as the sum of two terms, \mathbf{u}_ϕ and \mathbf{u}_a ,

$$\mathbf{u}_{ag} = \mathbf{u}_\phi + \mathbf{u}_a. \quad (2.40)$$

These velocities are obtained from the (expanded) scalar potential $\phi = \phi_g + Ro \phi_{ag}$ (where $\phi_g = \psi$) and a vector potential $\mathbf{A} = Ro \mathbf{A}_{ag}$ (it can be shown that $\mathbf{A}_g = 0$) as follows:

$$\mathbf{u}_g = \left(-\frac{\partial \phi_g}{\partial y}, \frac{\partial \phi_g}{\partial x} \right), \quad (2.41)$$

$$\mathbf{u}_\phi = \left(-\frac{\partial \phi_{ag}}{\partial y}, \frac{\partial \phi_{ag}}{\partial x} \right), \quad (2.42)$$

$$\mathbf{u}_a = -\frac{\partial A_{ag}}{\partial z}. \quad (2.43)$$

The functions ϕ_g , ϕ_{ag} and A_{ag} are related to surface and lower-order quantities through the following relations:

$$\widehat{\phi}_g = \widehat{\psi} = \frac{\widehat{\theta}^{(s)}}{k} e^{kz}, \quad (2.44)$$

$$\widehat{\phi}_{ag} = \frac{\widehat{\theta}^2}{2} - \frac{\widehat{[\theta^{(s)}(\partial_z \theta)^{(s)}]}}{k} e^{kz}, \quad (2.45)$$

$$\widehat{A}_{ag} = -\widehat{\theta \mathbf{u}_g} + \widehat{(\theta^{(s)} \mathbf{u}_g^{(s)})} e^{kz}. \quad (2.46)$$

Equations (2.44) and (2.45) follow from the requirement of having zero interior PV at all orders in Ro , while Eq. (2.46) is a form of the omega equation obeyed by vertical velocities (see also [25, 45, 47]). Note that \mathbf{u}_a has both a rotational and a divergent component from (2.46) while \mathbf{u}_ϕ is nondivergent.

SQG⁺¹ accounts for frontogenetic ageostrophic motions linked to next-order corrections to the geostrophic flow. Moreover, its idealized nature and relatively simple mathematical formulation represent a strong advantage. However, a notable limitation is its inability to account for other types of ageostrophic dynamics that deviate further from geostrophic equilibrium. Among these, high-frequency motions (internal gravity waves and tides), in particular, may be expected also to play a relevant role on submesoscale turbulence [49–51]. Another limitation, shared with SQG, is the absence of a seasonal cycle due to the lack of a mixed layer in the model.

2.5 Lagrangian Dispersion in Turbulent Flows

In the previous sections of this chapter, we have presented idealized models that simulate ocean flows from planetary scales to submesoscales, highlighting

some of their key characteristics (Sec. 2.1 to 2.3). We also introduced the model used in this study, which accounts for frontal ageostrophic motions and can better model ocean submesoscales (Sec. 2.4). These models provide an Eulerian representation of the flow. However, motivated by the SWOT mission and the fact that current experimental data on submesoscales come primarily from surface drifters, we shift our focus to Lagrangian statistics. SWOT measures SSH from which geostrophic velocity fields can be derived [5]. These velocity fields do not capture the full submesoscale flow, necessitating an assessment of their accuracy for Lagrangian applications. We address this by exploring the impact of ageostrophic motions on Lagrangian transport in SQG⁺.

Lagrangian dispersion has been investigated in both QG and SQG systems, revealing that large-scale structures dominate dispersion in QG, while in SQG, it is local due to the presence of smaller energetic scales in the direct cascade inertial range [52]. However, to our knowledge, there is no comprehensive study on Lagrangian transport in an idealized model that includes frontal ageostrophic motions.

Furthermore, understanding the impact of submesoscales on Lagrangian transport could have important applications for problems such as plankton dynamics (e.g., nutrient distribution) and pollutant dispersal (e.g., after an oil spill or plastic accumulation).

To address this gap, we analyze the dynamics of Lagrangian tracer particles in the turbulent flows produced by the model of Sec. 2.4. To qualitatively compare the main features of our results with those from ocean drifters, we restrict the motion to the surface. The particles move according to the following equation:

$$\frac{d\mathbf{x}_i}{dt} = \mathbf{u}(\mathbf{x}_i(t), t), \quad (2.47)$$

where $\mathbf{x}_i = (x_i, y_i)$ is the horizontal position of particle i with $i = 1, \dots, N_p$ (where N_p is the number of particles) and $\mathbf{u}(\mathbf{x}_i, t)$ is the total velocity, presented in Eq. (2.39), at its position.

In this section, we examine two main types of dispersion to assess Lagrangian turbulence: single-particle dispersion, which concerns the diffusion of a particle from its initial position (Sec. 2.5.1), and pair dispersion, which pertains to the

relative distance between two particles (Sec. 2.5.2). A comprehensive review of Lagrangian statistics and their geophysical applications can be found in [17]. Here, we focus on Lagrangian dispersion without delving into the Lagrangian dynamics related to potential clustering, which will be introduced and discussed in Chapters 4 and 5.

2.5.1 Single particle statistics

Let us start by defining the absolute dispersion $\langle A^2(t) \rangle$. This is the variance of the particle displacement relative to the mean position at a given time t , capturing the spread of particles from their average location over time:

$$\langle A^2(t) \rangle = \langle [\mathbf{x}_i(t) - \mathbf{x}_i(0)]^2 \rangle - \langle [\mathbf{x}_i(t) - \mathbf{x}_i(0)] \rangle^2. \quad (2.48)$$

where $\langle \cdot \rangle$ is the average over all particles. In the absence of a mean flow, the second term on the right-hand side vanishes.

At very short times, when $t \ll \tau_L$, where τ_L is the integral Lagrangian time, $\langle A^2 \rangle$ is expected to behave as

$$\langle A^2(t) \rangle \simeq \sigma_L^2 t^2, \quad (2.49)$$

where σ_L^2 is the total Lagrangian velocity variance. This is known as the ballistic regime, where trajectories still retain some memory of their initial conditions. At very large times, when $t \gg \tau_L$ and all memory of initial conditions is lost, $\langle A^2(t) \rangle$ scales diffusively,

$$\langle A^2(t) \rangle \simeq 2K_{abs}t, \quad (2.50)$$

where $K_{abs} = 1/2 d\langle A^2(t) \rangle/dt$ is the absolute diffusion coefficient.

The integral Lagrangian time τ_L can be estimated by integrating the autocorrelation function of the Lagrangian velocity $C(\tau)$ over the time scale over which the Lagrangian velocities are correlated or as the time of the first zero crossing of $C(\tau)$ with $C(\tau)$ defined as

$$C(\tau) = \frac{\overline{\mathbf{u}_i(t+\tau) \cdot \mathbf{u}_i(t)}}{\overline{\mathbf{u}_i^2(t)}}, \quad (2.51)$$

where the overbar denotes an average over time, $\mathbf{u}_i(t) = \mathbf{u}(\mathbf{x}_i(t), t)$ and τ the time lag from time t . $C(\tau)$ can be averaged over all particles in a homogeneous and isotropic system. Another interesting property of the autocorrelation function is its intrinsic connection to the kinetic energy spectrum. The Fourier transform of the temporal autocorrelation function is directly related to the temporal energy spectrum $E(\omega)$ (where ω is the angular frequency inversely proportional to time). This is a consequence of the Wiener-Krinchin theorem. Therefore, by calculating the autocorrelation function, we can also determine $E(\omega)$, providing important information on the frequency distribution of kinetic energy within the system. An exponentially decaying velocity autocorrelation results in a frequency spectrum characterized by an ω^{-2} decay at high frequencies (i.e., $E(\omega) \sim \omega^{-2}$) and a white spectrum at low frequencies (i.e., $E(\omega)$ is constant), with a transition frequency of $\omega = (2\pi\tau_L)^{-1}$ [17].

In fact, the behavior of absolute dispersion was observed using data from Lagrangian drifters released, for example, near the Brazil Current. At short times, we clearly observe ballistic dispersion where $\langle A^2(t) \rangle \sim t^2$. At larger times, absolute dispersion passes to the diffusive regime where $\langle A^2(t) \rangle \sim t$ [27].

2.5.2 Two-Particle statistics

While single-particle statistics provide insights into advective transport, primarily influenced by the largest and most energetic scales of motion, two-particle statistics offer valuable information about the physical mechanisms operating across various scales of motion.

In 1926, Richardson attempted to characterize the spreading of weather balloons in the atmosphere. He showed that particles in the atmosphere exhibit super-diffusion driven by turbulence; more interestingly, his results suggested that the mean-square relative displacement between two particles grows in time as t^3 [53]. The latter result came years before the famous Kolmogorov turbulence theory [29], yet it was shown to be a direct consequence of Kolmogorov scaling, in the inertial range of scales [54–56].

The mean-square relative displacement between two particles, i.e., relative

dispersion, is defined as

$$\langle R^2(t) \rangle = \langle |\mathbf{x}_i(t) - \mathbf{x}_j(t)|^2 \rangle, \quad (2.52)$$

where the average is computed at time t , over all pairs (i, j) such that at $t = 0$ (the release time) $|\mathbf{x}_i(0) - \mathbf{x}_j(0)| = R(0) = R_0$. Relative dispersion helps identify dispersion regimes, which is important for characterizing material spreading in a flow and for inferring flow properties, especially when working with drifter data.

At very short times, the relative dispersion grows ballistically as t^2 [52, 56, 57]. This follows from a Taylor expansion of the relative dispersion around $t = 0$:

$$\langle R^2(t) \rangle \simeq R_0^2 + \langle (\delta \mathbf{u}_0)^2 \rangle t^2, \quad (2.53)$$

where $\mathbf{u}_0 = \mathbf{u}(t = 0)$. For sufficiently small R_0 and assuming that velocity gradients are square-integrable, the second order structure function can be replaced by ZR_0^2 , where $Z = \langle \zeta^2/2 \rangle_x = \int k^2 E(k) dk$ is enstrophy; consequently, Eq. (2.53) can be simplified to $\langle R^2(t) \rangle \simeq R_0^2(1 + Zt^2)$.

At intermediate times, when pair separations lie in the inertial range of the flow, relative dispersion should grow exponentially or as a power law, if the kinetic energy spectrum scales as $k^{-\beta}$ with $\beta > 3$ or $\beta < 3$, respectively. The first case is generally referred to as a nonlocal dispersion regime, meaning that dispersion is dominated by the largest flow structures, and $\langle R^2(t) \rangle \sim \exp(2\lambda_L t)$, where λ_L is the maximum Lagrangian Lyapunov exponent, representing the mean exponential rate of divergence [58], defined as

$$\lambda_L = \lim_{t \rightarrow \infty} \lim_{R(0) \rightarrow 0} \frac{1}{t} \ln \left(\frac{R(t)}{R(0)} \right). \quad (2.54)$$

In the second case, dispersion is said to be in a local regime, meaning that it is controlled by flow features of size comparable with the distance between a pair of particles, and $\langle R^2(t) \rangle \sim t^{4/(3-\beta)}$ [17, 52]. At larger times, when the separation is larger than the largest eddy size, a diffusive scaling is expected due to uncorrelated particle velocities. In this diffusive regime, $\langle R^2(t) \rangle \sim 2K_{rel}t$,

where $K_{rel} = 2K_{abs}$ is the asymptotic value of the relative diffusivity [17].

The relative diffusivity can be derived directly from the relative dispersion:

$$K_{rel} = \frac{1}{2} \frac{d\langle R^2(t) \rangle}{dt}. \quad (2.55)$$

In the case of nonlocal dispersion, $K_{rel} \sim \langle R^2(t) \rangle$, while for local dispersion $K_{rel} \sim \langle R^2(t) \rangle^{(\beta+1)/4}$. In the diffusive regime, relative diffusivity converges to a constant value, $K_{rel} = 2K_{abs}$.

Another two-particle indicator that can be used to identify dispersion regimes is the kurtosis of the relative distance between particles in a pair [17, 52]:

$$ku(t) = \frac{\langle R^4(t) \rangle}{\langle R^2(t) \rangle^2}. \quad (2.56)$$

When dispersion is nonlocal, rapid (exponential) growth of $ku(t)$ is expected. For local dispersion, the kurtosis should be constant. At larger times, in the diffusive regime, the kurtosis reaches a constant value equal to 2.

Considering the SQG direct cascade, which is particularly relevant to our study, where $\beta = 5/3$, we retrieve Richardson scaling in the inertial range for the three indicators above:

$$\begin{aligned} \langle R^2(t) \rangle &\sim t^3, \\ K_{rel} &\sim R^{4/3}, \\ ku(t) &= 5.6. \end{aligned}$$

Note that in Kolmogorov turbulence and the QG and 2D turbulence inverse cascades, $\beta = 5/3$.

These indicators, known as fixed-time indicators, are commonly used in oceanography to study drifter behavior due to their ease of calculation. However, they depend highly on the initial separation distance $R(0)$ and the transition between different regimes. Additionally, capturing the expected local regime scaling requires a large inertial range spanning several decades [59]. Moreover, since these statistics are calculated at fixed times, the results can be difficult to interpret, as different pairs may have significantly different separations at the

same moment, leading them to follow different dynamical regimes [52, 60].

To address these limitations, fixed-scale indicators were developed, notably the finite-size Lyapunov exponent (FSLE) [59, 60]. The FSLE is a scale-by-scale dispersion rate and is defined as

$$\lambda(\delta) = \frac{\ln r}{\langle \tau(\delta) \rangle}, \quad (2.57)$$

where the average is over all pairs and $\tau(\delta)$ is the time needed for the separation to grow from δ to a scale $r\delta$ (with $r > 1$). Dimensionally, it is possible to relate the FSLE to the exponent β of the kinetic energy spectrum. For $\beta > 3$ (i.e., in the nonlocal dispersion regime), the FSLE should be constant, $\lambda(\delta) = \lambda_L$ [58, 59]. When dispersion is local ($\beta < 3$), it should have a power-law dependence $\lambda \sim \delta^{(\beta-3)/2}$, while in the diffusive regime one expects $\lambda(\delta) \sim \delta^{-2}$.

Part II

Methodology

Numerical Method

This chapter provides an overview of the numerical methods employed to simulate the SQG⁺¹ flows used to advect Lagrangian tracer particles. This chapter is divided into two primary sections: the Eulerian implementation in Sec. 3.1 and the Lagrangian implementation in Sec. 3.2.

3.1 Eulerian Implementation

The Eulerian fields are obtained from a code adapted from the original developed by [42] and previously utilized in [52, 61, 62]. The model evolution equations (Sec. 2.4) are numerically integrated using a pseudospectral method.

Fourier mode expansions, using complex exponentials as basis functions, deliver high accuracy and precision in numerical simulations. A major benefit is that, in Fourier space, differential operations are simplified to algebraic ones, making them computationally inexpensive. The high precision of the Fourier spectral method comes from its effective handling of spatial derivatives, where Fourier coefficients are multiplied by their corresponding wavenumbers, avoiding truncation errors typically found in finite difference schemes.

Despite this advantage, treating convolutions in Fourier space remains computationally intensive, with a $O(N^2)$ complexity. While this complexity can be reduced to $O(N^2/2)$ due to the reality condition on $u(x)$, it remains computationally demanding. The reality condition states that since $u(x)$ is real, then

$\widehat{u}(-k) = \widehat{u}^*(k)$, where $(u)k$ is the Fourier coefficient associated with wavenumber k and the asterisk denotes the complex conjugate. The pseudospectral approach is used to address this challenge, where linear terms are treated in Fourier space and nonlinear terms are computed in physical space. This method transforms the nonlinear terms to physical space for multiplication and then back to Fourier space, thereby reducing the computational cost to $O(N \log_2 N)$. This method's most computationally expensive part is applying Fast Fourier Transforms (FFTs) to switch between Fourier space and physical space. When using the Fourier transform, aliasing can cause high-frequency modes to be misrepresented on a discrete grid. Only the nonlinear terms are affected, and we address this through dealiasing. We truncate Fourier modes that lie outside a circle of radius $(2\sqrt{2}/3) \times (N/2)$ [63]. The inverse FFT is performed on $N/2$ points, and the modes where the Fourier coefficients correspond to $k^2 \geq (8/9) \times (N/2)^2$ are zero-padded, with k the wavenumber modulus.

The equations are integrated on a doubly periodic square domain of side $L_0 = 2\pi$ at resolution $N^2 = 1024^2$, starting from an initial condition corresponding to a streamfunction whose Fourier modes have random phases and small amplitudes. We consider the forced and dissipated version of Eq. (2.38):

$$\frac{\partial \theta^{(s)}}{\partial t} + \mathbf{u}^{(s)} \cdot \nabla \theta^{(s)} = \mathcal{F} + \mathcal{D}, \quad (3.1)$$

where \mathcal{F} is a random (δ -correlated in time) forcing acting over a narrow range of wavenumbers $4 \leq k_f \leq 6$ (and whose intensity is $F = 0.02$), and \mathcal{D} is the dissipation term. \mathcal{D} is composed of a hypofriction term $-\alpha \nabla_H^{-2} \theta$ to remove energy from the largest scales, and a hyperdiffusion term $-\nu \nabla_H^4 \theta$ to assure small-scale dissipation and numerical stability. The addition of forcing and dissipation allows reaching a statistically stationary flow state. This is verified by monitoring the energy and enstrophy in each simulation. For the dissipative terms, we set $\alpha = 0.5$ and we determine ν based on the condition $k_{max} l_\nu \gtrsim 6$, with l_ν the dissipative scale and $k_{max} = N/2 - 1$ (before dealiasing). These terms are estimated dimensionally for $Ro = 0$. This estimation is based on Kolmogorov-like

arguments [29, 64] applied to SQG such that

$$\nu \sim l_\nu^{10/3} F^{2/3}. \quad (3.2)$$

This is based on the consideration that the generalized enstrophy injection rate at large scales, its flux through the inertial range, and its dissipation rate are the same. In this system, since forcing is random and δ -correlated in time, the injection rate is proportional to F^2 through stochastic considerations of Eq. (3.1). These choices correspond to quite large dissipations and will limit the number of active scales; however, it turned out that they were necessary to control the numerical stability of the code at the largest Ro value explored. Indeed, integrating the SQG⁺¹ system is delicate due to the effective compressibility of the horizontal flow introduced by the ageostrophic corrections, which creates strong gradients that are difficult to resolve. These parameters were tested at resolutions $N^2 = 256^2, 512^2, 1024^2$. Figure 3.1 shows the energy spectra $E(k)$, computed from the full velocity for $Ro = 0.075$, at each resolution. As the resolution is increased, the inertial range expands, and smaller scales are resolved. The spectral slope remains relatively consistent across different resolutions, indicating that the dissipation terms do not significantly influence the inertial range.

Achieving a resolution of $N^2 = 2048^2$ was not possible with the condition $k_{max} l_\nu \leq 6$. A larger criterion would be required, hence a larger ν . As a result, the energy spectrum at 2048^2 closely resembled that at 1024^2 , with only a few additional scales resolved but at a significantly higher computational cost. Considering this and the minimal additional physical information gained, we chose to conduct our simulations at $N^2 = 1024^2$ as previously mentioned.

The surface-temperature evolution equation, Eq. (3.1), is advanced in time using a third-order Adams-Bashforth scheme. It is an explicit method that requires the knowledge of values at previous times. Considering $\partial_t \mathbf{u} = \mathbf{f}(\mathbf{u}, \mathbf{x}, t)$, the third-order Adams-Bashforth scheme can be formulated as:

$$\mathbf{u}_{n+1} = \mathbf{u}_n + \frac{dt}{12} (23\mathbf{f}_n - 16\mathbf{f}_{n-1} + 5\mathbf{f}_{n-2}) \quad (3.3)$$

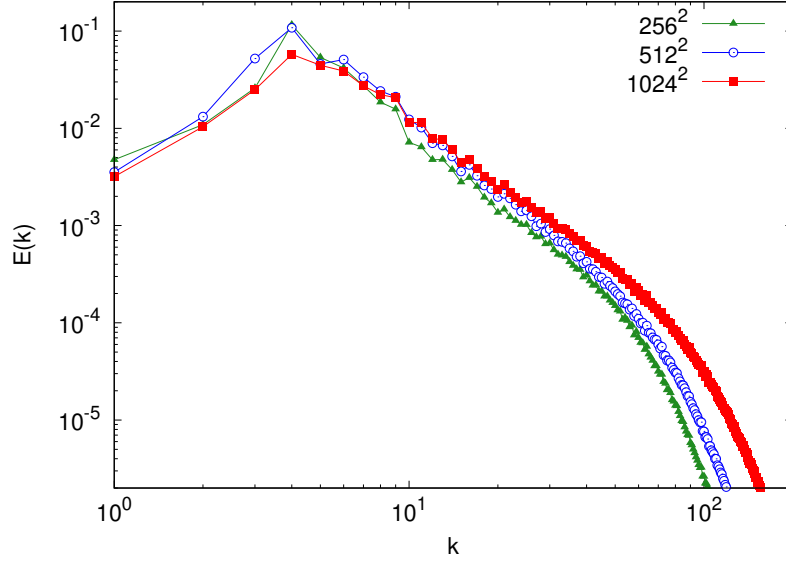


Figure 3.1: Kinetic energy spectra, temporally averaged over several flow realizations in the statistically steady state for $Ro = 0.075$ at resolutions $N^2 = 256^2, 512^2, 1024^2$.

where the subscript n denotes the current time.

We verified that the results are essentially unchanged when using a fourth-order Runge-Kutta algorithm. The latter is computationally less efficient, as it requires the computation of 4 coefficients for each new value, whereas the third-order Adams-Bashforth method reuses previously calculated values.

The time step was set to the quite small value $dt = 10^{-4}$, which was verified to ensure temporally converged results for different values of the Rossby number. Since this is the main control parameter, we performed different simulations, increasing it from $Ro = 0$ to $Ro = 0.075$ (with 0.0125 increments), the largest value we can safely reach.

Figure 3.2 shows the kinetic energy [panel (a)] and enstrophy [panel (b)] as a function of time, excluding the transient part. We see here that the system has reached a statistically steady state, allowing for studying its turbulent properties at different Rossby numbers and introducing Lagrangian tracer particles into the flows.

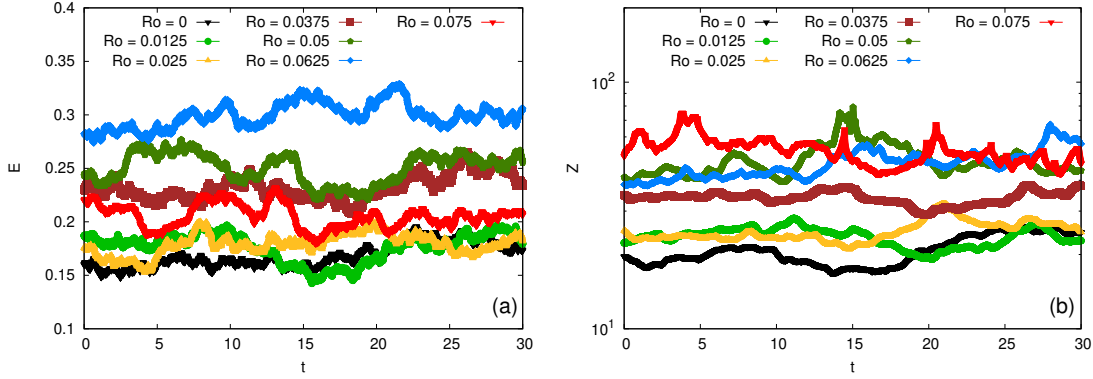


Figure 3.2: Kinetic energy (a) and enstrophy (b) as a function of time for the different Rossby numbers.

3.2 Lagrangian Implementation

We now consider the dynamics of Lagrangian tracer particles, governed by Eq. (2.47), in the turbulent flows produced by Eq. (3.1), both at $Ro = 0$ and at $Ro > 0$. Equation (2.47) is numerically integrated using a third-order Adams-Bashforth scheme, analogous to that described for Eq.(3.3), but applied to particle positions instead of velocity. Bicubic interpolation is used in space for the velocity field at particle positions [65], utilizing a 4×4 grid (grey dots) of surrounding points to interpolate a value within a smaller 2×2 grid, as shown by the red dots in Fig. 3.3.

Considering the grid configuration in Fig. 3.3, the interpolation can be performed using the following equation:

$$p(x, y) = \sum_{i=0}^3 \sum_{j=0}^3 a_{ij} x^i y^j, \quad (3.4)$$

where a_{ij} are the interpolation coefficients and $x, y = -1, 0, 1, 2$ are the grid point coordinates. The function $p(x, y)$ is also known as the interpolated surface.

Except where explicitly stated, we assume that the particle motion occurs in an infinite domain and use the spatial periodicity of the Eulerian flow to compute the Lagrangian velocities outside the computational box.

The temporal accuracy of the resulting trajectories was verified by varying

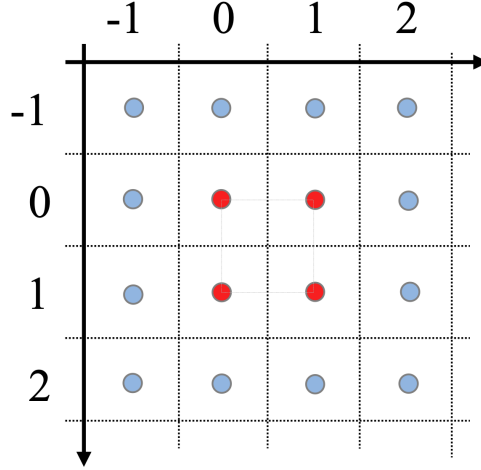


Figure 3.3: Illustration of a grid for bicubic interpolation. Blue dots are the 4×4 grid used to interpolate a value within the smaller 2×2 grid in red dots.

the time step and using the Lagrangian acceleration criterion proposed in [66], where its advantages and limitations are detailed. This criterion, $L(\mathbf{x}_i, t)$ (noted $F(\mathbf{a}, t)$ in [66], but changed here to avoid conflict of notation), is based on the differential equation governing the temporal evolution of the square of the norm of the absolute displacement vector. It establishes the relationship between the displacement, the velocity, and the acceleration of a Lagrangian tracer particle along its trajectory. $L(\mathbf{x}_i, t)$ is defined as

$$L(\mathbf{x}_i, t) = t \frac{d}{dt} A^2(\mathbf{x}_i, t) - A^2(\mathbf{x}_i, t) - t^2 |\mathbf{u}(\mathbf{x}_i, t)|^2 + \left| \int_0^t \tau \Gamma(\mathbf{x}_i, t) d\tau \right|^2. \quad (3.5)$$

The bias on the trajectory associated with the Lagrangian numerical scheme, in our case, the third-order Adams-Bashforth, can be considered negligible if $L(\mathbf{x}_i, t) \approx 0$. Figure 3.4a shows this criterion, averaged over all particles, for different values of Ro . Generally, $L(\mathbf{x}_i, t)$ remains small over time across the range of Ro values. Another method to quantify this bias is by defining a relative error ε_r as follows:

$$\varepsilon_r = \frac{|L(\mathbf{x}_i, t)|}{\frac{1}{4} \left(\left| t \frac{d}{dt} A^2(\mathbf{x}_i, t) \right| + A^2(\mathbf{x}_i, t) + t^2 |\mathbf{u}(\mathbf{x}_i, t)|^2 + \left| \int_0^t \tau \Gamma(\mathbf{x}_i, t) d\tau \right|^2 \right)}. \quad (3.6)$$

The relative error ε_r , shown in Fig. 3.4b, is of $O(10^{-6})$, or approximately 0.0001%,

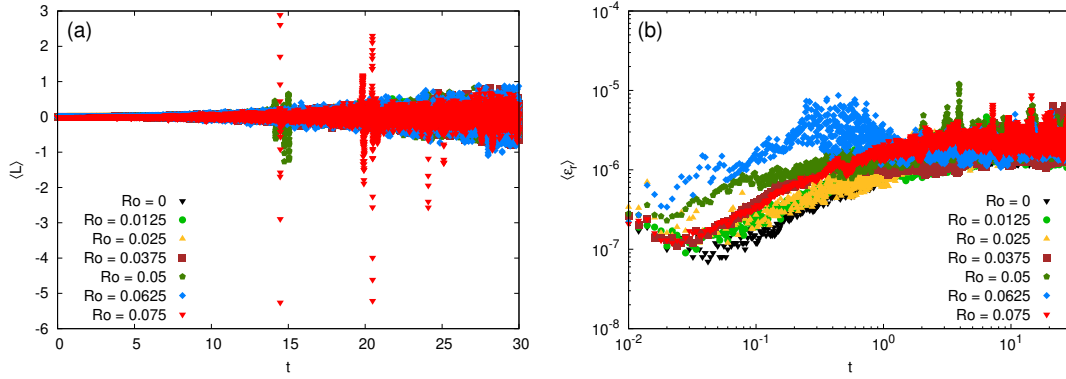


Figure 3.4: (a) Lagrangian acceleration criterion and (b) its relative error ε_r , both averaged over all particles, for different Rossby numbers. In panel (a), for $Ro \leq 0.0375$, $\langle L \rangle$ is sufficiently small and overshadowed by the larger Rossby numbers.

which is considered very low. This, along with the small value of $L(x_i, t)$, indicates that the bias on the trajectories is negligible.

A total of $N_p = 49152$ particles are seeded in the turbulent flows once the latter are at a statistically steady state (Fig. 3.2). Their initial positions correspond to a regular arrangement of $M = 128 \times 128$ triplets over the entire domain. This arrangement mimics the deployment of drifters in the ocean. Each triplet forms an isosceles right triangle with a particle pair along x and one along y , characterized by an initial pair-separation $R(0) = \Delta x/2$ (with Δx the grid spacing).

To compute dispersion statistics, only original pairs were used, which, in our case, amounts to 32768 pairs. These original pairs are formed by the particle pairs initially separated by a distance $R(0)$. The pair separation statistics were verified to not depend on the pairs' initial orientation (along x or y direction). This initial particle configuration also allowed us to confirm that the flow is isotropic by calculating the relative dispersion along the x and y directions, denoted $\langle R_x^2 \rangle = \langle (x_i - x_j)^2 \rangle$ and $\langle R_y^2 \rangle = \langle (y_i - y_j)^2 \rangle$, respectively, as presented in Fig. 3.5.

Moreover, provided that enough pairs are chosen, the results are mostly insensitive to their number. Figure 3.6 shows relative dispersion versus time for different numbers of pairs at $Ro = 0.075$. It is evident that 32768 pairs are

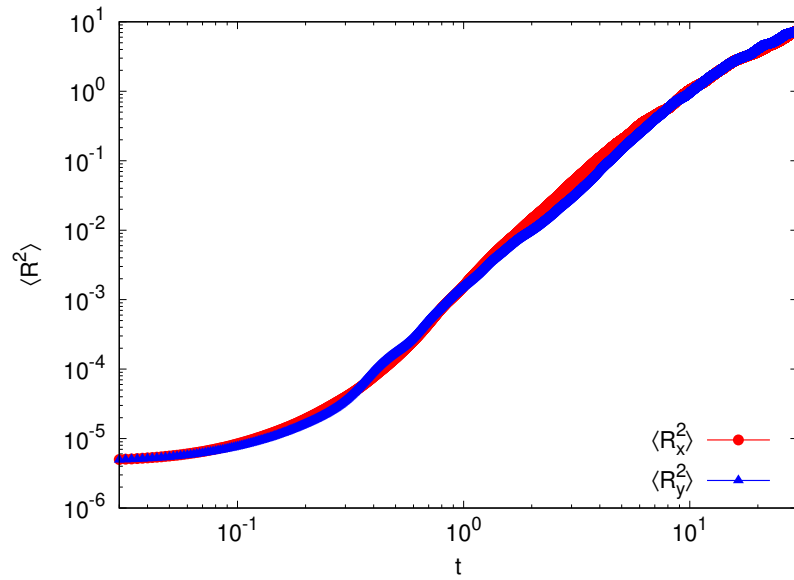


Figure 3.5: Relative dispersion, in the x and y direction, as a function of time for $Ro = 0.075$.

sufficient for the convergence of relative dispersion. Similarly, other time- and scale-dependent indicators used in this study have also demonstrated convergence in terms of the number of pairs. While Fig. 3.6 suggests that around 15000 particles (10000 pairs) would have been satisfactory for dispersion statistics, we opted for a higher number of particles (49152) to visualize particle distributions better and assess clustering. This choice accounts for the sensitivity of the clustering indicators introduced in the upcoming chapters while balancing computational time.

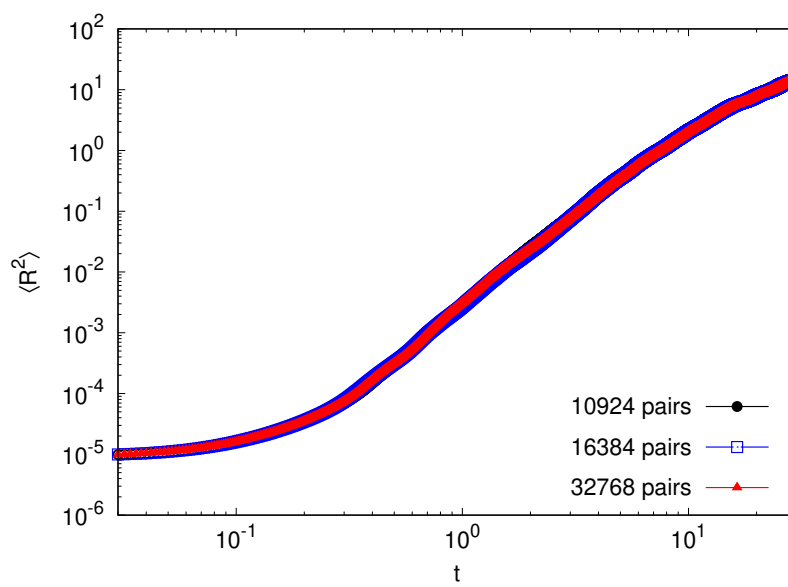


Figure 3.6: Relative dispersion as a function of time for $Ro = 0.075$ for different numbers of pairs.

Part III

Results

Particle dispersion and clustering in surface ocean turbulence with ageostrophic dynamics

This chapter explores the influence of ageostrophic motions on particle dispersion and clustering at the ocean surface, providing insights into Lagrangian transport properties. The research presented here is based on the article “Particle dispersion and clustering in surface ocean turbulence with ageostrophic dynamics” published in *Physics of Fluids* and coauthored with Guillaume Lapeyre, Bastien Cozian, Gilmar Mompean, and Stefano Berti [67].

Ageostrophic motions significantly influence submesoscale dynamics and are essential for understanding various associated phenomena. However, decoupling these motions from geostrophic ones is challenging, making it difficult to assess their specific impact on the flow and Lagrangian transport. Using numerical simulations of the SQG⁺¹ system (see Sec. 2.4), our objective is to study the processes governing particle behavior in surface ocean turbulence that include ageostrophic effects.

Our research focuses on how these dynamics impact pair-dispersion and clustering properties of Lagrangian tracer particles at the ocean surface. We performed different simulations by increasing the Rossby number from $Ro = 0$ to $Ro = 0.075$, the largest value we can safely reach (see Chap. 3 for more details).

The findings indicate that while large-scale eddies primarily drive the long-term pair-separation process, ageostrophic components significantly contribute to the formation of temporary particle aggregates. These results align with observational data [18–21] and underscore the importance of considering ageostrophic motions in models of ocean transport.

The implications of this work are broad, extending to the interpretation of upcoming high-resolution satellite data, such as that from the SWOT mission, which will provide unprecedented insights into the fine-scale structure of the ocean surface. By improving our understanding of particle transport dynamics, our results contribute to the broader goal of improving predictive models for marine and climate-related processes.

This chapter is organized as follows. In Sec. 4.1, we discuss the main features of SQG⁺¹ turbulent dynamics. The results of the analysis of Lagrangian particle statistics are reported in Sec. 4.2, where we separately characterize the role of ageostrophic motions on relative dispersion (Sec. 4.2.1) and clustering properties, as well as their relation with the flow structure (Sec. 4.2.2). Finally, discussions and conclusions are presented in Sec. 4.3.

4.1 Turbulent flow properties

In the following sections, we present the main characteristics of the turbulent flows for both $Ro = 0$ (SQG) and $Ro > 0$ (SQG⁺¹), which will be of interest for the dynamics of Lagrangian tracer particles.

4.1.1 Kinetic energy

When the Rossby number increases, starting from $Ro = 0$, the flow develops stronger and stronger gradients, and the total kinetic energy grows monotonically with Ro (Fig. 4.1). Its spatial structure is characterized by eddies of different sizes and, especially, by sharp fronts (see also Sec. 4.2). Note that in our simulations, $4 \leq k_f \leq 6$ (see Sec. 3.1). Within this range, the kinetic energy is predominantly influenced by the forcing. To mitigate any biases introduced by

the forcing, we perform the integration of $E(k)$ between $k_f = 6$ and k_{max} , thereby calculating the total energy as $E = \int_{k_f}^{k_{max}} E(k) dk$.

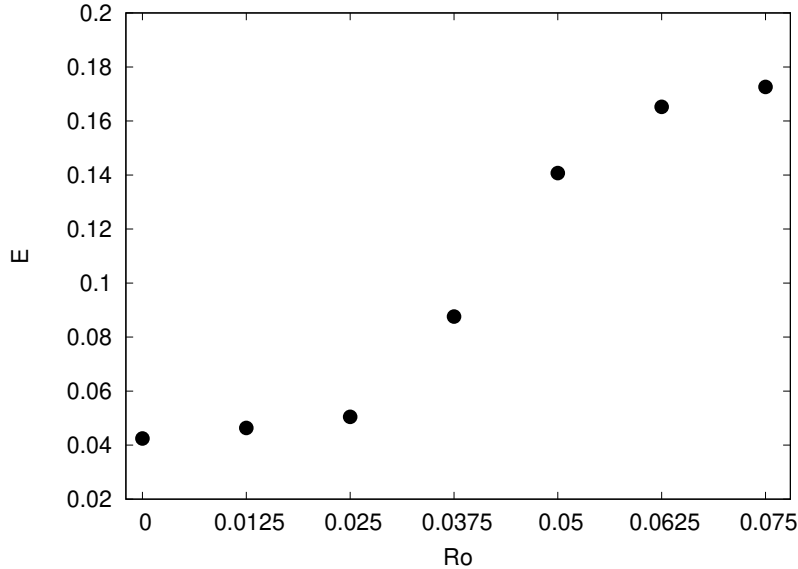


Figure 4.1: Kinetic energy, E , as a function of Ro . Here, the kinetic energy spectra, $E(k)$, are temporally averaged over several flow realizations in the statistically steady state.

Kinetic energy spectra $E(k)$ computed from the total velocity \mathbf{u} , for the smallest ($Ro = 0$) and the largest ($Ro = 0.075$) Rossby number are shown in Fig. 4.2. They display a scaling close to k^{-2} (see inset of Fig. 4.2) over about a decade. They are flatter than in QG barotropic dynamics, where $E(k) \sim k^{-3}$. However, they are slightly steeper than the theoretical prediction $k^{-5/3}$ for the direct cascade of buoyancy variance in the SQG system. This steepening effect is essentially independent of Ro and is more important at low wavenumbers, suggesting that its origin likely lies in the presence of large-scale persistent structures of size $\approx 2\pi/k_f$, as also noted in previous studies of SQG and SQG⁺¹ turbulence [25, 47, 61, 68].

At high wavenumber, the scaling range is limited by the large values of the dissipation coefficients, which are needed to control the formation of very intense gradients. At low wavenumbers, we do not observe the k^{-1} scaling corresponding to an inverse cascade in SQG, as the forcing acts on large scales and hypofriction is strong enough to dampen the energy below k_f .

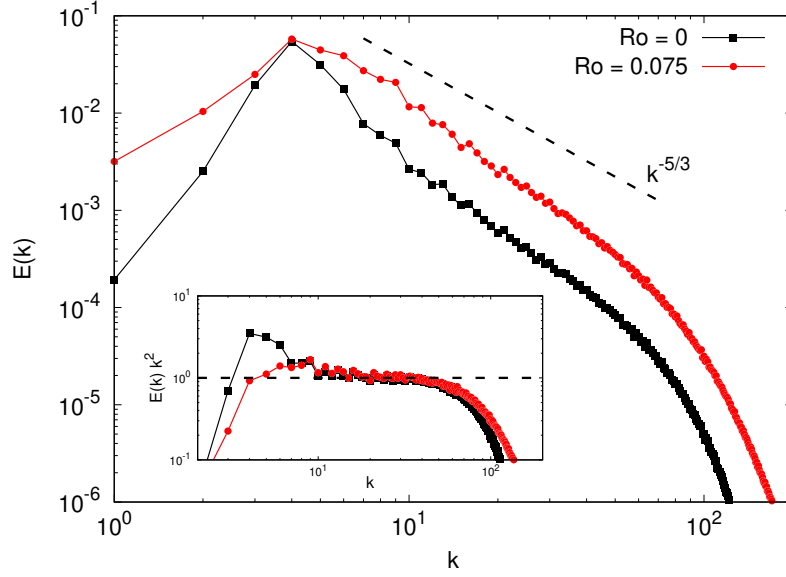


Figure 4.2: Kinetic energy spectra, temporally averaged over several flow realizations in the statistically steady state for $Ro = 0$ and $Ro = 0.075$. The dashed black line in the main panel corresponds to the expectation for SQG dynamics. Inset: the same spectra compensated by k^{-2} and rescaled with a coefficient such that, in both cases, the scaling range corresponds to the wavenumbers for which $E(k)k^2 \simeq 1$.

4.1.2 Vorticity statistics

As mentioned in Sec. 2.4, an important feature of oceanic (and atmospheric) flows, which is not captured by QG theory, is the asymmetry of vorticity statistics. This was detected in data from both observations [22, 24] and primitive-equation simulations [23, 69]. The latter numerical works also highlighted the role of surface dynamics on the prevalence of cyclonic over anticyclonic flow regions.

Different mechanisms can explain this asymmetry. A first one is related to nonlinear Ekman pumping. As the stress at the air-sea interface is proportional to the difference of winds and currents, it creates a surface drag causing the decay of ocean anticyclones [70, 71]. Another mechanism relies on the vortex-stretching term in the vorticity equation $\partial_t \zeta \sim (f + \zeta) \partial_z w + \dots$ for finite Rossby numbers. Here w is the vertical velocity, f the Coriolis frequency, and relative vorticity is defined as $\zeta = \partial_x v - \partial_y u$ [where $\mathbf{u} = (u, v)$ is the horizontal flow]. As discussed in previous works [3, 11, 47], at fronts, through the ageostrophic term $\zeta \partial_z w$, vortex stretching amplifies more cyclonic vorticity (on the heavy

side of the front) than anticyclonic vorticity (on the light side of the front). Note that within a purely QG framework vortex stretching would instead give a contribution to the vorticity growth rate ($\partial_t \zeta \sim f \partial_z w$) that is independent of the sign of ζ .

Clear asymmetry in favor of stronger cyclones is observed in QG⁺¹ and SQG⁺¹ models in which next-order corrections in Ro to QG equations are included [45, 47]. It was argued that the symmetry is broken because the divergence due to ageostrophic frontogenesis at small scales accelerates (slows down) the contraction of dense (light) filaments [47, 72], which gives rise to intense and localized cyclones, and weaker more broadly spread anticyclones. Moreover, it was shown that, from the mathematical viewpoint, the asymmetry arises from the quadratic dependency of the vector potential A [defined by Eq. (2.46)], from which the divergent velocity is obtained, on the geostrophic streamfunction [46]. In our forced simulations of SQG⁺¹ turbulence, cyclones prevail over anticyclones whenever $Ro > 0$, and vorticity statistics are similar to those in decaying SQG⁺¹ turbulence at fixed Rossby number [47]. The probability density function (pdf) of ζ , rescaled by its standard deviation s_ζ and averaged over time, is shown in Fig. 4.3 for $Ro = 0$ and $Ro = 0.075$. As it can be seen in the figure, the right tail of the pdf ($\zeta > 0$) is much higher than the left one ($\zeta < 0$) when $Ro = 0.075$, while the two tails essentially overlap over a whole range of $|\zeta|$ values for $Ro = 0$. The skewness of the vorticity distribution $S_\zeta = \langle \zeta^3 \rangle / \langle \zeta^2 \rangle^{3/2}$ grows, approximately quadratically, with Ro (see inset of Fig. 4.3), indicating that the magnitude of the asymmetry increases with the intensity of the ageostrophic flow.

Based on the results in this section, the SQG⁺¹ simulations considered here appear appealing to explore the transport and dispersion properties of Lagrangian tracers in turbulent flows, relevant for surface-ocean dynamics and possessing (weakly) ageostrophic components.

4.2 Lagrangian dynamics

We now consider the dynamics of Lagrangian tracer particles in the turbulent flows produced by the SQG⁺¹ model, both at $Ro = 0$ and at $Ro > 0$.

An illustration of typical particle spatial distributions, at a given instant of

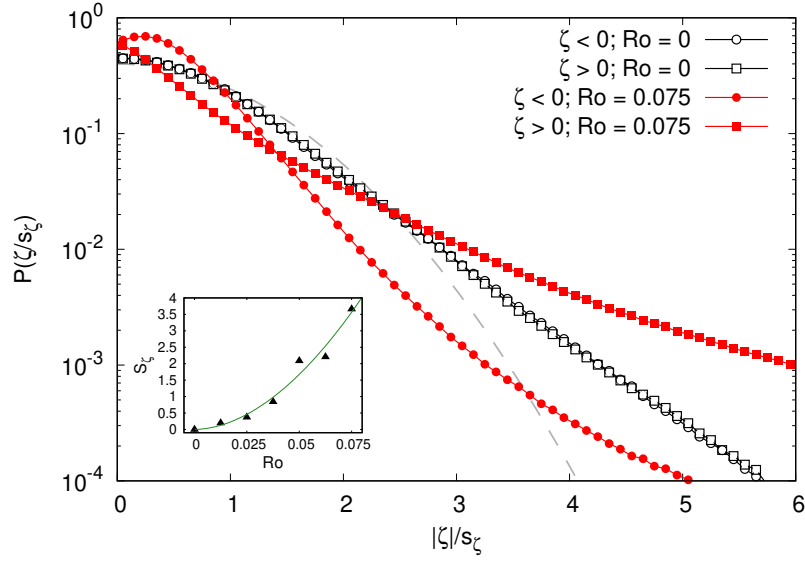


Figure 4.3: Probability density function of vorticity ζ (rescaled by its rms value s_ζ), temporally averaged over several flow realizations in the statistically steady state, for $Ro = 0$ (empty black points) and $Ro = 0.075$ (filled red points), with different point types indicating $\zeta > 0$ and $\zeta < 0$. For reference, the standard Gaussian distribution is also shown (dashed gray curve). Inset: vorticity skewness S_ζ as a function of the Rossby number; the solid green line corresponds to $S_\zeta \sim Ro^{1.87}$.

time in the statistically steady state of the flow, is shown in Fig. 4.4 for both $Ro = 0$ and $Ro = 0.075$, together with the corresponding vorticity fields. Here, particles are placed back in the original doubly periodic domain to see the effect of accumulation in space (while we assume that they leave this domain when computing dispersion statistics). Independently of the value of Ro , vorticity is characterized by quite a filamentary structure in addition to almost elliptical vortices of various sizes. For nonzero Ro cyclonic eddies ($\zeta > 0$) are more coherent than anticyclonic ones ($\zeta < 0$), and vorticity is globally more intense in root-mean-square (rms) value (Fig. 4.5). Concerning particles, it is here apparent that at $Ro = 0.075$ they do not uniformly spread over the spatial domain (as is the case for $Ro = 0$), which highlights the occurrence of clustering. In the following, we will separately address the characterization of their relative dispersion process and of their aggregation properties in the flow for varying Rossby number.

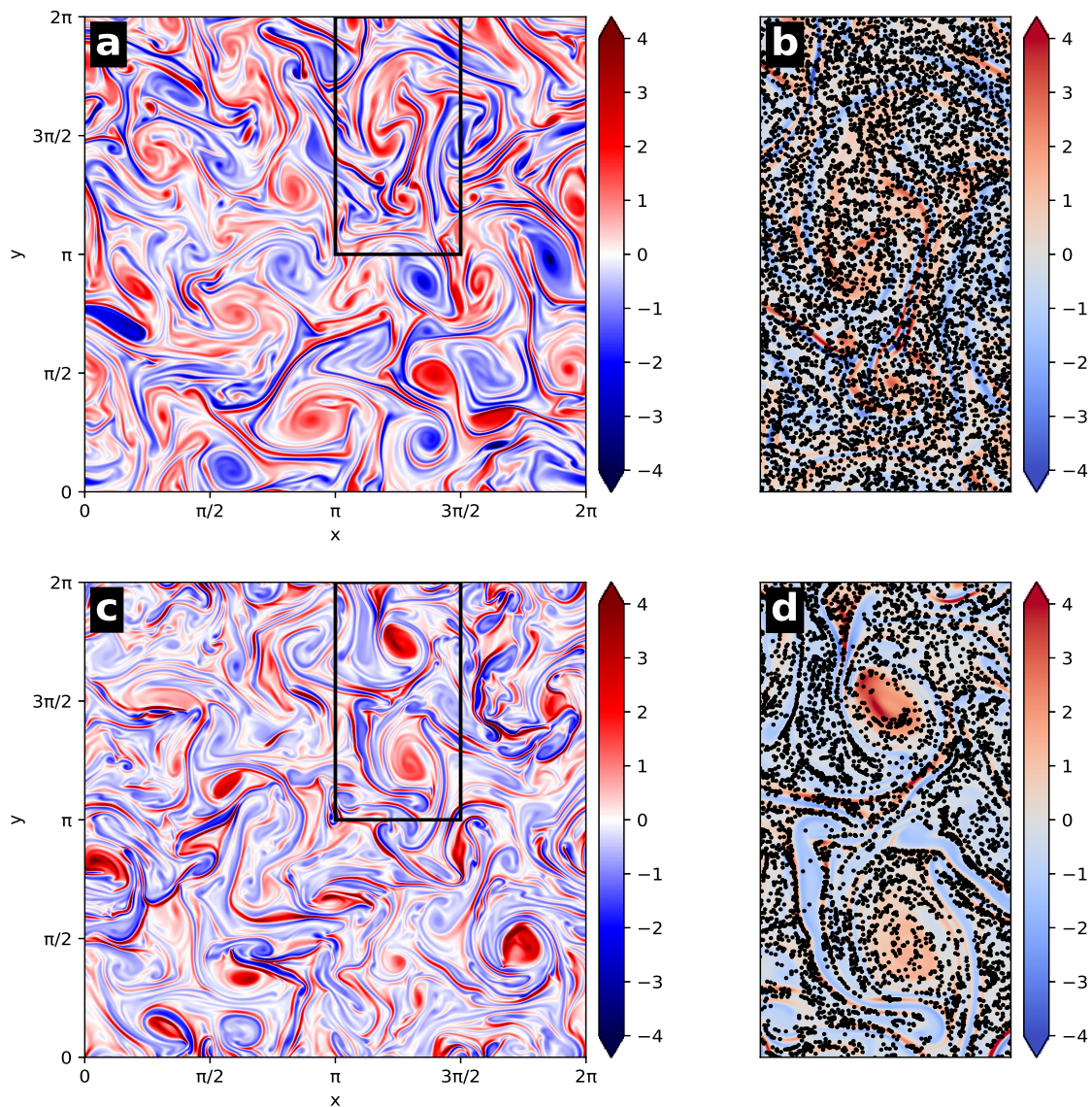


Figure 4.4: Vorticity normalized by its rms value for $Ro = 0$ (a) and $Ro = 0.075$ (c) at a fixed instant of time in statistically stationary conditions. Panels (b) and (d) show a closeup view of the region in the black rectangle in the main panels (a) and (c), respectively, including the particle distribution at that time.

4.2.1 Pair-dispersion statistics

In this section, we examine the effect of varying the Rossby number on particle pair dispersion using both fixed-time and fixed-scale indicators. The latter typically allows better for disentangling contributions from different flow scales [27,

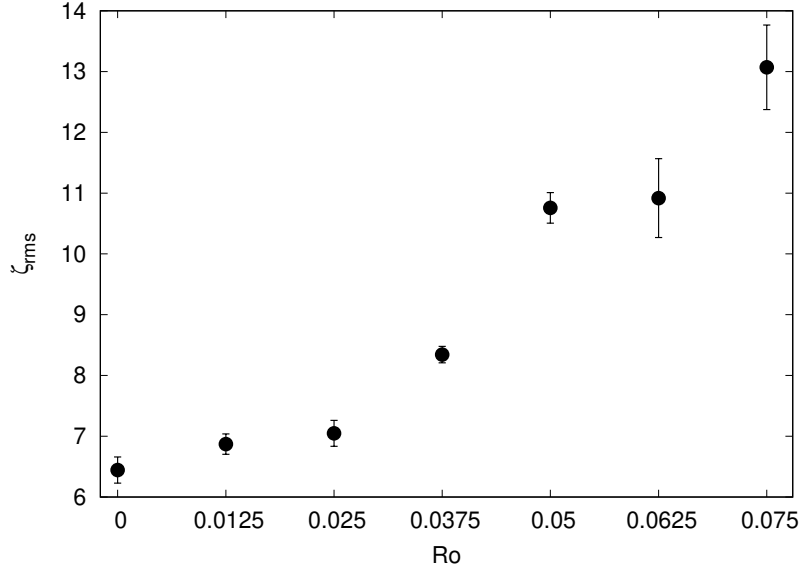


Figure 4.5: Root-mean-square of vorticity (ζ_{rms}) as a function of the Rossby number, averaged over several flow realizations in statistically steady conditions. The error is computed as the difference between the average over the full dataset and over half the dataset.

52, 59, 60]. We then mainly focus on the scale-by-scale dispersion rate by computing the FSLE [Eq. (2.57)].

As detailed in Sec. 2.5.2, in a nonlocal dispersion regime, which is normally associated with a steep kinetic energy spectrum of the flow [$E(k) \sim k^{-\beta}$, with $\beta > 3$], the FSLE is expected to attain a scale-independent, constant value. This is reflected by an exponential growth of the relative dispersion [Eq. (2.52)]. In a local dispersion regime, associated with turbulent flow possessing energetic small scales [$E(k) \sim k^{-\beta}$, with $\beta < 3$], both the FSLE and relative dispersion are expected to display power-law behaviors: $\lambda(\delta) \sim \delta^{(\beta-3)/2}$ and $\langle R^2(t) \rangle \sim t^{4/(3-\beta)}$, respectively. At separations larger than the largest flow scales, or at very large times, the FSLE scales as $\lambda(\delta) \sim \delta^{-2}$ and relative dispersion as $\langle R^2(t) \rangle \sim t$. Another indicator that may be used to discriminate between different dispersion regimes is the kurtosis of the separation distance [Eq. (2.56)]. Under nonlocal dispersion, $ku(t)$ should grow exponentially in time, while for local dispersion, it should attain a constant value (equal to 5.6 for Richardson dispersion, expected for $\beta = 5/3$) at intermediate times [52, 73]. At very large times, the kurtosis should in any case converge to $ku = 2$ corresponding to the diffusive limit of

dispersion [52, 73].

The FSLE measured in our simulations for different values of the Rossby number is shown in Fig. 4.6. Independently of Ro , the curves are remarkably flat at small separations and approach the diffusive behavior at the largest ones [larger than the flow integral length scale $\ell_I = 2\pi \int_0^\infty k^{-1}E(k)dk / \int_0^\infty E(k)dk$]. The slight deviations from the expected δ^{-2} scaling are here likely due to the limited inertial range of our turbulent flows. Indeed, previous studies reported similar observations in simulations with reduced inertial ranges and proposed using an alternative, pdf-based indicator [74] to improve the agreement with the large-scale theoretical prediction.

No clear evidence of a power-law scaling $\lambda(\delta) \sim \delta^{-1/2}$ [following from a kinetic energy spectrum $E(k) \sim k^{-2}$] is detected, except perhaps on a narrow range of intermediate separations (see inset of Fig. 4.6). This result suggests that the dispersion process is essentially nonlocal. This is also confirmed by the temporal evolution of the kurtosis (Fig. 4.7), which displays fast growth at short times and approaches 2 at large times. At intermediate times, $ku(t)$ never approaches a constant plateau, corresponding to a local dispersion regime. This behavior, pointing to nonlocal dispersion while local dispersion would be expected, may appear quite surprising. Interestingly, it bears some resemblance to measurements of drifter separation in the Gulf of Mexico [75, 76] once inertial oscillations are removed. One possibility to explain it is related to the presence of large-scale coherent structures in the flow, which can provide a dominant contribution to the dispersion process [68]. To test this hypothesis, we rescale the FSLE with the flow integral timescale $T_I = \ell_I / \sqrt{E}$, with E the total kinetic energy. As it can be seen in Fig. 4.6, for all Ro , the plateau values of the rescaled FSLE range between 1.1 and 0.8, which are close to 1, supporting this explanation.

The values of FSLE (not rescaled by T_I) at small δ slightly increase with the Rossby number (inset of Fig. 4.6), consistently with the increase of velocity gradients with Ro . A similar trend is observed from the short-time behavior of relative dispersion, which grows faster for larger Ro (inset of Fig. 4.7). At later times, $\langle R^2(t) \rangle$ does not present a clear scaling, though on a limited time interval; it may not be far from the t^4 theoretical expectation. More interestingly, its growth slows down when the Rossby number is increased, which hints at

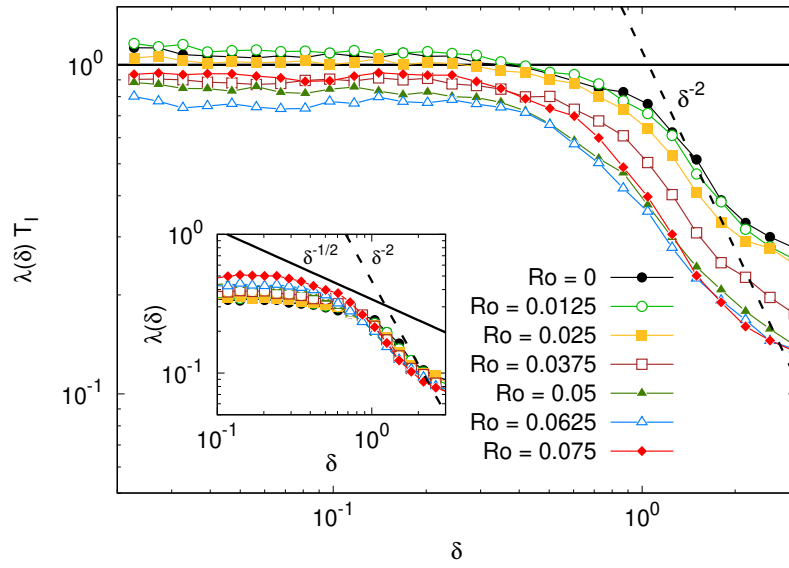


Figure 4.6: FSLE (rescaled by the flow integral time scale) for different Rossby numbers. Inset: the same without rescaling the FSLE. The $\delta^{-1/2}$ scaling law is the dimensional prediction for a kinetic energy spectrum $E(k) \sim k^{-2}$. The scale amplification factor is $r = 1.2$, and it was verified that the results are robust with respect to the choice of this parameter value.

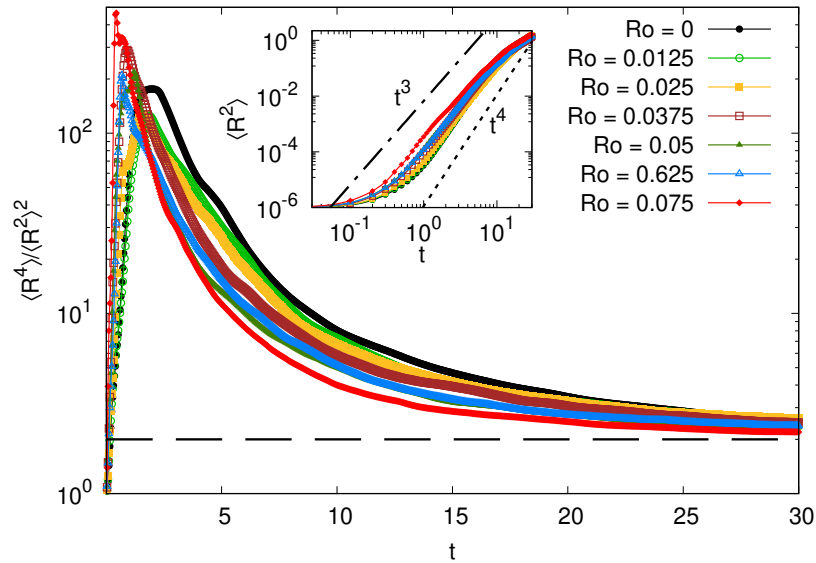


Figure 4.7: Kurtosis of particle relative displacements (main panel) and relative dispersion (inset) as a function of time for different Rossby numbers. The t^3 (Richardson dispersion) and t^4 scaling laws in the inset are the expectations for a kinetic energy spectrum $E(k) \sim k^{-5/3}$ and $E(k) \sim k^{-2}$, respectively.

temporary phases during which some particles aggregate, and thus, the efficiency of the global separation process is reduced.

We conclude that the Ro -dependence of the different measures of pair separation is overall weak, indicating that ageostrophic motions do not substantially alter pair-dispersion statistics. This suggests that, in this system, when the Rossby number is increased, large eddies conserve their capacity to drive the dispersion process.

4.2.2 Particle clustering and relation with the Eulerian flow structure

While on average, over long times, Lagrangian tracers separate, their spatial distribution is not homogeneous and clusters can form in the course of time. To investigate this point, the first quantity we consider is the averaged divergence experienced by particles along their trajectories, also known as the dilation rate [19], a numerically efficient single-particle indicator of tracer accumulation.

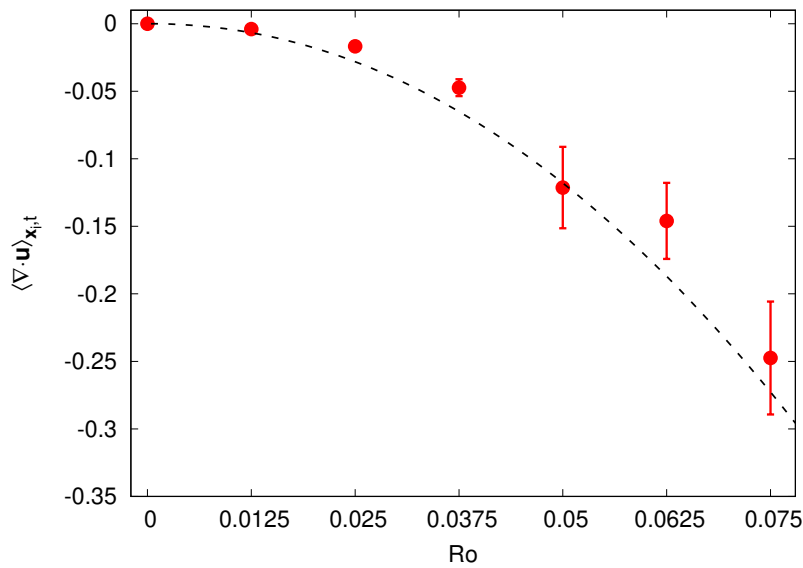


Figure 4.8: Velocity divergence sampled by particles, averaged over time and over all particles, as a function of the Rossby number. Here the error bars correspond to the standard deviation of the temporal statistics. The black dashed line is proportional to $-Ro^\alpha$, with $\alpha \approx 2.07$ from a best fit.

The divergence of the velocity field $\langle \nabla \cdot \mathbf{u} \rangle_{x_i, t}$, computed at particle positions \mathbf{x}_i and averaged over time and all particles, is shown as a function of Ro in Fig. 4.8. It is negative for nonzero Rossby numbers and grows roughly quadratically in Ro in absolute value, indicating that particles aggregate more when ageostrophic motions are more intense. Due to the compressibility they experience, particles are attracted to contracting flow regions and, hence, do not homogeneously sample the phase space. This fact has been shown to give rise to differences between Lagrangian and Eulerian statistics in other situations, such as that of time-correlated compressible flows [77, 78]. A qualitative understanding of what occurs in our experiments can be obtained by looking at the pdf of the Eulerian divergence, $P(\nabla \cdot \mathbf{u})$ (Fig. 4.9). When Ro is increased, the tails of this pdf rise, highlighting the more likely occurrence of very intense divergence events. Its shape is remarkably symmetric, though, meaning that positive and negative values of $\nabla \cdot \mathbf{u}$ are equally probable. The negative sign of the averaged Lagrangian divergence $\langle \nabla \cdot \mathbf{u} \rangle_{x_i, t}$ then results from particles getting trapped in convergence regions and spending a significant fraction of the time there. This phenomenon increases in intensity with the increase in Rossby number. The

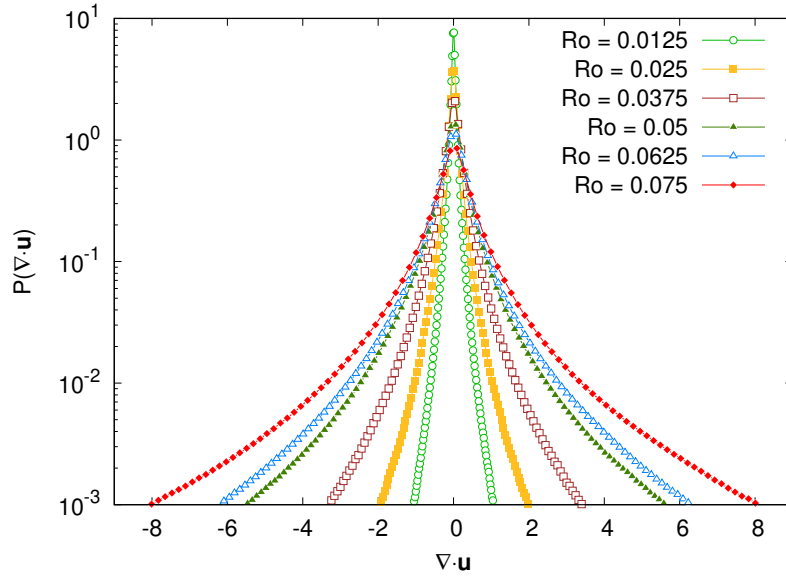


Figure 4.9: Probability density function of the Eulerian flow divergence $\nabla \cdot \mathbf{u}$, temporally averaged over several flow realizations in the statistically steady state, for different values of Ro .

occurrence of clustering in our system is clearly demonstrated by the pdf of

Voronoi normalized cell areas. This statistical tool is often used to characterize the aggregation of inertial particles in (incompressible) turbulent flows [79, 80]. The cells are constructed by partitioning the spatial domain into regions containing one particle and all the points closer to that particle than any other [79–81]. The nonhomogeneity of the particle distribution produces deviations of the pdf $P(A/\langle A \rangle_{x_i})$ (the average being taken over all areas, containing each one particle) from the corresponding one computed for uniformly random distributed particles. As it can be seen in Fig. 4.10, for $Ro = 0$, $P(A/\langle A \rangle_{x_i})$ agrees with the probability distribution expected for uniformly spread particles in a 2D domain [82], $f_{2D}(A/\langle A \rangle_{x_i}) = 343/15\sqrt{7/(2\pi)}(A/\langle A \rangle_{x_i})^{5/2} \exp(-7/2A/\langle A \rangle_{x_i})$ (solid gray line in the figure). However, when the Rossby number increases, its left tail gets monotonically higher, indicating that the probability of finding particles at small distances and, hence, observing clustering is larger. We can contrast the case of $Ro = 0.075$ with one where we advect particles by its geostrophic component only. As expected from particle transport in geostrophic turbulence [83], the pdf corresponding to uniformly distributed particles is recovered [case of $(Ro = 0.075)_g$ in Fig. 4.10], which further proves that this phenomenon is entirely due to the ageostrophic flow component.

Aiming to understand where particles accumulate, we first look at the fine-scale properties of clustering. The latter originates from the contraction of volumes in the phase space (here coinciding with the physical space) of the dissipative ($\nabla \cdot \mathbf{u} < 0$) dynamical system of Eq. (2.38). Consequently, after a transient, the Lagrangian dynamics take place on a fractal set. A common quantitative indicator of clustering is the correlation dimension [84], D_2 , of the dynamical attractor. A decrease to values $D_2 < d$, with d the dimension of the physical space ($d = 2$ in the present case), indicates an increased occurrence of small distances separating particle pairs. This fractal dimension is defined as:

$$D_2 = \lim_{r_p \rightarrow 0} \frac{\log[C(r_p)]}{\log(r_p)}, \quad (4.1)$$

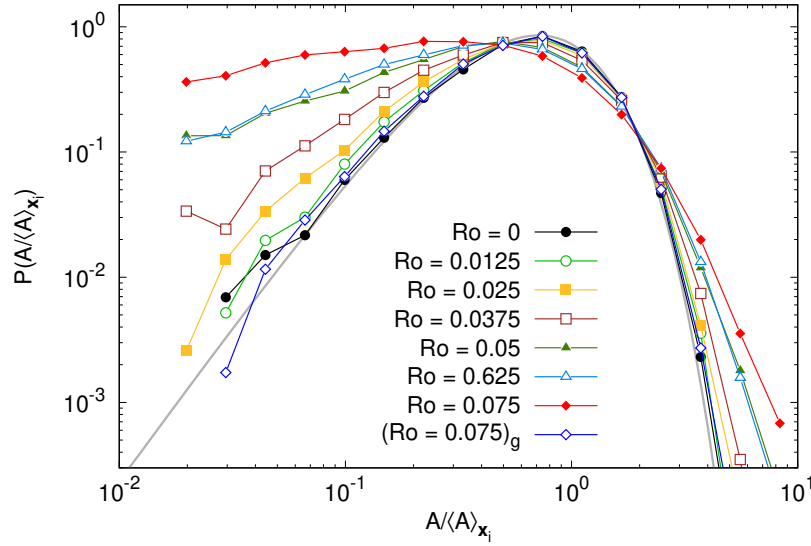


Figure 4.10: Probability density function of Voronoi cell areas, normalized by the averaged cell area, $P(A/\langle A \rangle_{x_i})$, at an instant of time in the statistically steady flow state, for different values of the Rossby number. The curve labeled by $(Ro = 0.075)_g$ has been obtained from particles advected by the geostrophic flow only. The solid gray line is the theoretical prediction for uniformly distributed particles $f_{2D}(A/\langle A \rangle_{x_i})$ (see text).

with the correlation sum $C(r_p)$ given by

$$C(r_p) = \lim_{N_p \rightarrow \infty} \frac{2}{N_p(N_p - 1)} \sum_{i,j>i}^{N_p} \Theta(r_p - |\mathbf{x}_i - \mathbf{x}_j|),$$

where Θ is the Heaviside step function, \mathbf{x}_i and \mathbf{x}_j are the positions of particles belonging to pair (i, j) , and the distance $|\mathbf{x}_i - \mathbf{x}_j|$ is the shortest one, after taking into account the 2π -periodicity of the computational box. Equation (4.1) then means that, for small r_p , the probability to find particle pairs separated by a distance less than r_p scales as $C(r_p) \sim r_p^{D_2}$.

Figure 4.11 shows the measurement of the correlation dimension as a function of the Rossby number. For $Ro = 0$, as expected, $D_2 = 2$ within statistical accuracy, which confirms the spatially homogeneous distribution of particles in the SQG system. Here, the small deviation from the theoretical value 2 may be attributed to the finite number of particles. At nonzero values of Ro , D_2

decreases monotonically, highlighting that clustering now takes place and that its intensity grows with the Rossby number. Again, this is a direct consequence of the transport of Lagrangian tracers by the ageostrophic flow. Indeed, when advection is realized by the geostrophic velocity only in the SQG⁺ model, the nonhomogeneity of the particle distribution disappears and $D_2 \simeq 2$, as shown by the blue empty point in the figure for the highest value of Ro explored (but the same holds for all Ro). Overall, these results suggest that particles aggregate on flow structures with a dimensionality smaller than that of the physical space and progressively more unidimensional with increasing Ro .

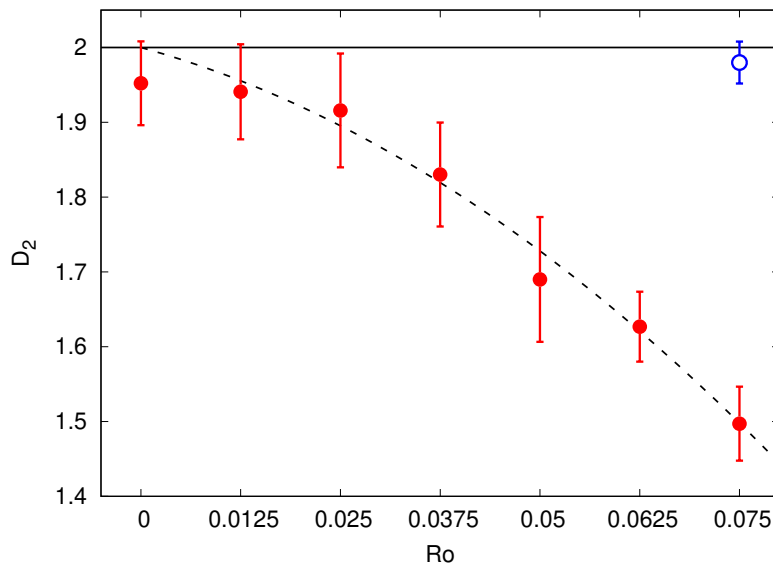


Figure 4.11: Correlation dimension D_2 as a function of Ro , obtained from data in several statistically steady flow realizations. Uncertainties are estimated from the standard deviations of best fits over the range of small distances r_p where $C(r_p) \sim r_p^{D_2}$. The empty blue point is for particles advected by the geostrophic flow component only at $Ro = 0.075$. The black dashed line corresponds to the second-order Taylor expansion $D_2 \simeq 2 + aRo + bRo^2$, with $a \simeq -2.9$ and $b \simeq -50.2$ from a fit.

We now discuss in what regions of the flow particles tend to cluster. This question is of primary importance in oceanography, e.g. to identify areas of pollutant accumulation in surface flows, or locations of intense vertical velocities relevant for nutrient upwelling and plankton dynamics.

While inspection of Fig. 4.4d already suggests some tendency of particles to avoid negative-vorticity (anticyclonic) regions and to concentrate along fila-

mentary structures, a more quantitative approach is needed. A classical tool to identify different (2D) flow regions, and to characterize their role in transport phenomena, is the Okubo-Weiss parameter [85, 86],

$$Q = \sigma^2 - \zeta^2, \quad (4.2)$$

where $\sigma = \sqrt{\sigma_n^2 + \sigma_s^2}$ is the total strain ($\sigma_n = \partial_x u - \partial_y v$ and $\sigma_s = \partial_x v + \partial_y u$ being the normal and shear strain, respectively) and ζ is vorticity. The parameter Q allows to discriminate between strain-dominated ($Q > 0$, i.e., $\sigma > |\zeta|$) and rotation-dominated ($Q < 0$, i.e., $\sigma < |\zeta|$) regions, and reveals useful, for instance, to explain the dynamics of tracer-field gradients [87, 88]. Note that a more refined criterion was obtained in incompressible flows to account for the rotation of the strain eigenvectors that can affect the straining properties [89]. These strain and rotation-dominated regions can be related to dispersion properties through the linearization $d(\mathbf{x}_i - \mathbf{x}_j)/dt = \mathbf{u}_i - \mathbf{u}_j \simeq (\nabla \mathbf{u})(\mathbf{x}_i - \mathbf{x}_j)$. It is then clear that velocity gradients will also determine the particle's small-scale dispersion or aggregation properties. A similar interpretation can be derived by computing the eigenvalues of the velocity-gradient tensor, which, for a 2D flow, can be written as:

$$\mu_{\pm} = \frac{1}{2}(\Delta \pm \sqrt{Q}), \quad (4.3)$$

where $\Delta = \nabla \cdot \mathbf{u}$. From Eq. (4.3), one sees that, independently of the sign of Q , divergent flow ($\Delta \neq 0$) determines the decrease ($\Delta < 0$) or increase ($\Delta > 0$) of the separation distance between pairs of particles. It is also worth noting, however, that the most important effects for Lagrangian-tracer convergence are expected when $\Delta < 0$ and $Q > 0$ (i.e. for strain overcoming vorticity), in which case $\mu_- = -(|\Delta| + \sqrt{Q})/2$.

In order to determine the regions where particles preferentially cluster, we follow [90] and compute the flow divergence conditionally averaged over all grid points of the domain with given values of vorticity and strain, noted $\overline{\Delta}^{\zeta, \sigma}$. This is a robust statistical tool originally introduced to investigate the vertical fluxes of a passive scalar field in submesoscale turbulence [90]. Figure 4.12a shows its measurement in our SQG⁺¹ simulations for $Ro = 0.075$ at the same instant of time chosen for the visualization of Fig. 4.4d (but it was verified that its features

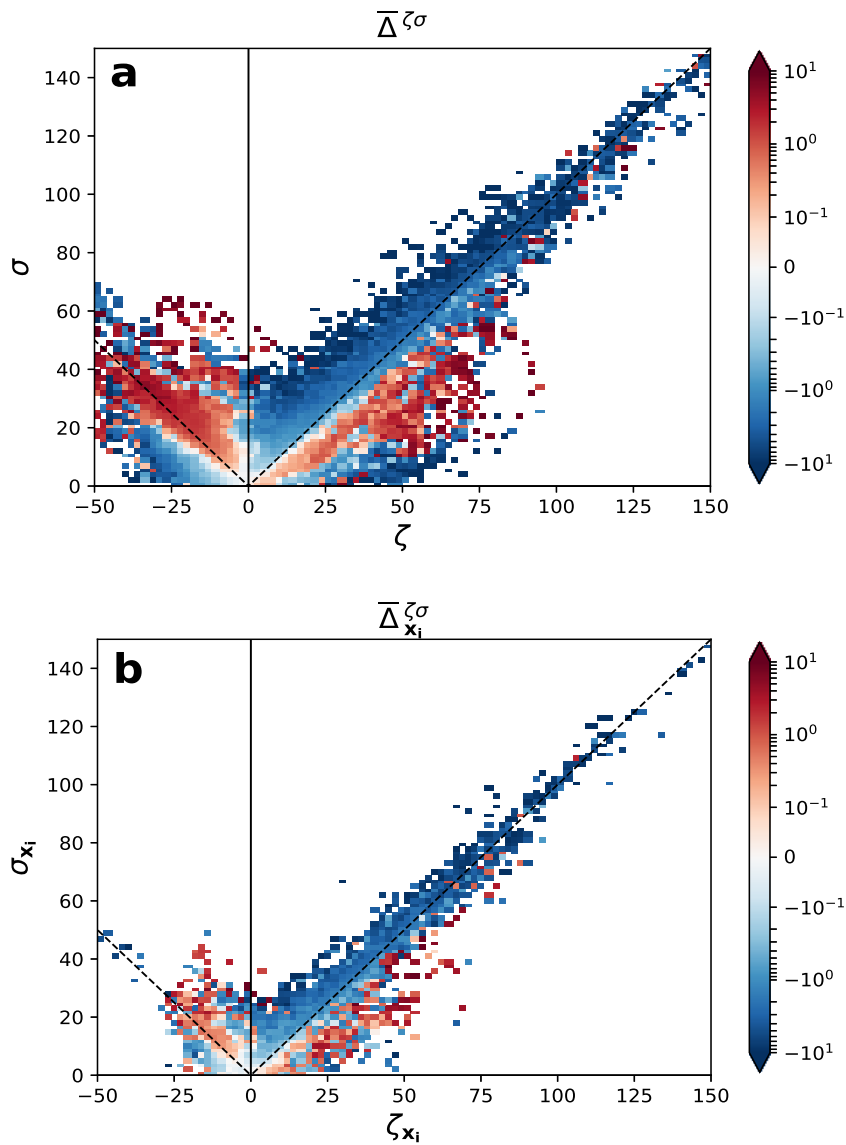


Figure 4.12: Mean divergence $\overline{\Delta^{\zeta\sigma}}$ conditionally averaged over vorticity (ζ) and strain (σ), from Eulerian (a) and Lagrangian (b) statistics, at a fixed instant of time in the statistically steady state of the flow, for $Ro = 0.075$. For the Lagrangian estimate, the subscript x_i indicates that Δ , ζ and σ are computed at particle positions. In both (a) and (b) the dashed lines correspond to $\sigma = |\zeta|$.

do not change significantly when a time average is also taken, see Fig. C.1). It is here apparent that strong divergence ($\overline{\Delta^{\zeta\sigma}} > 0$) and convergence ($\overline{\Delta^{\zeta\sigma}} < 0$) predominantly occur in strain-dominated regions ($\sigma > |\zeta|$), extending along tails above the lines $\sigma = |\zeta|$. The asymmetric shape of the tails is a direct consequence of the dominance of cyclonic vorticity (see Fig. 4.3) due to ageostrophic dynamics.

Here, the association of convergence with $\zeta > 0$ values is arguably due to the same vortex-stretching effects that amplify cyclonic vorticity (Sec. 4.1.2). Note, too, that in rotation-dominated regions ($|\zeta| > \sigma$), the divergence $\overline{\Delta}^{\zeta\sigma}$ is more likely to take both positive and negative values that tend to cancel out more. The above features are generic and also appear at smaller values of Ro (Fig C.1), except that the tails associated with large positive and negative values of $\overline{\Delta}^{\zeta\sigma}$ become more symmetric, and divergence is smaller in absolute value, when the Rossby number is decreased.

To complete the picture, we also show in Fig. 4.12b the divergence, in vorticity-strain space, computed at particle positions, $\overline{\Delta}_{x_i}^{\zeta\sigma}$. The Rossby number and the instant of time are the same as in Fig. 4.12a (and, again, we verified that averaging over time does not considerably modify the results, refer to Fig. C.2). By comparing Fig. 4.12a and Fig. 4.12b, it is evident that the Lagrangian and Eulerian estimates of divergence conditionally averaged over the values taken by vorticity and strain share the same general characteristics (similarly to what is found for vertical velocity in [91]). The partial attenuation of extreme events when using Lagrangian statistics is likely due to the smaller sample. Apart from this, it can be noted that the patterns from the Lagrangian estimate are sharper and characterized by a reduced frequency of $\overline{\Delta}^{\zeta\sigma} > 0$ events, in comparison with those from the Eulerian estimate. This is due to the tendency of particles to aggregate in flow-convergence regions and, hence, to predominantly sample negative values of divergence. Overall, Fig. 4.12b confirms the preference of Lagrangian tracers to concentrate in regions of positive vorticity and large strain ($\sigma > |\zeta|$). This finding quite nicely matches the spatial organization of particles that is observed from a closeup view of a portion of the full domain at the same instant of time (Fig. 4.4d). Indeed, regions of negative vorticity ($\zeta < 0$) tend to be relatively particle-free. On the contrary, particles are abundant in filamentary, positive vorticity regions (corresponding to $\zeta > 0$ and $\sigma > \zeta$), while it is less the case inside cyclonic eddies (corresponding to $\zeta > 0$ and $\sigma < \zeta$).

The previous analysis indicates that particle clustering takes place in cyclonic strain-dominated regions. These correspond mostly to filaments and fronts outside coherent eddies. Indeed, a straight front along the y direction [with velocity $\mathbf{u} = \mathbf{u}(x)$ independent of y (see Fig. 4.13)] is characterized by negative

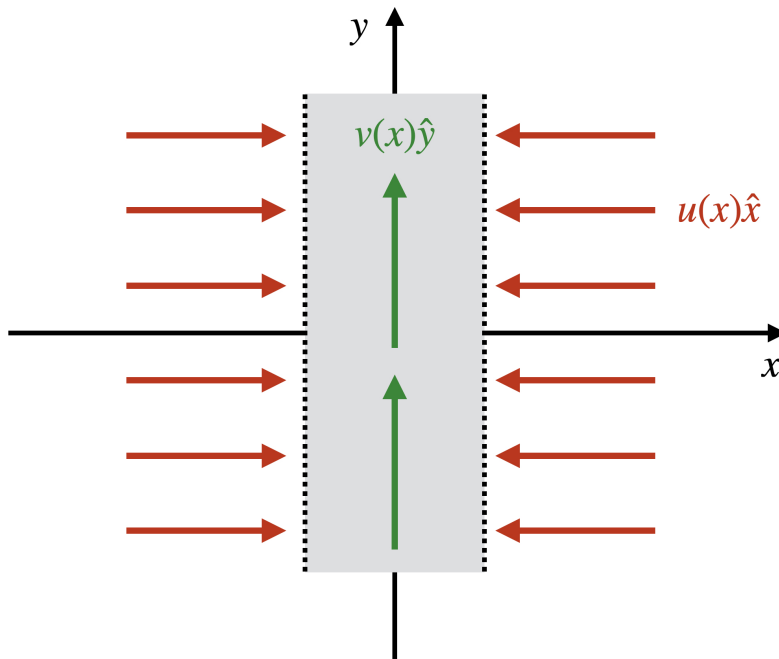


Figure 4.13: Sketch of an ideal straight front. The red and green vectors represent the velocity $u(x)$ and $v(x)$ respectively. \hat{x} is unit vector in the x direction and \hat{y} is unit vector in the y direction. The velocity components in an ideal straight front are independent of y .

divergence ($\nabla \cdot \mathbf{u} = \partial_x u < 0$) in its cross-front direction (which sustains the front) and by strain exceeding vorticity. The fact that $\sigma > |\zeta|$ follows from the relation $\sigma^2 = (\nabla \cdot \mathbf{u})^2 + \zeta^2 > \zeta^2$ holding for a velocity field that only depends on the cross-front coordinate x .

Our findings support those from a recent, more complex modeling study, which, from an Eulerian perspective, reported on strong vertical velocities and flow convergence in cyclonic submesoscale fronts [90]. Furthermore, they provide clear evidence of Lagrangian-tracer clustering in cyclonic regions, also observed from real surface-drifter data [18, 92], and a possible explanation of the basic mechanisms controlling the phenomenon in the framework of a minimal model accounting for ageostrophic dynamics.

4.3 Conclusions

We studied Lagrangian particle dynamics in an idealized model of surface-ocean turbulence that includes ageostrophic motions by means of numerical simulations. We particularly focused on the effect of ageostrophy on the spreading process of tracer particles by examining both relative dispersion and clustering properties.

The turbulent dynamics were assumed to be described by the SQG⁺¹ system, which accounts for frontogenetic ageostrophic motions and is obtained from a development of primitive equations to next order in Ro , with respect to standard QG models. This approach, originally introduced in an atmospheric context [47], allowed us to reproduce the cyclone-anticyclone asymmetry, a phenomenon that is observed in both primitive-equation simulations [23] and data from observations [22, 24] of ocean turbulence at sufficiently fine scales, but is missed by QG models. The turbulent flows from our simulations for different Rossby numbers are characterized by energetic small scales, particularly in the form of filamentary structures associated with intense gradients. Kinetic energy spectra are not far from the theoretical expectation in the SQG system (recovered by setting $Ro = 0$ in the governing equations), although slightly steeper. Their scaling behavior is close to $E(k) \sim k^{-2}$, as also found at submesoscales in more realistic simulations [93–95]. In the present case, the steepening of the spectrum is most likely due to the presence of large-scale coherent structures, a feature that was already observed in both the SQG [25, 68] and the SQG⁺¹ systems [47].

To explore how ageostrophic fluid motions impact the particle separation process, we compared the measurements from different indicators of pair dispersion as a function of Ro . Given that the total kinetic energy increases when increasing Ro , we used mostly dimensionless diagnostics, allowing a fair comparison between the different simulations. We found that irrespective of the Rossby number, dispersion is essentially nonlocal, except perhaps on a narrow range of separations, as highlighted by the extended region of scale-independent FSLE and by the fast initial growth in a time of the kurtosis of relative displacements. As the FSLE, where constant, was found to be close to the inverse large-eddy turnover time of the flow, we could show that this apparently surprising result is

due to the presence of large persistent flow structures, which dominate the dispersion process. Overall, the general picture emerging from different metrics of relative dispersion is that, in the present simulations, dispersion only weakly depends on the intensity of the ageostrophic flow dynamics (i.e., Ro). Nevertheless, when increasing Ro , the latter manifest in a small, but measurable, increase of the separation rate at short times (and small distances), due to velocity gradients becoming stronger, and in a subsequent slowdown of relative dispersion at later times, possibly arising from the formation of temporary particle aggregations.

The occurrence of clustering events was demonstrated by computing the averaged divergence experienced by particles (the dilation rate [19]), and the pdf of cell areas from a Voronoï tessellation. The decrease of the dilation rate to more and more negative values, and the rise of the left tail of the Voronoï cell-area pdf, indicate that particles are progressively more likely to be at small distances one from the other when Ro is increased. While this phenomenon is a direct consequence of the compressibility of the ageostrophic flow component, it is not straightforward to relate Eulerian and Lagrangian measures of clustering, as already noted in previous studies of Lagrangian tracer dynamics in compressible turbulence [77, 78]. Here, at a qualitative level, we argued that clustering arises from the increased probability of very large flow divergence values at larger Ro , and hence the longer fraction of time spent by particles in negative-divergence regions.

Determining where convergence, and thus particle clustering, takes place in surface-ocean flows is of paramount importance, both to predict the accumulation of biogeochemical substances or pollutants and to identify locations of large vertical velocities. To address this question, we first computed the correlation dimension of the sets over which particles concentrate, which is directly related to the probability of finding a pair of them within a given distance. With increasing Ro , this was found to decrease from $D_2 = 2$ (corresponding to uniformly distributed particles) to smaller values, indicative of clustering and pointing to less than 2D aggregates (possibly quasi-one-dimensional ones, for large enough Rossby numbers). To further understand in what flow regions clusters can be found, we examined the divergence conditionally averaged over vorticity and strain. This quantity was recently introduced as a generalization

of the Okubo-Weiss parameter to divergent flows to partition 2D flows into regions with different stirring properties [90]. We found that divergence has an asymmetric distribution in vorticity-strain space that reflects the cyclone-anticyclone asymmetry. More interestingly, it is predominantly negative and large (in absolute value) where strain overcomes vorticity, and the latter is positive, which indicates that clusters form in cyclonic frontal regions. Such a picture agrees with the results in more realistic simulations of submesoscale dynamics in the Antarctic Circumpolar Current, focused on the vertical fluxes of tracer fields [90]. It may also be useful to better understand observations of surface-drifter clustering in cyclonic regions in the Gulf of Mexico [18].

To conclude, the SQG⁺¹ system revealed a useful minimal model to investigate some basic mechanisms related to ageostrophy, controlling the separation and clustering of Lagrangian tracer particles at the ocean surface. Ageostrophic effects only weakly affect the nonlocal relative dispersion, while they are responsible of non-negligible clustering in filamentary cyclonic regions. This is remarkably similar to the observations from drifters in the Gulf of Mexico, which also indicated both nonlocal dispersion [75] and small-scale clustering [18]. Note that, in addition to ageostrophy, in the real ocean, other processes play a role in the transport of particles in the surface layer, such as Ekman currents induced by the wind [96], or Stokes drift due to ocean waves. The dispersion of floating material may also be affected by inertial effects [97] or by the drag exerted by the wind (the so-called windage). A natural perspective of this study is to extend the analysis to simulations from general circulation models to explore the effects of the ocean's fast variability, which cannot be accounted for by the modeling framework considered here (see Chapter 6).

Finally, the present results appear to us interesting in consideration of the satellite data at high spatial resolution acquired by the SWOT spatial mission [98]. The weak dependence of pair-dispersion indicators on the Rossby number suggests that the geostrophically derived surface velocities may be essentially accurate for relative-dispersion applications. On the other hand, to access finer details of the particle dynamics, such as clustering phenomena, further information on the ageostrophic flow components would clearly be required.

Impact of ageostrophic dynamics on the predictability of Lagrangian trajectories in surface-ocean turbulence

In the previous chapter, we investigated the effect of ageostrophic motions on Lagrangian tracer trajectories by varying Ro . Here, instead, we artificially filter the ageostrophic dynamics from the SQG⁺¹ flows by removing, *a posteriori*, the ageostrophic component (\mathbf{u}_{ag}) from Eq. (2.39). Throughout this chapter, we distinguish between the full flow and the filtered (geostrophic only) flow using the subscripts f and g , respectively. We focus on Lagrangian predictability, comparing trajectories of particles advected by either the full flow or its geostrophic part only. The research presented here is based on the article “Impact of ageostrophic dynamics on the predictability of Lagrangian trajectories in surface-ocean turbulence” published in *Physical Review Fluids* and coauthored with Guillaume Lapeyre and Stefano Berti [99].

In this chapter, our primary objective is to dispose of an idealized modeling framework to assess the accuracy of velocity fields similar to those derived from satellites like SWOT. While SWOT-derived velocity fields are geostrophic by construct, they may be influenced by ageostrophic processes at submesoscales. This

is somewhat analogous to the dynamic coupling between surface temperature and velocity fields in the SQG⁺¹ system, leading to the fact that filtering SQG⁺¹ flows is not equivalent to considering flows at $Ro = 0$.

We systematically compare the turbulent dispersion properties of both types of trajectories using two-particle statistics, primarily through Lagrangian Lyapunov exponents of various types. The results align with the findings in Chapter 4, where we analyzed particle advection in simulations at different Rossby numbers and observed the weak impact of ageostrophic velocity on relative dispersion. However, they also reveal that advection by geostrophic-only flow tends to overestimate the typical pair-separation rate.

Moreover, we show that filtering the ageostrophic flow causes a bias on trajectories, whose importance increases with Ro , and we quantify the scale-by-scale dispersion rate between the full and geostrophic-only advection models. We further provide a characterization of the temporary particle clusters that form due to ageostrophic motions. In particular, we find that, while compressibility is always small in our simulations, due to the smallness of the Rossby numbers explored, the intensity of clustering can be substantial. Our analysis indicates that, in the SQG⁺¹ system, clustering is essentially due to the interplay between the (small) flow compressibility and the existence of long-lived structures that trap particles, increasing their accumulation.

This chapter is structured as follows. In Sec. 5.1, we characterize the main turbulent features of the full flow and its filtered geostrophic counterpart. Next, we assess Lagrangian statistics for tracers advected by either the complete velocity field or its geostrophic component. In Sec. 5.2, we discuss the impact of filtering on the relative-dispersion process, and in Sec. 5.3, we examine the small-scale particle dynamics using Lyapunov exponents, with a particular focus on clustering in the full flow. Finally, discussions and conclusions are presented in Sec. 5.4.

5.1 Eulerian properties of the turbulent flow and its geostrophic component

In this section, we present the main characteristics of the turbulent flows for SQG^{+1} and $(\text{SQG}^{+1})_g$. This is a first attempt at distinguishing between the full flow and its geostrophic component.

For nonzero Rossby number, the SQG^{+1} flow is characterized by well-defined, mainly cyclonic, eddies of different sizes and sharp gradients along filament-like structures. This is illustrated in Fig. 5.2a, which shows the (full) vorticity field $\zeta_f = \partial_x v - \partial_y u$, normalized by its root-mean-square (rms) value ζ_f^{rms} , for $Ro = 0.0625$ at an instant of time t_* in the statistically steady state reached by the system after a transient. The rms vorticity is found to be close to $\zeta_f^{\text{rms}} \approx 10$, and to slightly grow with Ro but overall to weakly depend on it. It provides an *a posteriori* measure of the Rossby number as $Ro \zeta_f^{\text{rms}} \lesssim 1$ (see Fig. 5.1), suggesting that the small scales of our flows can be interpreted as submesoscales. The

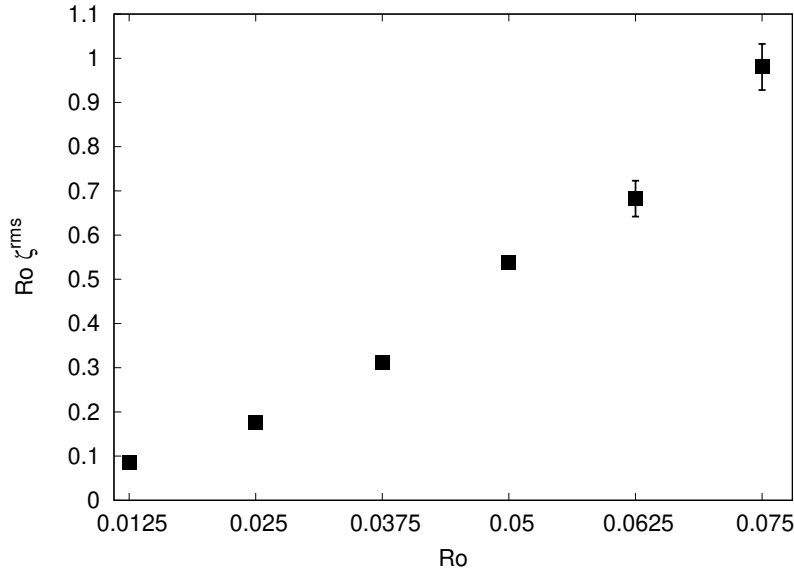


Figure 5.1: Rossby number estimated by $Ro \zeta_f^{\text{rms}}$ as a function of Ro for the full SQG^{+1} simulations.

presence of strong gradients in the horizontal flow (as visualized by ζ_f) is a generic feature due to the ageostrophic velocity components [67]. This can be

deduced from Fig. 5.2b where we show the difference field $\Delta\zeta = \zeta_f - \zeta_g$ (i.e. the ageostrophic vorticity), again normalized by ζ_f^{rms} . Positive values of $\Delta\zeta$ can be seen at the periphery of cyclonic eddies and along extended filaments. This implies that the full cyclonic vorticity, ζ_f , is stronger than its geostrophic component, ζ_g .

Filtering also has consequences on Lagrangian dynamics (see Fig. 5.2c and Fig. 5.2d). For instance, when initially uniformly distributed tracer particles are advected by either the full or the geostrophic-only flow, important qualitative differences emerge, such as the occurrence of clustering when ageostrophic fluid motions are included (Fig. 5.2c). For the geostrophic flow, instead, no sign of clustering is observed (Fig. 5.2d), as expected due to the nondivergent character of this flow. We will discuss particle dispersion properties and clustering in Sec. 5.2 and Sec. 5.3.

We now examine the statistical features of the Eulerian flows from a more quantitative point of view. Figure 5.3 shows the kinetic energy spectrum $E(k)$, with k the horizontal wavenumber modulus, for three cases: the purely SQG ($Ro = 0$) flow, the full SQG⁺ flow at $Ro = 0.0625$ and its geostrophic component [i.e. filtering \mathbf{u}_{ag} in Eq. (2.39)]. In all cases, we find that spectra follow power laws $E(k) \sim k^{-\beta}$ over about a decade. In an oceanographic context, this means that our simulations resolve both the mesoscale range [$O(100)$ km], here corresponding to spatial scales $\ell \approx 1/k_f$, and the submesoscale range down to length scales of $O(10)$ km, here corresponding to $\ell \approx 1/(10k_f)$. For both the $Ro = 0$ and full $Ro = 0.0625$ cases, the exponent β is larger than $5/3$, the value expected for SQG turbulence forced at large scales [25]. This fact is found to be general and independent of the Rossby number, with spectral exponents in the range $2.2 \lesssim \beta \lesssim 2.7$ (see Fig. C.3). Its causes are the presence of large persistent structures (of size comparable with the forcing lengthscale), which are known to steepen the spectrum [47, 67, 68], but also the important values of the small-scale dissipation coefficients used [52]. The spectrum of the filtered flow at $Ro = 0.0625$ is found to be lower than that of the corresponding full flow (at all scales), and the same is true for all the Rossby numbers considered (see Fig. C.3). It is worth remarking, however, the clearly higher similarity with the spectrum of the full flow (at the same Rossby number) than with that of the $Ro = 0$ flow.

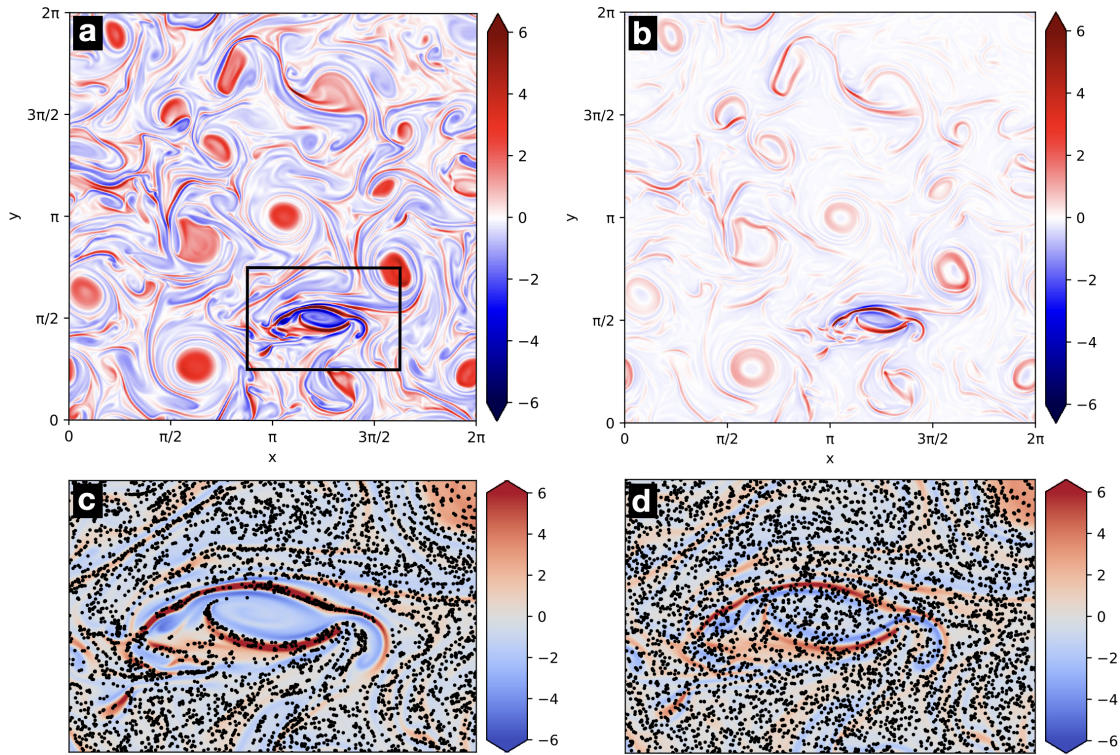


Figure 5.2: (a) Vorticity field ζ_f for the SQG⁺ system for $Ro = 0.0625$ at a specific time t_* during the statistically stationary state. (b) Difference field $\Delta\zeta = \zeta_f - \zeta_g$, where ζ_g is the geostrophic component of vorticity. Panels (c) and (d) show the distribution of particles at time t_* in the region corresponding to the black rectangle in (a), for advection realized by either the full flow (c), or its geostrophic component (d). In (c) and (d), the full and geostrophic vorticity fields are shown in color, respectively. In all panels, vorticity is normalized by the rms value of ζ_f .

This provides a first evidence of the fact that, even after filtering, traces of the influence of the ageostrophic velocities are still discernible in the geostrophic flow component. In other words, the properties of a genuine, dynamically constrained geostrophic flow are not fully recovered once ageostrophic motions are (*a posteriori*) removed from the complete flow.

The relative difference between the kinetic energy of the filtered and full flow $|E_g - E_f|/E_f$ grows with increasing Ro and can reach about 40% at the highest Rossby number (inset of Fig. 5.3). Note that these values do not appreciably change when the contributions from the smallest wavenumbers are excluded from the computation of E_f and E_g . This difference is clearly due to the ageostrophic kinetic energy $E_{ag} = Ro^2 \langle |\mathbf{u}_{ag}|^2 / 2 \rangle_x$ (with $\langle \dots \rangle_x$ a spatial average),

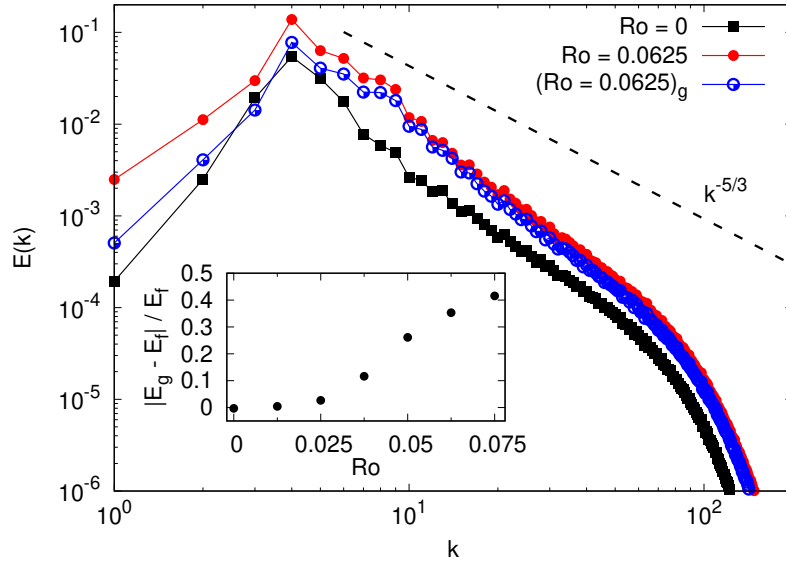


Figure 5.3: Kinetic energy spectra, temporally averaged over several flow realizations in the statistically steady state for $Ro = 0$, $Ro = 0.0625$ and $(Ro = 0.0625)_g$ (i.e., for the geostrophic component of the simulation at $Ro = 0.0625$). The dashed black line corresponds to $k^{-5/3}$, the expected spectrum for SQG turbulence. Inset: absolute value of the relative difference of kinetic energy between the full and filtered flow as a function of Ro .

but also to the positive correlation between the geostrophic and ageostrophic components of the flow. Indeed, the total velocity is $\mathbf{u}_f = \mathbf{u}_g + Ro \mathbf{u}_{ag}$, so that $E_f = E_g + E_{ag} + Ro \langle \mathbf{u}_g \cdot \mathbf{u}_{ag} \rangle_x$. In our simulations, the last term is found to be always positive (Fig. 5.4), meaning that it contributes to the increase of E_f with respect to E_g . As it is proportional to Ro , it is also typically larger than E_{ag} due to the Ro^2 dependence of the latter. Additionally, this result confirms that the filtered, geostrophic flow also depends on the ageostrophic corrections.

A distinctive feature of the SQG⁺¹ model, absent in the QG and SQG systems, is the asymmetry of vorticity statistics, with cyclones prevailing over anticyclones [47, 67]. To further investigate the imprints left by ageostrophic motions on the filtered flow, we consider the probability density function (pdf) of vorticity. Unlike divergence, which vanishes when ageostrophic terms are filtered out, no condition is imposed by the filtering procedure on vorticity. Figure 5.5 shows vorticity skewness (S_ζ) as a function of Ro for the total flow and its geostrophic component. The corresponding pdfs $P(\zeta)$ are reported in the inset of Fig. 5.5

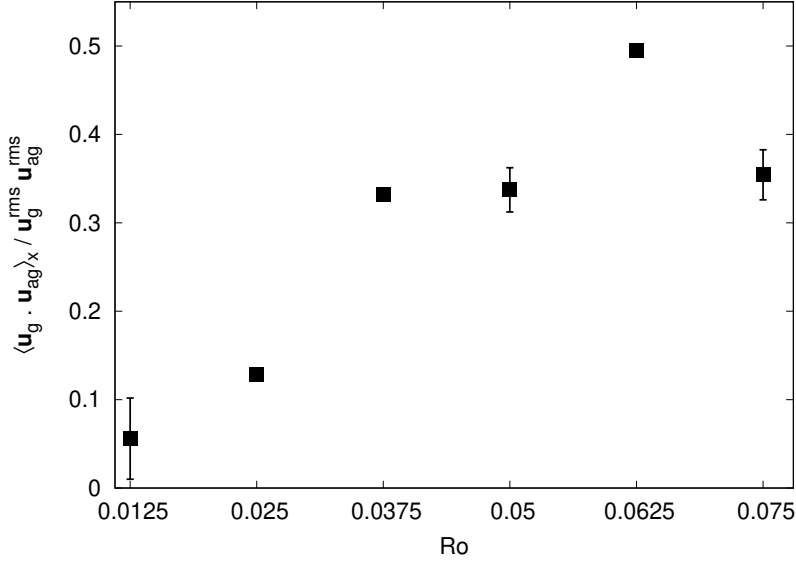


Figure 5.4: Normalized correlation between the geostrophic and ageostrophic flow components as a function of Ro (where $u_g^{rms} = \sqrt{\langle |\mathbf{u}_g|^2 \rangle}$ and similarly for u_{ag}^{rms}). Here, the average is over several flow realizations in statistically steady conditions, and errors bars are computed as the difference between the average over the full dataset and over half the dataset.

(with ζ rescaled by its rms value s_ζ) for $Ro = 0.0625$. Positive skewness, indicative of the predominance of cyclonic structures, characterizes the vorticity pdf of the full SQG⁺¹ flows, and this effect becomes more important with increasing Ro . After filtering, S_ζ significantly drops to values much closer to zero. However, it definitely stays positive at large enough Rossby numbers (see also the inset of Fig. 5.5). This means that the cyclone-anticyclone asymmetry, though strongly reduced, still persists in the filtered velocity field and highlights, once more, that the latter is different from a purely SQG flow at $Ro = 0$.

We conclude this section by noting that the reduction of the vorticity skewness, when taking only the geostrophic flow component, is associated with a decrease of the right tail (and rise of the left one) of $P(\zeta)$. By looking at the vorticity difference field in Fig. 5.2b, it is possible to see that $\Delta\zeta$ is predominantly positive and that a relevant part of the vorticity variation occurs along filamentary structures. In particular, comparison with Fig. 5.2a shows that the intensity of cyclonic ($\zeta > 0$) filaments gets lowered by filtering, in qualitative agreement with the behavior of $P(\zeta)$. Such structures play a central role in

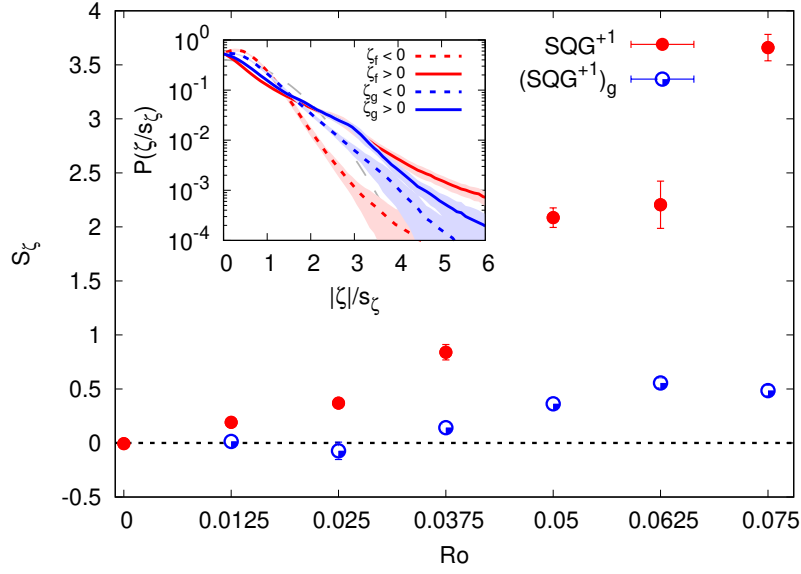


Figure 5.5: Skewness of vorticity ($S_\zeta = \langle \zeta^3 \rangle / \langle \zeta^2 \rangle^{3/2}$) as a function of the Rossby number for SQG⁺ (filled red points) and (SQG⁺)_g (empty blue points), averaged over several flow realizations in statistically steady conditions. The error is computed as the difference between the average over the full dataset and over half the dataset. Inset: Probability density function of vorticity ζ (rescaled by its rms value s_ζ), temporally averaged over several flow realizations in the statistically steady state for $Ro = 0.0625$. Here, the red and blue colors correspond to the SQG⁺ and (SQG⁺)_g cases, respectively. The dashed and solid lines are for $\zeta < 0$ and $\zeta > 0$, respectively. The shaded areas correspond to the standard deviation of the temporal statistics. For comparison, the long-dashed gray line represents a Gaussian distribution.

particle clustering. Indeed, drifter studies [18] and realistic simulations [90, 92] of submesoscale ocean turbulence indicate that flow convergence (and intense vertical velocities) should take place along cyclonic frontal regions. As discussed in Chapter 4, the SQG⁺ system can be seen as a minimal model capable of accounting for this feature and giving rise to particle clustering. When we compare the particle distributions in Fig. 5.2c and Fig. 5.2d, obtained from advection by the full and filtered flow, respectively, it becomes apparent that substantial variations in the vorticity field reflect in very different particle behaviors. For instance, in the region defined by $\pi \lesssim x \lesssim 3\pi/2$ and $y \approx \pi/2$, we see that particles cluster over an intense positive vorticity filament in the full flow, while this effect completely disappears in the vorticity-weakened, filtered flow.

5.2 Lagrangian dispersion

In this section, we compare the particle transport and dispersion properties of the SQG⁺¹ flows and of the corresponding filtered, (SQG⁺¹)_g, ones. Recall that by (SQG⁺¹)_g we mean that only the geostrophic component of the flow is used to advect the Lagrangian tracers. The analysis presented below relies on both time- and scale-dependent metrics.

For a comprehensive discussion on Lagrangian statistics and their theoretical expectations, please refer to Chapter 2, Sec. 2.5 of this manuscript. Here, we will briefly remind the reader of the key aspects of Lagrangian statistics that are particularly relevant to the analysis presented in this chapter. This summary aims to provide the necessary context to better understand the following results and interpretations.

We focus on two-particle statistics, which depend on velocity-field spatial increments and allow us to characterize the tracer pair-separation process. The most natural way to proceed is perhaps to measure $\langle R^2(t) \rangle$ [Eq. (2.52)].

At sufficiently short times, one expects a ballistic behavior of the form $\langle R^2(t) \rangle \simeq R_0^2(1 + Zt^2)$ [52, 56], where $Z = \langle \zeta^2/2 \rangle_x$ is enstrophy. At very long times, instead, particles typically are at distances much larger than the largest eddies, and a diffusive scaling is expected, $\langle R^2(t) \rangle \sim t$, due to particles experiencing essentially uncorrelated velocities [17]. At intermediate times, when pair separations lie in the inertial range of the flow, relative dispersion should grow exponentially or as a power law if the kinetic energy spectrum scales as $k^{-\beta}$ with $\beta > 3$ or $\beta < 3$, respectively. The first case is generally referred to as a nonlocal dispersion regime, and $\langle R^2(t) \rangle \sim \exp(2\lambda_L t)$, with λ_L the maximum Lagrangian Lyapunov exponent. In the second case, dispersion is said to be in a local regime, and $\langle R^2(t) \rangle \sim t^{4/(3-\beta)}$ [17, 52].

Another two-particle, fixed-time indicator that can be used to identify dispersion regimes is the kurtosis of the relative distance between particles in a pair [Eq. (2.56)] [17, 52].

When dispersion is nonlocal (i.e., dominated by the largest flow structures), rapid (exponential) growth of $ku(t)$ is expected. For local dispersion (meaning controlled by flow features of size comparable with the distance between a

pair of particles), the kurtosis should be constant; in particular, $ku(t) = 5.6$ for Richardson dispersion (the behavior expected for $\beta = 5/3$). At larger times, in the diffusive regime, the kurtosis reaches a constant value equal to 2.

We find that two-particle statistics are affected to a limited extent by ageostrophic motions (see Fig. 5.6, for $Ro = 0.0625$). Indeed, the curves of $\langle R^2(t) \rangle$ obtained using the full and filtered flows (Fig. 5.6a) are close, and the same holds for all the values of Ro considered (not shown). In both the SQG⁺ and the (SQG⁺)_g cases, at short times, relative dispersion agrees with the t^2 ballistic prediction, the prefactor being close to the enstrophy of the corresponding flow. At later times, $\langle R^2(t) \rangle$ is slightly larger in the full flow, but the two curves reach the diffusive regime with almost identical values; the same trend is observed at all Rossby numbers. However, its importance decreases as Ro decreases, and it is hardly detectable for $Ro < 0.05$. At this level, while the effect is small, one may speculate that this slowing down of $\langle R^2(t) \rangle$ in the full-flow case is due to particle trapping in flow convergence regions. At intermediate times, relative dispersion grows faster than t^3 , which is consistent with the spectra of the two flows being steeper than $k^{-5/3}$, but overall, the data do not allow to draw quantitative conclusions about the agreement with the predictions for different dispersion regimes.

The behavior of the kurtosis (Fig. 5.6b) reveals two points. On one side, for both full and filtered flows, the rapid initial growth (up to values ≈ 350) points to nonlocal dispersion. Indeed, for a local dispersion regime, one would instead obtain a stabilization around a constant, much smaller value. As extensively discussed for SQG⁺ flows at varying Rossby numbers in a previous work [67], this is due to the presence of large-scale coherent flow structures that dominate the particle spreading process. On the other side, we find that, except perhaps at the very shortest times, $ku(t)$ grows more rapidly and to higher values in the geostrophic-only flow. While the difference is small, it is clearly detectable, and it is observed also at other Rossby numbers (not shown). This implies that the dispersion regime is more strongly nonlocal when particles are advected by the geostrophic component of the flow only (a result that is difficult to infer from relative dispersion alone).

As fixed-scale indicators are often preferred to fixed-time ones to identify

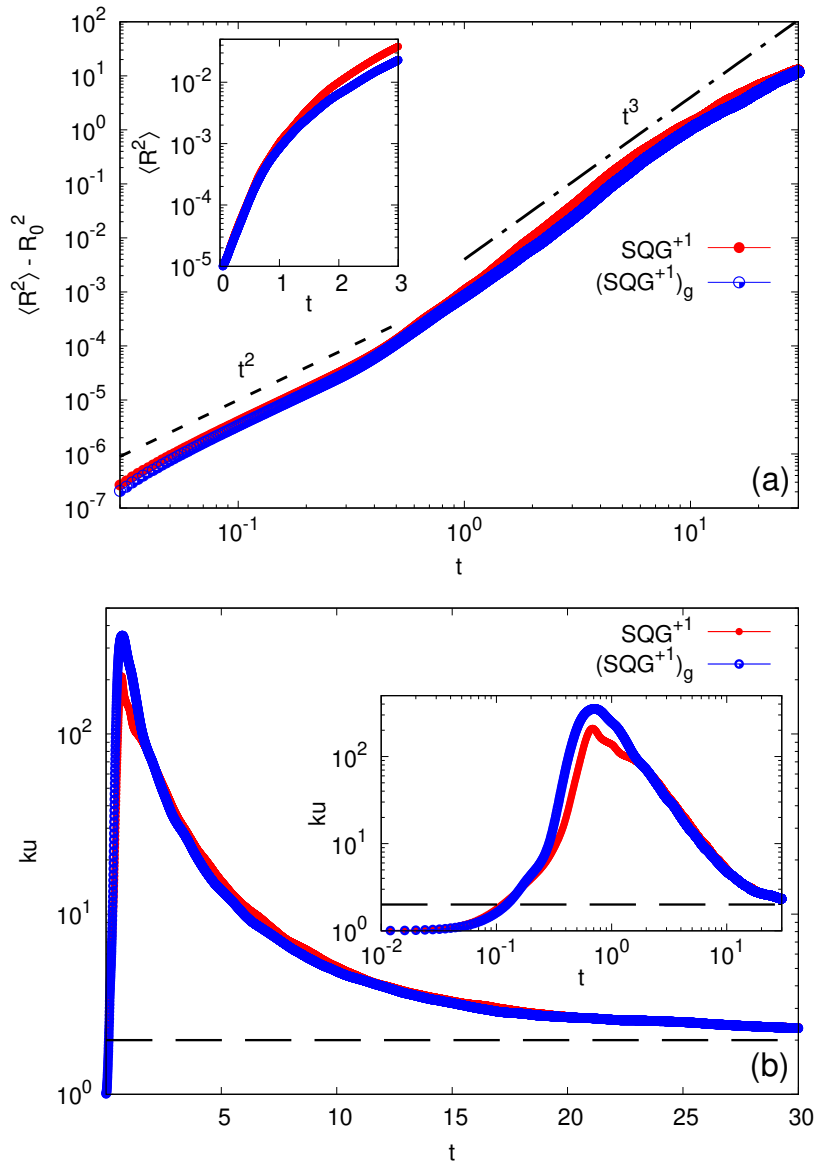


Figure 5.6: (a) Relative dispersion (after subtraction of the initial value) $\langle R^2(t) \rangle - R_0^2$ as a function of time. The t^3 (Richardson dispersion) scaling law is the expectation for a kinetic energy spectrum $E(k) \sim k^{-5/3}$, and the t^2 one is the short-time ballistic expectation. Inset: early growth of relative dispersion $\langle R^2(t) \rangle$ versus time in semilogarithmic scale. (b) Kurtosis of separation as a function of time on a semilogarithmic scale. The horizontal dashed line is the expectation $ku = 2$ in the diffusive regime. The inset shows the same in logarithmic scales. In both (a) and (b) $Ro = 0.0625$, the filled red points correspond to advection by the full SQG⁺¹ flow and the empty blue ones to advection by its geostrophic component only.

dispersion regimes [59], we now examine the FSLE [Eq. (2.57)] [59, 60] where the average is over all pairs and $\tau(\delta)$ is the time needed for the separation to grow from δ to a scale $r\delta$ (with $r > 1$). Dimensionally, it is possible to relate the FSLE to the exponent β of the kinetic energy spectrum. For $\beta > 3$ (i.e., in the nonlocal dispersion regime), the FSLE should be constant, $\lambda(\delta) = \lambda_L$. When dispersion is local ($\beta < 3$), it should have a power-law dependence $\lambda \sim \delta^{(\beta-3)/2}$, while in the diffusive regime one expects $\lambda(\delta) \sim \delta^{-2}$.

Our measurement of $\lambda(\delta)$ is reported in Fig. 5.7 for $Ro = 0.0625$, for both advection by the full and filtered flows. The results confirm those from $ku(t)$: dispersion is essentially nonlocal [$\lambda(\delta) \simeq \text{const}$] over a broad range of separations, and the corresponding plateau value (an estimate of λ_L) is larger for advection by the geostrophic part of the flow only. This result also qualitatively agrees with the expectation that particle convergence, due to ageostrophic motions, reduces the dispersion rate. At the largest separations, the FSLE approaches the diffusive δ^{-2} scaling. Qualitatively similar results are found for the other Rossby numbers considered. From a quantitative point of view, the differences due to filtering are quite small. However, the overestimation of the small-scale dispersion rate [the plateau value $\lambda(\delta) \simeq \text{const}$] is not always negligible. Indeed, in the inset of Fig. 5.7, we see that the relative difference $(\lambda_g - \lambda_f)/\lambda_f$ between those values computed in the full (λ_f) and geostrophic (λ_g) flow advection cases, grows monotonically and can reach about 20% at the highest values of Ro . This finding appears relevant for Lagrangian dispersion applications relying on advection of synthetic drifters using real data from satellite altimetry, as the latter measures the geostrophic flow. Moreover, in real oceanic conditions the Rossby number could be much larger than in the present simulations, and thus this type of effects may be expected to be much more important.

Most often, Eq. (2.57) is used to characterize the growth of the separation between two particles starting from different initial positions and evolving in the same flow. In such a case, $\lambda(\delta)$ is known as the FSLE of the first kind (FSLE-I). Another possibility is to apply the same computation to pairs of particles that start from the same position but evolve in two different flows, such as a reference flow and a perturbed one. This gives the FSLE of the second kind (FSLE-II), $\tilde{\lambda}(\delta)$, which is sometimes used to quantify the effect of unresolved flow

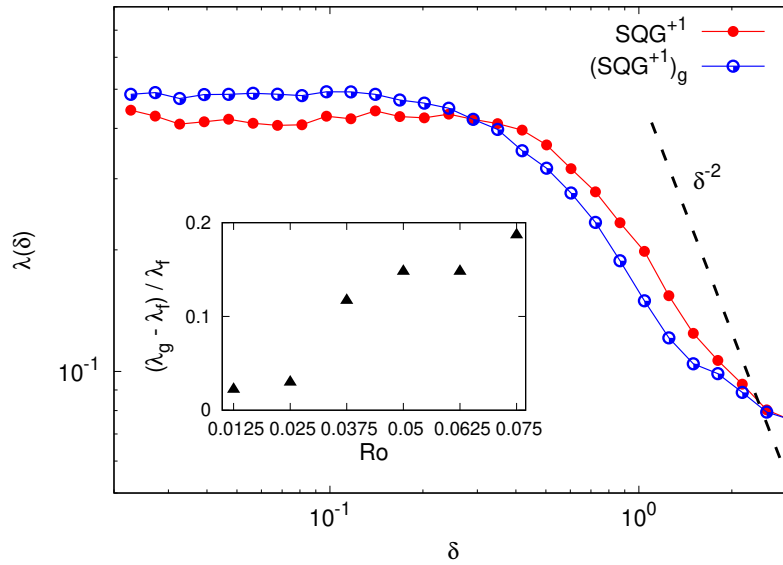


Figure 5.7: FSLE of the first kind $\lambda(\delta)$ for $Ro = 0.0625$; the filled red points correspond to advection by the full SQG⁺¹ flow and the empty blue ones to advection by its geostrophic component only (i.e., by the filtered flow). The δ^{-2} scaling law is the dimensional expectation in the diffusive regime. Inset: the relative difference between the plateau value (at small separations) of $\lambda(\delta)$ for particles advected by either the full flow or the filtered one, as a function of Ro .

components [100, 101]. Initially, particles start from the same position. Hence, the early growth of their distance is solely controlled by the differences in the velocity fields they are advected with. When their distance has sufficiently grown, the spatial increment of the velocity field will also contribute to their separation and eventually dominate. This means that at large enough separations, $\tilde{\lambda}(\delta)$ should approach $\lambda(\delta)$, while at small enough ones, the two kinds of FSLE should differ. This yields an estimate of a critical separation scale above which the flow perturbation has no significant effect on particle dynamics.

Based on the above reasoning, we computed the FSLE of the second kind to provide a statistical characterization of the scale-dependent dispersion between the full-flow model and the geostrophic-flow-only model. The results are shown in Fig. 5.8, for all the Rossby numbers explored. The filled black points are the average of the $\lambda(\delta)$ values obtained for different Ro (which only weakly vary when such a control parameter is changed, see Fig. 4.8). As it can be seen, at large enough separations $\tilde{\lambda}(\delta)$ recovers the behavior of $\lambda(\delta)$, while at small ones it deviates from it to approach a δ^{-1} scaling. In this range of δ values, the role of

the ageostrophic flow components, when present, is non-negligible.

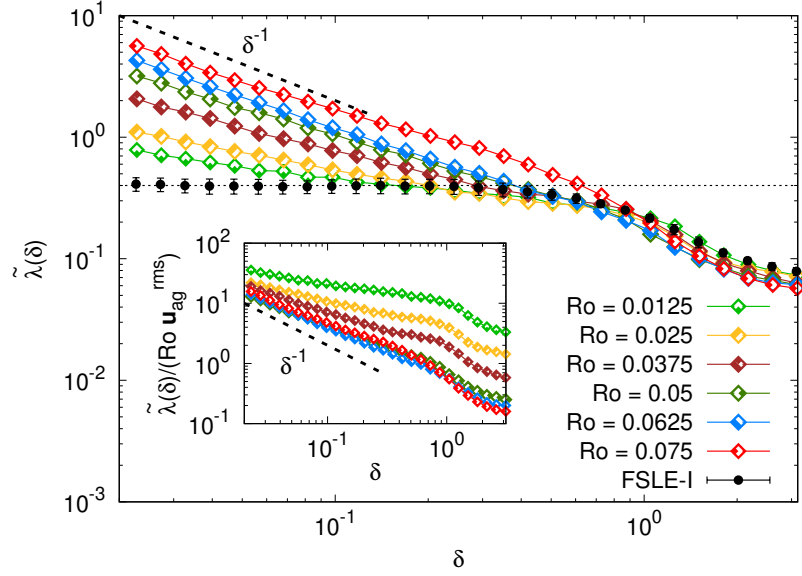


Figure 5.8: FSLE of the second kind $\tilde{\lambda}(\delta)$ for different Rossby numbers. The filled black points correspond to the FSLE-I $\lambda(\delta)$, averaged over the values obtained at the different Rossby numbers. The uncertainty is here quantified by the standard deviation computed using the latter values. Inset: FSLE-II rescaled by the Rossby number and the rms value of the ageostrophic velocity.

The behavior of the FSLE-II illustrated above can be explained as follows. First, recall that particle dynamics in the full and geostrophic-only flow are governed by $\dot{\mathbf{x}} = \mathbf{u}(\mathbf{x}(t), t) = \mathbf{u}_g(\mathbf{x}(t), t) + Ro \mathbf{u}_{ag}(\mathbf{x}(t), t)$ and $\dot{\mathbf{x}}_g = \mathbf{u}_g(\mathbf{x}_g(t), t)$, respectively. Here, $\mathbf{x}(t)$ is the position of one of the two particles in a pair, advected by the total velocity, and $\mathbf{x}_g(t)$ is that of the other particle in the pair, advected only by the geostrophic velocity. The particle separation vector $\Delta \mathbf{x} = \mathbf{x} - \mathbf{x}_g$ then evolves according to

$$\frac{d\Delta \mathbf{x}(t)}{dt} = \mathbf{u}(\mathbf{x}, t) - \mathbf{u}_g(\mathbf{x}_g, t). \quad (5.1)$$

Adapting a more general derivation [100] to our case, we perform a Taylor

expansion of $\mathbf{u}(\mathbf{x}, t)$ around \mathbf{x}_g :

$$\begin{aligned} \mathbf{u}(\mathbf{x}, t) &\simeq \mathbf{u}_g(\mathbf{x}_g, t) + \left(\frac{\partial \mathbf{u}_g}{\partial \mathbf{x}} \right)_{\mathbf{x}_g} \Delta \mathbf{x} \\ &+ Ro \left[\mathbf{u}_{ag}(\mathbf{x}_g, t) + \left(\frac{\partial \mathbf{u}_{ag}}{\partial \mathbf{x}} \right)_{\mathbf{x}_g} \Delta \mathbf{x} \right], \end{aligned} \quad (5.2)$$

which implies

$$\begin{aligned} \frac{d\Delta \mathbf{x}(t)}{dt} &\simeq \left(\frac{\partial \mathbf{u}_g}{\partial \mathbf{x}} \right)_{\mathbf{x}_g} \Delta \mathbf{x} \\ &+ Ro \left[\mathbf{u}_{ag}(\mathbf{x}_g, t) + \left(\frac{\partial \mathbf{u}_{ag}}{\partial \mathbf{x}} \right)_{\mathbf{x}_g} \Delta \mathbf{x} \right]. \end{aligned} \quad (5.3)$$

Since particles start from the same position [i.e. $\Delta \mathbf{x}(t_0) = 0$], at short times Eq. (5.3) gives

$$\frac{d\Delta \mathbf{x}(t)}{dt} \simeq Ro \mathbf{u}_{ag}(\mathbf{x}_g, t). \quad (5.4)$$

From Eq. (5.4), using dimensional considerations, one has $\delta/t \sim Ro u_{ag}^{\text{rms}}$ (with $u_{ag}^{\text{rms}} = \sqrt{\langle |\mathbf{u}_{ag}|^2 \rangle}$). Therefore, the FSLE-II is expected to scale as

$$\tilde{\lambda}(\delta) \sim \frac{Ro u_{ag}^{\text{rms}}}{\delta}. \quad (5.5)$$

As shown in the inset of Fig. 5.8, the different curves are in fairly good agreement with the prediction in Eq. (5.5), except at the smallest nonzero Rossby number, and collapse onto each other for $Ro \geq 0.05$. At larger times, the separation distance $\Delta \mathbf{x}$ is no longer negligible, and eventually, the terms in $\Delta \mathbf{x}$ on the right-hand side of Eq. (5.3) dominate. For such large relative displacements, the particle separation distance evolves as if both particles were in the same flow, $d\Delta \mathbf{x}/dt \simeq (\partial_x \mathbf{u})_{\mathbf{x}_g} \Delta \mathbf{x}$. As a consequence, for large values of δ one finds $\tilde{\lambda}(\delta) \simeq \lambda(\delta)$, as observed in Fig. 5.8.

The critical relative displacement δ^* below which the FSLE-II differs from the FSLE-I is found to increase with Ro . At the largest value of the latter ($Ro = 0.075$), we have $\tilde{\lambda}(\delta) \neq \lambda(\delta)$ over all separations, except in the diffusive range. If we exclude the data for $Ro = 0.0125$, we observe that when Ro increases from 0.025 to 0.075, i.e. by a factor 3, δ^* increases from approximately 0.15 to 0.8, i.e. by a factor of roughly 5. Despite the idealized character of the present model dynamics, such values suggest caution when performing synthetic-particle advection in the submesoscale range with velocity fields derived from satellite altimetry. Indeed, the bias on the simulated trajectories, in terms of distance from the true ones, may be considerable given the typically larger Rossby numbers of real ocean submesoscales with respect to those assumed here.

5.3 Small-scale particle dynamics and clustering

In the previous section, we analyzed the separation process of Lagrangian tracers. However, through the metrics previously used, it is not possible to address the quantitative characterization of aggregation phenomena. For instance, the FSLE of the first kind (Fig. 5.7) provides an estimate of the (scale-dependent) pair separation rate, but it does not allow the exploration of particle convergence events. Now, we investigate the small-scale particle dynamics for varying Rossby number, focusing on this aspect. This will also allow us to characterize particle clustering.

An interesting tool to address this problem is offered by the spectrum of (asymptotic) Lyapunov exponents $\lambda_{1,2}$, with $\lambda_1 \geq \lambda_2$, which can be computed by linearizing Eq. (2.47) in tangent space and are thus related to the velocity gradient tensor (see Appendix A and [58, 102]). While λ_1 measures the exponential divergence rate (and is positive for a chaotic system), λ_2 accounts for the dynamics along the local contracting direction. As the sum of Lyapunov exponents gives the divergence of the flow, $\lambda_1 + \lambda_2 = \nabla \cdot \mathbf{u}$, clearly for an incompressible flow it is enough to compute λ_1 . However, this is no longer the case in the presence of nonzero compressibility, as in our SQG⁺¹ simulations. In such a case, it is instructive to separate the Lyapunov exponents into their contributions from nondivergent (or straining) and divergent processes. To this end, we

introduce $s = \lambda_1 - \lambda_2$ and $d = \lambda_1 + \lambda_2$, so that $\lambda_1 = (s + d)/2$ and $\lambda_2 = (-s + d)/2$. Since we know that the SQG⁺¹ flow is turbulent, with particle pair separations eventually increasing in time, λ_1 should be positive. Due to the occurrence of clustering at small scales, we also expect $d \leq 0$, implying that $|\lambda_2| \geq \lambda_1$ and $s > 0$. Then, from the expressions of λ_1 and λ_2 it is possible to see that both Lyapunov exponents should be reduced by the nonzero divergence, with respect to those of the incompressible part of the flow.

The Lyapunov exponents computed using the full and filtered flows are shown in Fig. 5.9a as a function of the Rossby number (see Appendix A and [58, 102, 103] for more details on the computation method). Here, we also present the values obtained in the simulation of SQG turbulence (i.e., for $Ro = 0$). The values of $d = \lambda_1 + \lambda_2$ and $s = \lambda_1 - \lambda_2$ versus Ro are shown in Fig. 5.9b [in both panels (a) and (b) an average over all the different Lagrangian initial conditions is also taken]. As expected, for $Ro = 0$, the two Lyapunov exponents sum to zero, $\lambda_2(0) = -\lambda_1(0)$ [$d(0) = 0$]. For nonzero and increasing Ro , both $\lambda_{1,f}$ and $\lambda_{2,f}$ grow in absolute value, but $\lambda_{2,f}$ by a larger amount, so that $|\lambda_{2,f}| > \lambda_{1,f}$ at all Ro (here the subscript f indicates that the full flow is considered). The mean Lagrangian divergence d (the average being over particles) is consistently negative, growing in absolute value with Ro (Fig. 5.9b). In the (SQG⁺¹)_g case, the flow is nondivergent by construction, because only the geostrophic velocity component is retained. As it can be seen in Fig. 5.9b, this constraint is very well satisfied in our simulations. The mean Lagrangian strain s does not differ much between the (SQG⁺¹) and (SQG⁺¹)_g cases, i.e., $s_f \simeq s_g$ (the subscript g indicating that the geostrophic-only flow is considered) for all Rossby numbers. This implies that filtering only affects the divergent part of velocity gradients and much less the straining one. Since $s_f(Ro) \approx s_g(Ro)$ and $d_f(Ro) \leq 0$, we have $\lambda_{1,g}(Ro) = s_g(Ro)/2 \approx s_f(Ro)/2 \geq [s_f(Ro) + d_f(Ro)]/2 = \lambda_{1,f}(Ro)$ and $\lambda_{2,g}(Ro) = -s_g(Ro)/2 \approx -s_f(Ro)/2 \geq [-s_f(Ro) + d_f(Ro)]/2 = \lambda_{2,f}(Ro)$. This explains why $\lambda_{i,g}(Ro) \geq \lambda_{i,f}(Ro)$ (with $i = 1, 2$), as observed in Fig. 5.9a. These arguments then provide support to the increase of the FSLE-I plateau value after filtering (Fig. 5.7). Note that the values of $[\lambda_{1,g}(Ro) - \lambda_{1,f}(Ro)]/\lambda_{1,f}(Ro)$ nicely match those of the FSLE-I relative difference (at not too large separations) shown in the inset of Fig. 5.7. In addition, these results indicate, once more, that filtering

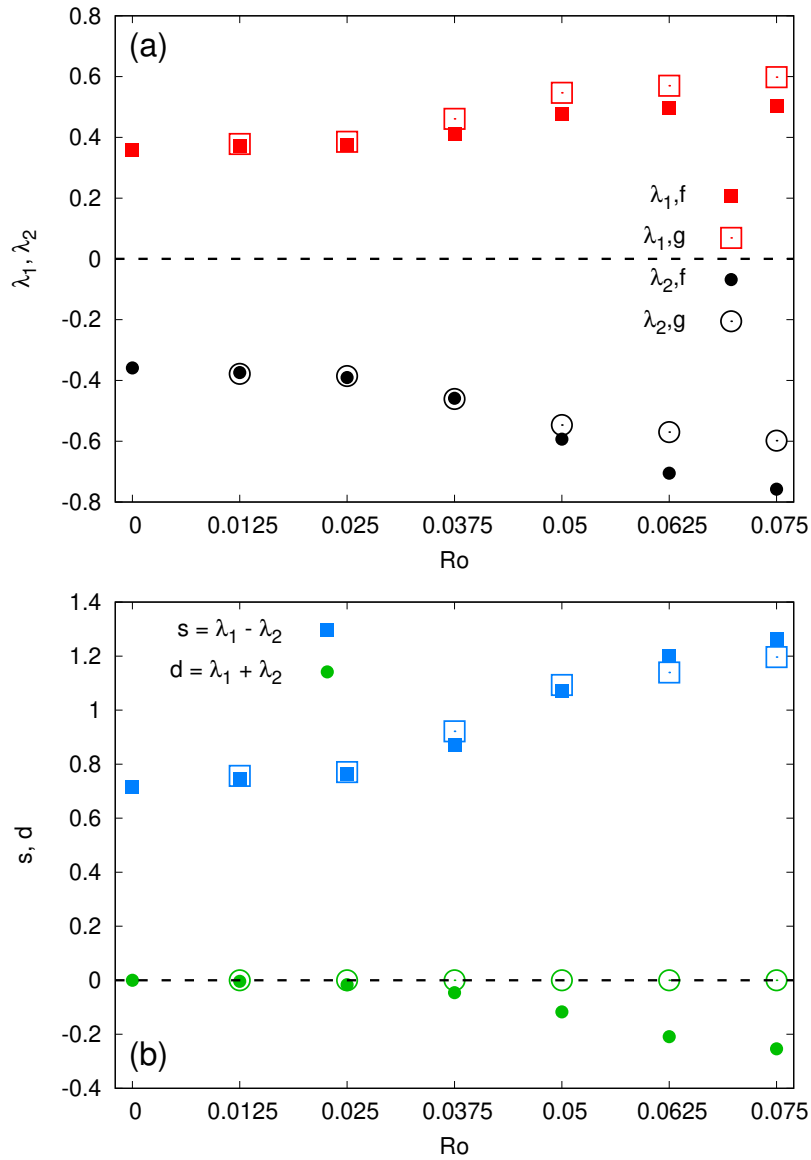


Figure 5.9: (a) Lyapunov exponents of the Lagrangian dynamics (red squares for λ_1 and black circles for λ_2) for varying Rossby number. (b) Mean Lagrangian strain, $s = \lambda_1 - \lambda_2$, and divergence, $d = \lambda_1 + \lambda_2$ versus Ro . In both (a) and (b) the filled and empty points are calculated from SQG⁺ flows and their filtered counterpart (SQG⁺)_g, respectively. Uncertainties, estimated as the standard deviation of $\lambda_{1,2}$ over their time series (at large times), are mostly of the order of point size.

the SQG⁺ flow to exclude ageostrophic motions does not lead to the same flow properties of the SQG system (i.e., with $Ro = 0$).

Lyapunov exponents also provide further information on the clustering of

Lagrangian tracers. In particular, they can be used to compute the fractal dimension of the sets over which particles accumulate (when the full flow is considered). This is known as the Lyapunov dimension D_L [58]. While the correlation dimension D_2 , another estimate of the fractal dimension discussed in Sec. 4.2.2, is derived from the particle distribution and relies solely on particle positions, the Lyapunov dimension provides more insight into the system dynamics and is calculated from the Lyapunov exponents, which requires knowledge of the system's equations. In the present 2D case, it is given by

$$D_L = 1 + \frac{\lambda_1}{|\lambda_2|}. \quad (5.6)$$

Note that for an incompressible flow (like the geostrophic one) one would have $\lambda_1 = |\lambda_2|$, and hence $D_L = 2$, meaning uniformly distributed particles. As in SQG⁺¹ the geostrophic equilibrium is broken and the flow becomes compressible, $|\lambda_2| > \lambda_1$ and $D_L < 2$, implying particle clustering. From Eq. (5.6), when $|\lambda_2| \gg \lambda_1$ one has $D_L \simeq 1$, i.e. a one-dimensional (1D) fractal set. Clustering is clearly due to the compressibility of the horizontal flow being nonzero, and in the following we will thus discuss the relation between D_L and this quantity. However, the flow compressibility alone typically does not allow for full characterization of the distribution of particles [78, 104]. Different other factors can be also important and, among these, the flow time correlations play a relevant role [77, 78], as we shall see below for our system.

The compressibility of the (full) Eulerian flow is quantified by the ratio [77, 78, 104]

$$\mathcal{C} = \frac{\langle (\partial_x u + \partial_y v)^2 \rangle}{\langle (\partial_x u)^2 + (\partial_x v)^2 + (\partial_y u)^2 + (\partial_y v)^2 \rangle}, \quad (5.7)$$

which takes values between 0 and 1, for incompressible and potential flow, respectively. Providing a theoretical prediction for \mathcal{C} from its definition is generally not an easy task as it requires estimating the correlations of velocity gradients. Indeed, the denominator in Eq. (5.7) can be rewritten as $\langle \Delta^2 \rangle + \langle \zeta^2 \rangle - 2\langle (\partial_x u)\partial_y v - (\partial_x v)\partial_y u \rangle$, where the correlations between different velocity-gradient components are more evident, Δ is divergence and ζ is vorticity. However, the structure of the velocity-gradient tensor and its low-order moments

were recently analyzed for both incompressible [105] and compressible [106] three-dimensional (3D) turbulence. Using the same derivation as in [106] and under the assumptions of homogeneity and isotropy, we obtain in the 2D case $\langle(\partial_x u)\partial_y v\rangle = \langle(\partial_x v)\partial_y u\rangle$. This relation is found to be well verified in our simulations for all Rossby numbers (see Appendix B). Compressibility is then given by

$$\mathcal{C} = \frac{\langle\Delta^2\rangle}{\langle\Delta^2\rangle + \langle\zeta^2\rangle}. \quad (5.8)$$

Considering now that $\mathbf{u} = \mathbf{u}_g + Ro \mathbf{u}_{ag}$, one has $\Delta = \nabla \cdot \mathbf{u} = Ro \nabla \cdot \mathbf{u}_{ag}$ and $\zeta = \zeta_g + Ro \zeta_{ag}$. Inserting these expressions in Eq. (5.8), at lowest order we then obtain the following estimate of \mathcal{C} as a function of Ro

$$\mathcal{C} = \frac{Ro^2}{Ro^2 + 1} \sim Ro^2. \quad (5.9)$$

As seen in the inset of Fig. 5.10, our numerical data are in quite good agreement with Eq. (5.9), supporting this prediction.

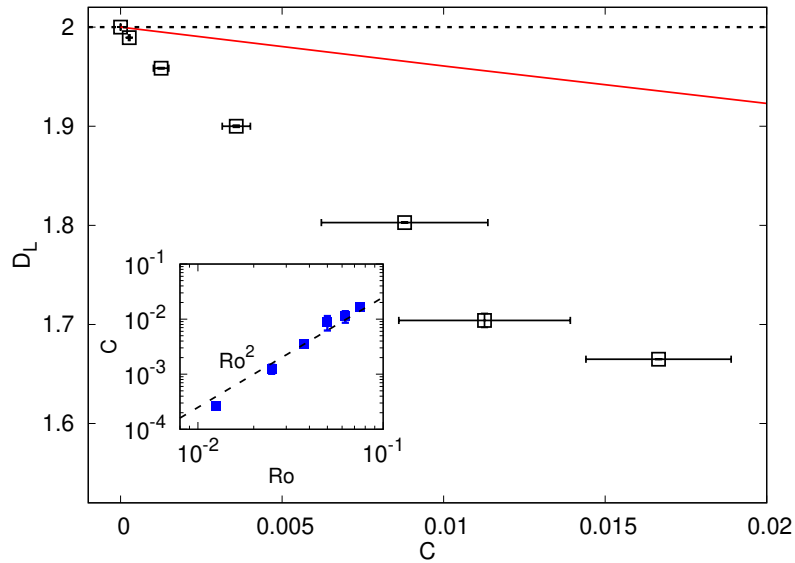


Figure 5.10: Lyapunov dimension D_L , for particles advected by the full flow, as a function of compressibility \mathcal{C} ; the solid red line is the expectation $D_L = 2/(1 + 2\mathcal{C})$ in the compressible Kraichnan model. Inset: compressibility versus Ro and the prediction $\mathcal{C} \sim Ro^2$ (dashed line). Uncertainties on D_L and \mathcal{C} are estimated from the standard deviation using the values taken over their time series (at large times).

While here compressibility is always small, due to Eq. (5.9), clustering is well evident in our flows, as highlighted by the decrease of D_L with \mathcal{C} (Fig. 5.10). For the SQG case ($Ro = 0$ and $\mathcal{C} = 0$), the Lyapunov dimension is very close to 2, in agreement with the nondivergent nature of this flow. As Ro (and then also \mathcal{C}) grows, it decreases monotonically, and its value allows us to quantify the intensity of clustering. Such decrease is due to $|\lambda_{2,f}|$ growing faster with Ro than $\lambda_{1,f}$ (Fig. 5.9a), meaning to the intensification, and dominance, of the locally contracting flow direction. These findings indicate that the structures over which particles accumulate are not space-filling, and tend to be more and more unidimensional for larger Ro . This, in turn, suggests that clustering should occur along filaments, which is in line with the observations from Fig. 5.2c and the discussions in Sec. 4.2.2. By filtering the flow to take only its geostrophic component, instead, we retrieve $D_L = 2$ with good accuracy (as shown in Fig. 5.11), corresponding to particles filling the entire domain (see also Fig. 5.2d). Figure 5.11 presents the behavior of two estimates of the fractal dimension, D_L and D_2 , as a function of the Rossby number (for details on the calculation of D_2 , refer to Sec. 4.2.2). For the SQG case, D_2 and D_L are equal to 2 (within statistical accuracy). As Ro increases, both D_L and D_2 decrease monotonically, and their values allow for quantification of the intensity of clustering. By filtering the flow and only considering its geostrophic component, we retrieve $D_L = 2$ and $D_2 \approx 2$, as mentioned previously. We also observe $D_L \gtrsim D_2$, in agreement with other studies and general arguments about the convexity of the spectrum D_q of generalized dimensions (of order q) [58], which is reasonable considering that $D_L = D_1$ (also known as information dimension).

On the basis of the persistent structures present in our flows (see Sections 5.1 and 5.2), we argue that the relevant decrease of D_L , in spite of the small compressibility, is due to the time correlations in the velocity field. To test this hypothesis, we compare our results with what one would obtain in a temporally uncorrelated flow. For this purpose, we consider the 2D compressible Kraichnan flow, which is white-in-time, and for which the following prediction [77, 78] for D_L is available:

$$D_L = \frac{2}{1 + 2\mathcal{C}}. \quad (5.10)$$

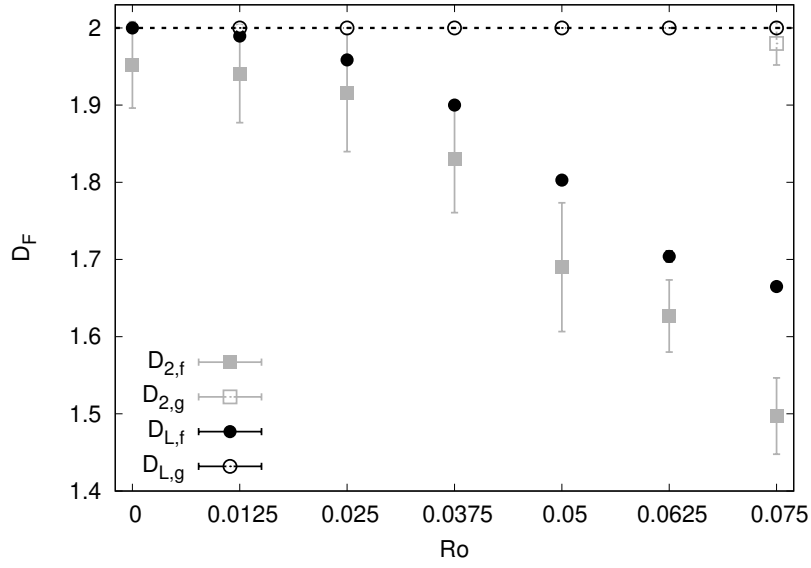


Figure 5.11: Fractal dimension D_F as a function of Rossby number; D_2 and D_L are the correlation dimension and Lyapunov dimension, respectively. The error bars for D_L are of the order of points size and are obtained from the standard deviation of the temporal statistics, while for D_2 , they are obtained from the standard deviation of best fits over the range of small distances r where $C(r) \sim r^{D_2}$. The filled and empty points are for SQG⁺ and (SQG⁺)_g, respectively.

Figure 5.10, where the Kraichnan-model prediction is the solid red line, shows that in the absence of flow temporal correlations, the fractal dimension is considerably larger than in the SQG⁺ system. This indicates that in the present case, clustering is essentially due to the interplay between the (small) Eulerian compressibility and the existence of long-lived flow structures that trap particles, enhancing their aggregation. We note that this finding may also be understood by considering the evolution equation for the gradients of the particle density field $\rho_p(\mathbf{x}, t)$. The latter is defined as the number of Lagrangian tracers per area and is governed by the equation $\partial_t \rho_p + \mathbf{u} \cdot \nabla \rho_p = -\rho_p \nabla \cdot \mathbf{u}$. For the gradients of ρ_p one then has:

$$\frac{D}{Dt} \nabla \rho_p = -(\nabla \mathbf{u})^T \nabla \rho_p - \Delta \nabla \rho_p - \rho_p \nabla \Delta, \quad (5.11)$$

in which $D/Dt = \partial_t + \mathbf{u} \cdot \nabla$, $(\nabla \mathbf{u})^T$ denotes the transpose of the velocity gradient tensor and Δ is divergence. From Eq. (5.11), one can see that Δ , which is due to ageostrophic corrections, if nonuniform ($\nabla \Delta \neq 0$), will create gradients of the scalar field ρ_p that will be amplified in convergence regions ($\Delta < 0$), and further

strengthened by persistent strain [related to the velocity-gradient tensor $(\nabla \mathbf{u})$]. Taking the dot product of Eq. (5.11) with $\nabla \mathbf{u}$ and decomposing the velocity-gradient tensor into its symmetric and antisymmetric parts, $\nabla \mathbf{u} = \mathbf{S} + \mathbf{A}$, where $\mathbf{S} = [\nabla \mathbf{u} + (\nabla \mathbf{u})^T]/2$ and $\mathbf{A} = [\nabla \mathbf{u} - (\nabla \mathbf{u})^T]/2$, we obtain:

$$\frac{1}{2} \frac{D}{Dt} |\nabla \rho_p|^2 = -(\nabla \rho_p)^T (\mathbf{S} - \mathbf{A}) \cdot \nabla \rho_p - \Delta |\nabla \rho_p|^2 - \frac{1}{2} \nabla \rho_p^2 \cdot \nabla \Delta. \quad (5.12)$$

Since $\nabla \rho_p \cdot (\mathbf{A} \nabla \rho_p) = 0$, the equation simplifies to:

$$\frac{1}{2} \frac{D}{Dt} |\nabla \rho_p|^2 = -\nabla \rho_p \cdot (\mathbf{S} \nabla \rho_p) - \Delta |\nabla \rho_p|^2 - \frac{1}{2} \nabla \rho_p^2 \cdot \nabla \Delta. \quad (5.13)$$

Equation (5.13) demonstrates that rotation, represented by \mathbf{A} , does not influence the magnitude of $\nabla \rho_p$; only strain, via \mathbf{S} (the strain rate tensor), and divergence affect it. As strain is related to the structure of the flow, in the SQG⁺¹ case, its persistence reflects the time correlations of the velocity field. In the temporally uncorrelated Kraichnan flow, instead, this effect is not present, which leads to weaker clustering.

We conclude by noting that the transition to strong clustering, with particles accumulating over 1D structures, is marked by the Lyapunov dimension reaching $D_L = 1$. This occurs for a critical compressibility $\mathcal{C}^* = 1/2$ in the Kraichnan model. Based on the results in Fig. 5.10, with the numerical data being always below the theoretical prediction of Eq. (5.10), one may speculate that in the SQG⁺¹ system, the transition occurs for $\mathcal{C}^* < 1/2$. From \mathcal{C}^* , the corresponding critical Rossby number may then be estimated as $Ro^* \approx \mathcal{C}^{*1/2}$. However, clustering properties in time-correlated compressible flows strongly depend on the spatio-temporal details of the velocity field [77]. Indeed, it has been shown that for Lagrangian tracers at the free surface of a 3D incompressible Navier-Stokes turbulent flow [78], while the qualitative behavior of D_L as a function of \mathcal{C} is similar to that observed here for small \mathcal{C} , the transition occurs at $\mathcal{C}^* > 1/2$. The determination of the critical compressibility (and Rossby number) for SQG⁺¹ turbulence thus remains an open question, which would require considerably extending the range of Ro values explored and extensive numerical simulations.

5.4 Conclusions

We investigated surface-ocean turbulence in the fine-scale range by means of numerical simulations of the SQG⁺¹ model [47, 67]. This model is derived from primitive equations and extends the SQG one by including ageostrophic motions corresponding to first-order corrections in the Rossby number. By construction, the latter are related to secondary flows due to finite-Rossby effects at fronts. Note that other ageostrophic processes (, e.g., internal waves), further deviating from geostrophy, are not represented [107]. As previously shown [67] (refer to Chapter 4), this approach allows to reproduce both the prevalence of cyclones over anticyclones and the accumulation of Lagrangian tracers in cyclonic frontal regions, which are found in observations [18, 20–22, 24] but not captured by standard QG models. Our main goal was to assess the effect of ageostrophic motions on Lagrangian pair dispersion, which is relevant for the interpretation and exploitation of new, high-resolution satellite data [16, 108], as well as to improve the understanding of material spreading at the surface of the ocean. For this purpose, we compared Lagrangian statistics for tracer particles advected by either the full SQG⁺¹ flow or by its filtered, geostrophic counterpart for different Rossby numbers.

Our results confirm the general expectation, also supported by previous numerical indications [67], that relative dispersion weakly depends on the ageostrophic corrections to the flow. From a quantitative point of view, however, the FSLE-I, a fixed lengthscale indicator of the separation process, reveals that excluding the ageostrophic velocity leads to an overestimation of the typical pair-dispersion rate and that the importance of this effect grows with Ro . This can be understood by analyzing the spectrum of the (asymptotic) Lyapunov exponents of the particle dynamics. Considering the weak dependence of the FSLE-I on spatial scales in the present simulations, the latter appears appropriate for characterizing the small-scale behavior of particles over a significant range of scales. A decomposition of Lyapunov exponents into the divergent and nondivergent parts of the velocity-gradient tensor experienced by particles shows that the absence of flow convergences in the geostrophic-only case is at the origin of the increase of both exponents and, hence, of the FSLE-I at the

smallest separations.

In addition, we examined the scale-by-scale dispersion rate for pairs such that both particles start from the same position but one evolves in the full flow and the other in the filtered one. We found that such an inter-model dispersion rate (FSLE-II) differs from the FSLE-I over a range of small separations, which extends towards larger and larger ones with Ro . The behavior of the FSLE-II is explained by a simple theoretical argument relying on the different mechanisms (the differences in the evolution equations and in the particle positions) controlling the separation process. These results highlight that at sufficiently small separations particle trajectories are sensitive to ageostrophic motions and can be biased if advected by the geostrophic velocity only, which appears relevant to applications using satellite-derived velocity fields to advect synthetic particles in order to deduce flow transport properties.

Beyond the above quantitative differences, the ageostrophic velocities are responsible for a major qualitative change in the Lagrangian dynamics, namely the occurrence of clustering of tracer particles. While this is clearly not captured by geostrophic flows, which are incompressible by definition, it has important consequences for the identification of hotspots of pollutant accumulation in the sea and for marine ecology modeling. We then measured its intensity for increasing Rossby numbers and characterized the mechanisms controlling it in the SQG^{+1} system. We showed that the horizontal-flow compressibility is always small and grows only quadratically with Ro . Nevertheless, clustering can be relatively intense, with the Lyapunov dimension clearly decreasing to values smaller than 2 with increasing Ro (and compressibility). Finally, the comparison of our numerical results with the prediction for the time uncorrelated Kraichnan flow [78, 104] revealed that clustering is, in the present case, essentially due to the interplay between the small compressibility and the important temporal correlations of the flow.

To conclude, this study indicates that the overall effect of ageostrophic motions related to fronts on Lagrangian pair dispersion at the ocean surface should be weak. Nevertheless, it also suggests some caution in particle advection experiments with geostrophically derived flows, as single-particle trajectories should separate from the true ones, and important phenomena, such as clustering,

would be missed. An interesting further development of this work is to extend the analysis to data from general circulation models at the global scale to address the impact on Lagrangian dynamics of other ageostrophic processes (internal gravity waves and tides) that are associated with the ocean's fast variability (see Chapter 6).

Particle dispersion in a general circulation model

In Chapters 4 and 5, we explored particle dispersion within the idealized SQG⁺¹ model, introduced in Chapter 2, Sec. 2.4. In this chapter, we use data from the MITgcm LLC4320 simulation and Lagrangian tracer advection (provided by Aurélien Ponte, Ifremer) aiming to identify the mechanisms that drive dispersion when high-frequency motions, absent in the SQG⁺¹ model, are included. We aim to examine the role of these high-frequency motions in the particle dispersion process, an aspect that, to our knowledge, remains an unexplored open question. By doing so, we intend to provide a more complete characterization of dispersion by encompassing a broader spectrum of oceanic motions. The findings in this chapter result from a collaboration between Stefano Berti, Guillaume Lapeyre, Aurélien Ponte, and myself.

Our work investigates the dispersion and clustering properties of Lagrangian tracer particles in the Kuroshio Extension during winter and summer. The study area was specifically chosen for its energetic currents with intense submesoscale activity and its proximity to a SWOT crossover. We also chose two distinct seasons to explore the effects of seasonal variability. The findings indicate that in winter, pair dispersion is predominantly influenced by mesoscale and submesoscale motions. Additionally, the slope of the kinetic energy spectrum derived

from SSH via geostrophic balance is underestimated, leading to a potential overestimation of the small-scale pair-separation rate. Conversely, in summer, when high-frequency motions are more pronounced, the results emphasize the necessity of considering the full spectrum of oceanic motions and highlight the importance of selecting appropriate Lagrangian indicators to accurately capture which processes govern pair-dispersion.

This chapter is organized as follows. Sec. 6.1 describes LLC4320 with the implementation of Lagrangian particles. Sec. 6.2 provides an overview of internal gravity waves (IGWs). In Sec. 6.3, we present the Lagrangian transport properties of the flow in a region near the Kuroshio current, then we relate them to the Eulerian properties of the flow through spectral analyses in both the frequency and wavenumber domains, which are discussed in Sec. 6.4. Finally, discussions and conclusions are presented in Sec. 6.5.

6.1 Model description

As mentioned briefly in Chapter 1, Sec. 1.2, LLC4320 is a simulation performed using MITgcm on an LLC Arakawa-C grid. It has a horizontal spatial resolution of $1/48^\circ$, ranging from 0.75 km at the Arctic to 2.2 km at the Equator, with 90 vertical levels of ~ 1 m spacing near the surface which gradually increases with depth. The model uses a time step of 25 seconds and outputs data hourly for a 1-year period spanning from 13 September 2011 to 15 November 2012. Given its spatial and temporal resolutions, LLC4320 can resolve the high-frequency motions in the ocean. Here, we focus on surface dynamics, using only the surface velocities and SSH outputs from the simulation.

In addition to the SST validation [14], the LLC4320 simulation has been validated against in-situ observations to assess its accuracy in reproducing spectral dynamics and kinetic energy across various time and spatial scales. In the Drake Passage, the model data compare well with Acoustic Doppler Current Profiler (ADCP) measurements for the rotational and divergent flow components following a one-dimensional Helmholtz decomposition [109]. Additionally, it accurately captures the location and amplitude of kinetic energy peaks in the

Northwestern Pacific [110]. LLC4320 also effectively reproduces diurnal and semidiurnal tidal variances, and its higher spatial resolution allows better modeling of internal gravity waves, surpassing other models in supertidal frequency accuracy [111].

The LLC4320 surface velocities are utilized to advect Lagrangian tracer particles using Parcels, a customizable Lagrangian simulator in Python developed by OceanParcels. The particles are initially uniformly distributed across the domain in triplets, each arranged in an equilateral triangle inscribed within a circle of radius 1 km (Fig. 6.1). A total of 1 976 343 particle triplets, equivalent to 5 929 029 particles, are seeded in the LLC4320 flow field and advected over a 30-day period during both February and August of 2012. Data from this simulation is outputted hourly. Since the Kuroshio Extension is in the Northern Hemisphere, February and August represent winter and summer, respectively, allowing us to explore the effects of seasonal variability.

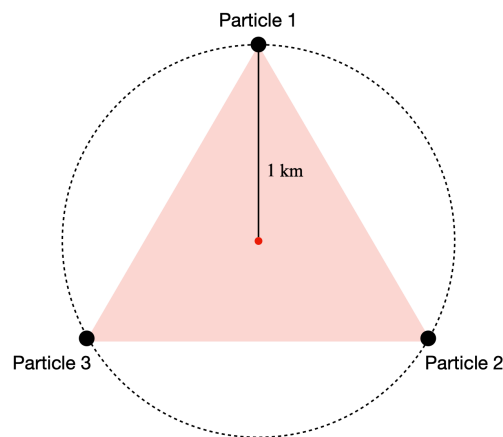


Figure 6.1: Sketch of the initial configuration of a triplet. Black dots are the particles. The red dot is the center of mass of the triplet.

The zone studied is a SWOT crossover region, where ascending and descending satellite tracks intersect, indicated by a red circle in Fig. 6.2. During SWOT's fast-sampling calibration-validation phase, the satellite passes over this crossover zone twice daily, completing daily cycles and achieving higher temporal resolution. The Kuroshio region was specifically selected for its distance from the

coast and its well-documented Eulerian properties [112, 113].

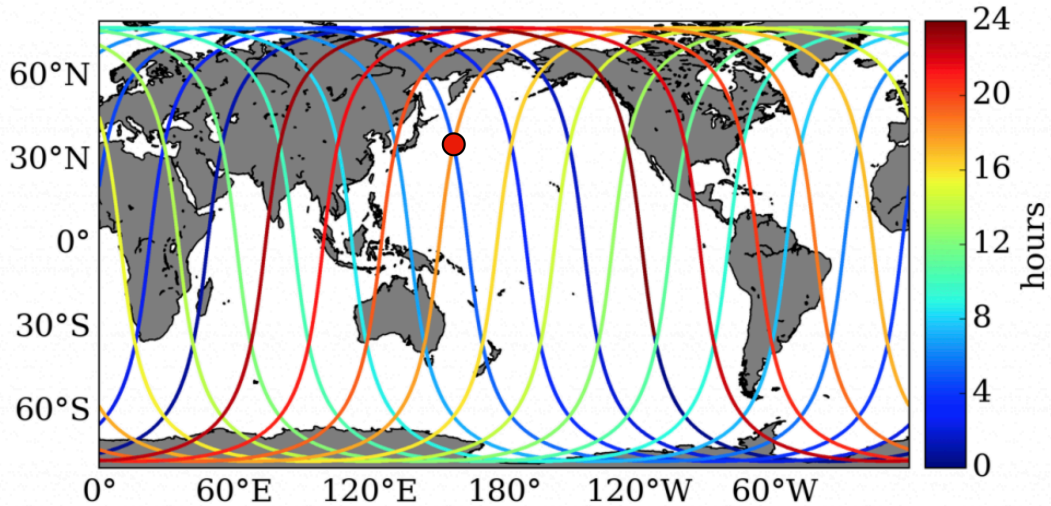


Figure 6.2: SWOT orbit during the fast-sampling phase (adapted from [110]). The red point indicates the location of the Kuroshio study zone

The Lagrangian dataset, which includes information on all particles, is approximately 369 GB for a one-month period. To analyze the results, we employed a parallel computing approach using the Datarmor supercomputer at IFREMER in Brest. Parallelization was achieved with the `Dask` and `Xarray` libraries in Python. `Xarray` extends the capabilities of Numpy arrays and Pandas dataframes, facilitating the manipulation of multidimensional datasets, and is widely used in atmospheric and oceanographic research. `Dask` enables efficient parallel computing by allowing users to handle computations that exceed memory limits or require parallel processing.

Figure 6.3a shows the SST field from the LLC4320 simulation on February 1, 2012, focusing on a restricted area within the Kuroshio zone, indicated by the white box. An initial distribution of 3600 particles was considered for analysis in this area. Over time, the particles disperse and sample a region larger than their initial starting area. Consequently, we decided to focus on the Eulerian properties of the region that encompasses all the particles at the end of the observation period. The green box in Fig. 6.3b highlights the studied region.

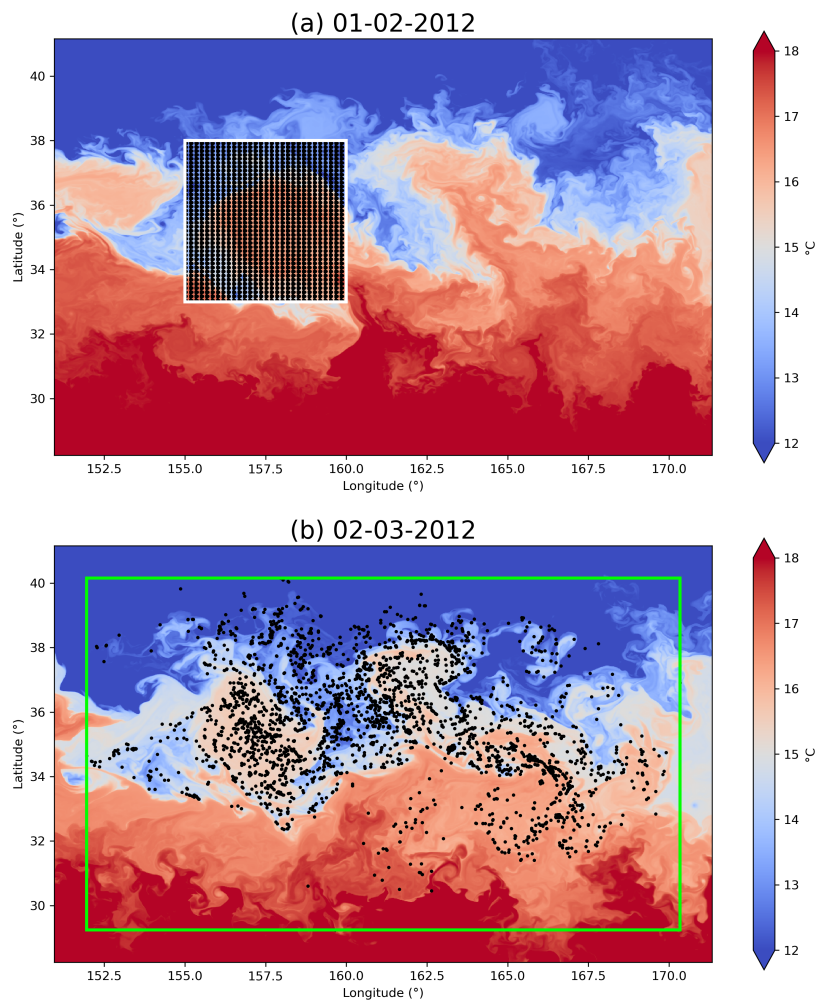


Figure 6.3: Snapshot of the SST field from the LLC4320 simulation of the Kuroshio zone on February 1, 2012, and 30 days later, in panels (a) and (b), respectively. Each panel includes black points representing the particles selected for the Lagrangian analysis. The white box in panel (a) outlines the initial sampling domain, where these particles were initially seeded. The green box in panel (b) marks the studied domain, which encompasses all particles at the final time of the study.

6.2 Internal Gravity Waves

Internal gravity waves form due to stratification within the ocean, where the deeper waters are usually colder, denser, and have higher salinity compared to shallower waters, which are relatively warm, less dense, and fresher. Such conditions create fluid layers that, while part of a continuous stratification,

can be understood by analogy as behaving like separate fluids. These density variations in the ocean interior generate buoyancy waves, known as internal gravity waves. As these waves propagate through the denser layers below the surface, they induce oscillations in the less dense layers above. In turn, they cause surface water to accumulate over the troughs and to stretch over the crests, forming alternating lines of smooth and rough water. These dynamics appear in satellite images as changes in surface texture: calmer areas reflect more light and thus appear brighter. In comparison, rougher areas scatter light more diffusely and thus appear darker, as shown in Fig. 6.4. However, since these internal gravity waves do not always significantly alter surface wave heights, they are often unnoticeable from boats.

These waves can propagate vertically and horizontally, not limited to the interfaces between the fluid layers. Buoyancy forces primarily drive these IGWs in the ocean. In a uniformly stratified fluid, where N , the buoyancy frequency, is constant, we can assume a plane wave solution [114], and the dispersion relation is expressed as:

$$\omega^2 = N^2 \cos^2 \Theta, \quad (6.1)$$

where ω is the wave frequency and Θ is the angle of the wave with the horizontal. For internal waves in the x - z plane, $\cos^2 \Theta = k_x^2 / (k_x^2 + k_z^2)$, where k_x and k_z are the wavenumbers corresponding to the x and z directions, respectively. When their periods approach about a day, they are influenced by Coriolis forces and feel the Earth's rotation; these are referred to as inertial waves. The dispersion relation for IGWs is given by

$$\omega^2 = c^2 k^2 + f^2 \quad (6.2)$$

where c , k , and f are the phase speed of the wave, isotropic horizontal wavenumber, and Coriolis parameter, respectively. A detailed derivation of this dispersion relation can be found in [114]. This relation can be reformulated to incorporate the deformation radius L_d , which approximately measures the distance an object travels at speed c before being influenced by Coriolis forces over a time span of f^{-1} . Consequently, the deformation radius is approximated as $L_d \approx c/|f|$, where $c = \sqrt{gH}$ in the shallow water limit, with H representing the mean fluid depth [114]. Thus, the dispersion relation becomes $\omega^2 = f^2 (L_d^2 k^2 + 1)$.

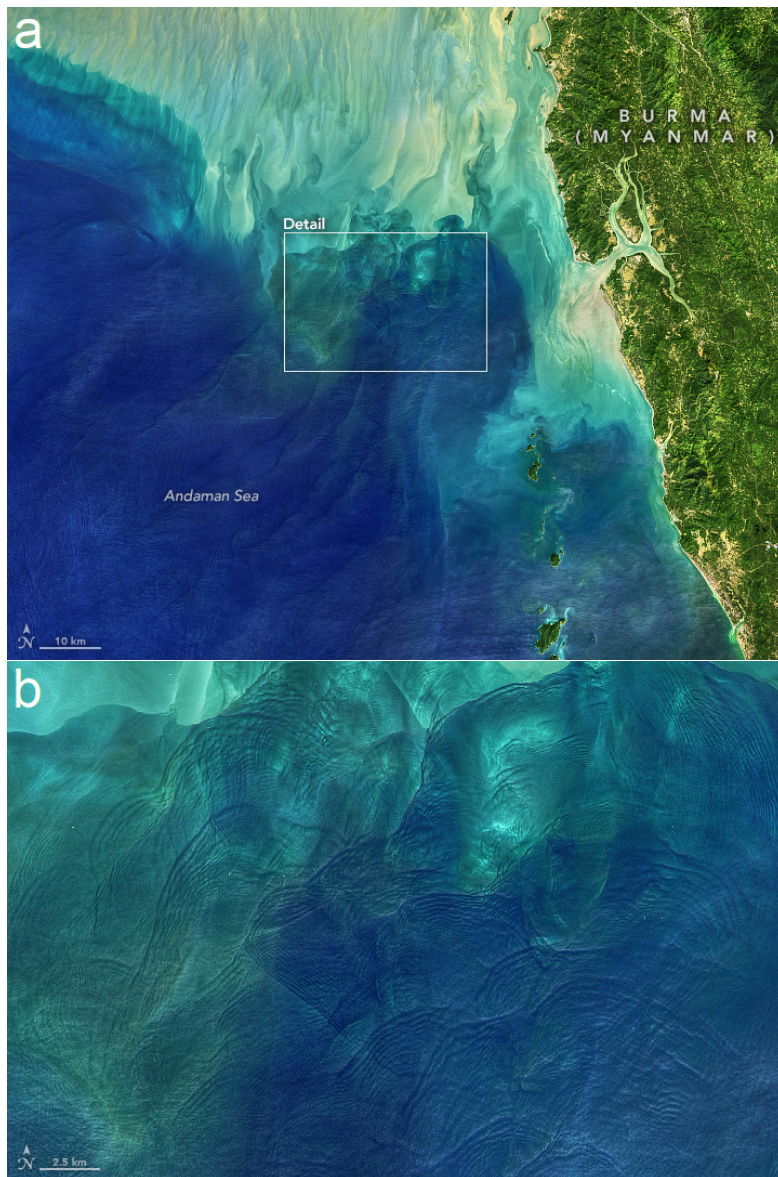


Figure 6.4: Images of the Andaman Sea captured by the Operational Land Imager (OLI) on Landsat 8 on November 29, 2019. Panel (a) shows a comprehensive view of the sea and coast, while panel (b) shows a detailed view of the area within the white box shown in panel (a). The sunglint effect enhances the visibility of internal waves, with color enhancements helping to distinguish detailed water features. Lighter and darker tones indicate variations in water depth (darker is deeper) and suspended sediments from nearby rivers (from the [NASA Earth Observatory](#)).

This dispersion relation is important for distinguishing between internal waves and mesoscale/submesoscale turbulent motions. By performing a spec-

tral analysis of the kinetic energy in the frequency and wavenumber domains, following the methodologies of [111, 113, 115], we can effectively highlight the influence of various oceanic processes. The frequency-wavenumber spectrum allows us to identify distinct dynamical regimes, including IGWs, high-frequency submesoscales, low-frequency submesoscales, and the transition from mesoscale to submesoscale, as shown in Fig. 6.5. Low-frequency motions have frequencies smaller than f_o , the Coriolis frequency, while IGWs lie above the dispersion relation curve associated with the 10th baroclinic vertical mode. This mode corresponds to the highest baroclinic mode resolved in the LLC4320 simulation and is the most relevant one for partitioning motions into balanced mesoscale/submesoscale motions and IGWs [113]. This partitioning method is essential because IGWs and high-frequency submesoscales share similar frequencies, making it difficult to distinguish between them using simple filtering techniques, such as filtering based solely on f_o or M_2 , the semidiurnal tidal frequency.

Before computing the $\omega - k$ spectrum for a given variable, linear trends in both space and time are removed. The dataset is then multiplied by a Hanning window applied across the spatial and temporal dimensions. Next, a discrete three-dimensional Fourier transform is performed, with two dimensions representing space and one representing time. The resulting transform is then used to compute a two-dimensional spatiotemporal spectral density. This process follows the methodology described in [113] and can be implemented using `xrft`, a Python package designed for performing discrete Fourier transforms on Xarray and Dask arrays.

6.3 Lagrangian Properties

In this section, we evaluate the Lagrangian statistics for the Kuroshio extension for February and August 2012. To compute these statistics, it is necessary to calculate distances. Since the particles are advected on the surface of a sphere, we use the Haversine formula to determine the spherical distance d , defined as:

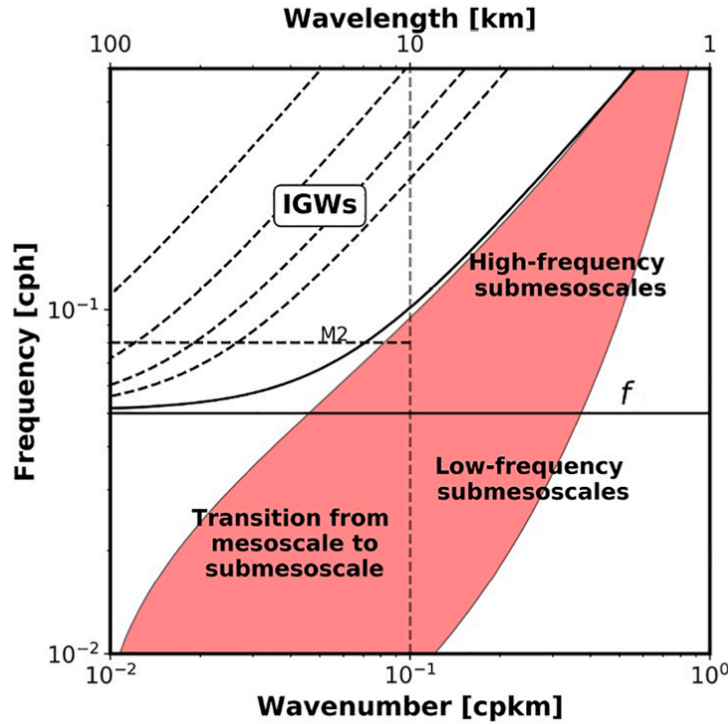


Figure 6.5: Schematic of the frequency-wavenumber spectrum showing the different dynamical regimes in the ocean: the low-frequency mesoscale/submesoscales, the high-frequency submesoscales, and IGWs. The dispersion relations for the first 4 baroclinic modes (dashed lines) and the 10th mode (solid line) are plotted. f and M_2 are the Coriolis and semidiurnal tidal frequencies, respectively. M_2 is related to the direct gravitational effect of the Moon on the tides (adapted from [115]).

$$d = 2r \arcsin \sqrt{\sin^2 \left(\frac{\phi_2^d - \phi_1^d}{2} \right) + \cos \phi_1 \cos \phi_2 \sin^2 \left(\frac{\lambda_2^d - \lambda_1^d}{2} \right)}, \quad (6.3)$$

where, r represents the Earth's radius, ϕ_1^d and ϕ_2^d are the longitudes, and λ_1^d and λ_2^d are the latitudes of the two points on the globe. The superscript d is used to distinguish these symbols from those used in Chap. 2. In this chapter, unless otherwise specified, one-particle and two-particle dispersion statistics are calculated using the Haversine formula in Eq. (6.3).

For the dispersion statistics in this section, the uncertainty is estimated as

the 95% confidence interval of the bootstrapped mean from 1000 samples.

Unlike in Chapters 4 and 5, here we begin with an analysis of the Lagrangian properties, aiming to follow a methodology similar to that used for analyzing drifter data. We start by examining the trajectories of the drifters, and then investigate how various flow features influence their advection.

6.3.1 One-Particle Statistics

We start by considering the single-particle statistics discussed in Chapter 2, Sec. 2.5.1. Figure 6.6a shows the absolute dispersion $\langle A^2 \rangle$, defined by Eq. (2.48). For both February and August, at short times we find a quite good agreement with the ballistic prediction, while at large times (roughly $t > 5$ days) diffusive scaling sets in. The velocity autocorrelation function, defined by Eq. (2.51), decreases approximately exponentially (see inset of Fig. 6.6a). The crossover time between the ballistic and diffusive regime of $\langle A^2 \rangle$ is close to the value of τ_L estimated from the first zero-crossing of $C(\tau)$. The velocity autocorrelation function is related to the Lagrangian frequency spectrum by a Fourier transform. At low frequencies, for an exponential decay of $C(\tau)$, one expects the kinetic energy frequency spectrum $E(\omega)$ to follow a ω^{-2} scaling [17]. This behavior is observed in Fig. 6.6b, where $E(\omega) \sim \omega^{-2}$, particularly in February, while in August, the slope is steeper for intermediate frequencies, i.e., $10^{-5} \lesssim \omega \lesssim 10^{-4}$. Additionally, we can distinguish two peaks corresponding to waves with periods $T_f \approx 20.53$ hours and $T_{M_2} \approx 12.65$ hours, which are the respective periods for the Coriolis and tidal frequencies. In August, the peaks associated with these internal waves are more pronounced.

Coherently with previous studies, the kinetic energy in winter is higher than in summer, leading to higher absolute dispersion in February in the Kuroshio Extension [13, 113]. This result implies that, while the overall behavior of absolute dispersion is similar in the two flows, the distance traveled by particles is, in a mean-square sense, larger under advection in winter.

Next, we can calculate the absolute diffusivity K_{abs} , which is the time deriva-

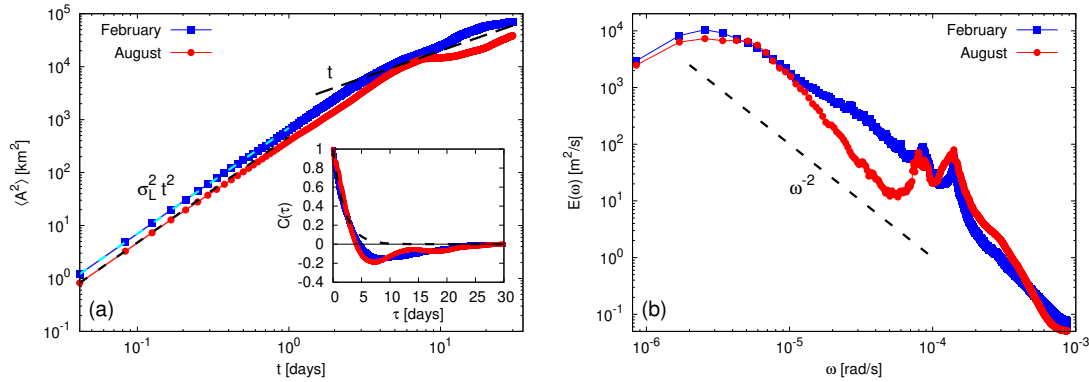


Figure 6.6: (a) Absolute dispersion $\langle A^2 \rangle$, for February and August, as a function of time. $\sigma_L^2 t^2$ is the expectation in the short-time ballistic regime, represented by the cyan and black short-dashed lines for February and August, respectively. The t scaling law (long-dashed line) is the expectation in the diffusive regime. Uncertainties, estimated as the 95% confidence interval, are mostly of the order of the point size. Inset: Lagrangian velocity autocorrelation function $C(\tau)$ versus time. The dashed black line corresponds to a decreasing exponential function. (b) Lagrangian frequency spectrum of the kinetic energy $E(\omega)$ for February and August. The ω^{-2} scaling law corresponds to an exponential decay of the Lagrangian velocity autocorrelation function [17].

tive of the absolute dispersion. This is defined by the equation:

$$K_{abs} = \frac{1}{2} \frac{d\langle A^2 \rangle}{dt}. \quad (6.4)$$

As shown in Fig. 6.7, the absolute diffusivity agrees with the trends observed in the absolute dispersion. In the early ballistic regime, $K_{abs} \sim \sigma_L^2 t$. It then transitions to the diffusive regime, where K_{abs} becomes constant at approximately 10^4 m²/s, around a similar crossover time estimated from both the absolute dispersion and the first zero crossing of $C(\tau)$.

6.3.2 Two-Particle Statistics

We now move to two-particle statistics, which depend on velocity-field spatial increments and provide insight into the tracer pair-separation process. A natural approach to this analysis is to measure the mean-square relative displacement between two particles as a function of time, i.e., relative dispersion $\langle R^2(t) \rangle$. Here, we consider only original pairs, initially separated by a distance $R_0 \approx 3.48$ km, with each triplet contributing three pairs (one for each side of the triangle in

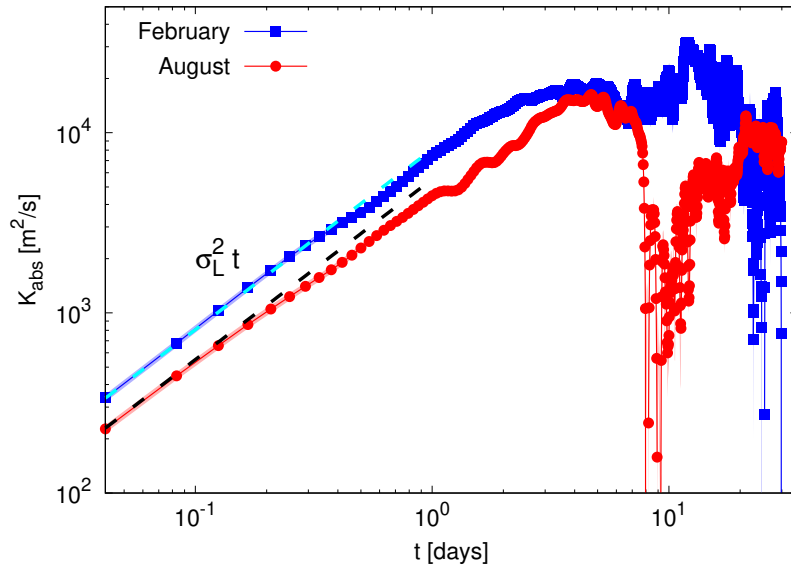


Figure 6.7: Absolute diffusivity K_{abs} , for February and August, as a function of time. $\sigma_L^2 t$ is the expectation in the short-time ballistic regime, represented by the cyan and black short-dashed lines for February and August, respectively. In the diffusive regime, K_{abs} converges to a constant value. Uncertainties, estimated as the 95% confidence interval, are mostly of the order of the point size.

Fig. 6.1).

Figure 6.8 shows the normalized relative dispersion after subtracting the initial value as a function of time. At short times, we observe a t^2 scaling law, indicating a ballistic regime. Specifically, $(\langle R^2 \rangle - R_0^2)/R_0^2 \approx Z t^2$, where $Z = \langle \zeta^2/2 \rangle_x$ [52, 56]. This provides the first link between the Lagrangian and Eulerian properties of the flow, as enstrophy is calculated solely from the Eulerian velocity gradients. In fact, this holds well for February, when vorticity dominates the flow. However, in August, a slight deviation is observed, likely due to an increase in flow divergence [113, 115], making the substitution of $\langle (\delta \mathbf{u}_0)^2 \rangle$ in Eq. 2.53 with $Z R_0^2$ less reliable. At intermediate times [$1 \text{ day} < t < 10 \text{ days}$], in February, $\langle R^2(t) \rangle \sim$ follows a behavior close to t^3 , the Richardson expectation, before a transition to a t scaling at large enough times. In August, within the same time range, relative dispersion increases more rapidly with a slightly steeper slope before eventually transitioning to what appears to be a t^3 scaling. However, as mentioned in Secs. 2.5.2, 4.2.1, and 5.2, relative dispersion has its drawbacks

when interpreting scaling laws in the inertial range, making it difficult to draw definitive conclusions. At short times ($t < 1$ day), the relative dispersion in February is larger than in August, suggesting that the vorticity of the flow is stronger in winter in the Kuroshio extension.

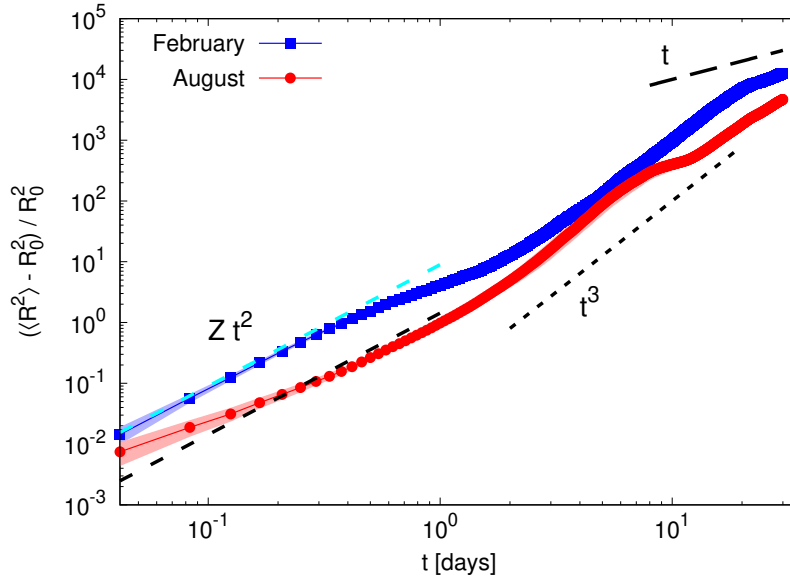


Figure 6.8: Relative dispersion normalized by its initial value (after subtracting the initial value) $(\langle R^2 \rangle - R_0^2) / R_0^2$, for February and August, as a function of time. $Z t^2$ is the expectation in the short-time ballistic regime, represented by the cyan and black short-dashed lines for February and August, respectively. The t^3 scaling law is the Richardson expectation for a kinetic energy spectrum $E(k) \sim k^{-5/3}$. The t scaling law (long-dashed line) is the expectation in the diffusive regime. Uncertainties, estimated as the 95% confidence interval, are mostly of the order of the point size.

From the relative dispersion, we can easily compute the relative diffusivity shown in Fig. 6.9 as a function of the separation distance $\langle R^2 \rangle^{1/2}$. In February, at intermediate scales [$10 \text{ km} < R < 100 \text{ km}$], K_{rel} exhibits a scaling close to $R^{3/2}$, which would correspond to a kinetic energy spectrum $E(k) \sim k^{-2}$. In August, however, accounting for uncertainties, K_{rel} follows a behavior closer to R^2 , indicating a smooth flow where $\beta > 3$. At large scales, relative diffusivity reaches a constant value. This is clear for February and less so for August, where $K_{rel} \sim 2K_{abs}$ [17]. Instead, in August, beyond the visible dip around 70km, relative diffusivity approaches $R^{3/2}$, consistent with the qualitative observation from relative dispersion, where at large scales, it scales more slowly. In February,

relative dispersion and diffusion suggest two slightly different behaviors in the inertial range, with one indicating a scaling law corresponding to $\beta = 5/3$ and the other to $\beta = 2$. In August, fitting an exponential law for relative dispersion that matches the R^2 scaling observed in relative diffusion is difficult. However, accurately determining the scaling from relative dispersion is particularly challenging when the inertial range is limited [74].

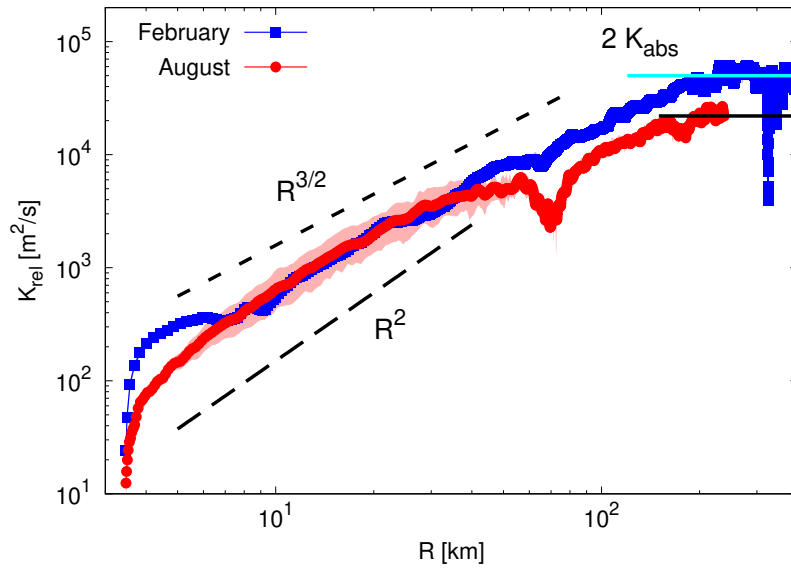


Figure 6.9: Relative diffusivity K_{rel} , for February and August, as a function of time. The $R^{3/2}$ and R^2 scaling laws (short-dashed and long-dashed lines) correspond to $\beta = 2$ and $\beta > 3$, respectively. In the diffusive regime, the relative diffusivity is constant such that $K_{rel} \sim 2K_{abs}$, represented by the cyan and black solid lines for February and August, respectively. Uncertainties are estimated as the 95% confidence interval.

Another indicator used to characterize the dispersion process is the kurtosis of the pair relative displacement. Unlike the relative dispersion and diffusivity, the difference in kurtosis behavior between winter and summer is quite evident (Fig. 6.10). At short times, the kurtosis grows to values an order of magnitude higher in August than in February and then decreases rapidly. In February, the kurtosis remains close to $ku = 5.6$, the Richardson expectation, before decreasing to $ku = 2$, in line with the diffusive regime expectation. These observations, along with those from relative diffusivity, suggest that in February, dispersion is local, while in August, it is nonlocal. This aligns with the fact that smaller

structures and the flow in general are more energetic in winter. [13, 113].

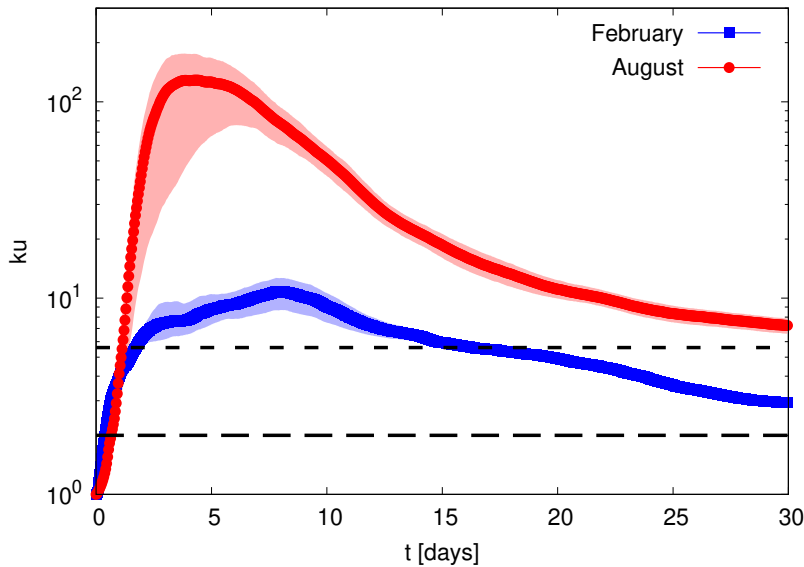


Figure 6.10: Kurtosis of separation ku , for February and August, as a function of time. The horizontal short-dashed line is the expectation $ku = 5.6$ in the Richardson regime, while the horizontal long-dashed line is the expectation $ku = 2$ in the diffusive regime. Uncertainties are estimated as the 95% confidence interval.

So far, we have focused on fixed-time indicators, which share similar drawbacks with relative dispersion; however, fixed-scale indicators are often preferred for identifying dispersion regimes [59]. A commonly used fixed-scale indicator is the FSLE (Finite-Scale Lyapunov Exponent), a scale-by-scale dispersion rate defined by Eq. (2.57). In February, at small scales and up to approximately 100 km, the FSLE follows a $\delta^{-1/2}$ scaling law, corresponding to a kinetic energy spectrum $E(k) \sim k^{-2}$. In contrast, the FSLE remains constant in August with $\lambda(\delta) \approx 0.15 \text{ days}^{-1}$ across that range of scales. Between 100 and 400 km, both FSLEs are not too different. This is in line with the relative diffusivity, where both relative diffusivities grow approximately as $R^{3/2}$ in a similar range of scales. Additionally, in relative dispersion, we observe that after 10 days, both cases follow a t^3 scaling. In both cases, the FSLE eventually transitions to a diffusive regime, indicated by a δ^{-2} scaling law. The high dispersion rate values, in February, in the submesoscale range indicate that LLC4320 effectively captures small-scale dynamics, outperforming other ocean circulation models, such as

the one used in [26] (see Fig. 1.8).

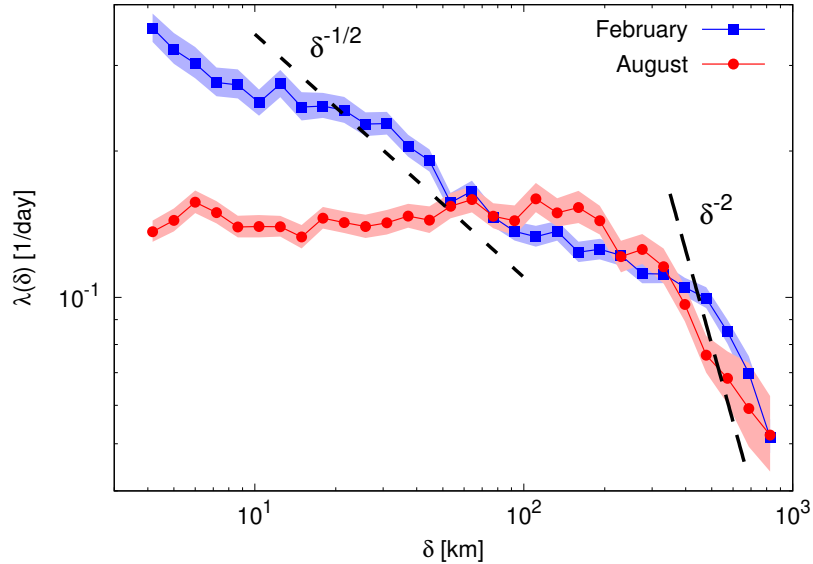


Figure 6.11: FSLE $\lambda(\delta)$, for February and August, as a function of separation. The $\delta^{-1/2}$ scaling law (short-dashed line) corresponds $\beta = 2$. In the diffusive regime, the FSLE scales as δ^{-2} (long-dashed line). Uncertainties are estimated as the 95% confidence interval.

These results demonstrate that in the studied region, the season significantly influences Lagrangian transport. The coherence observed in both winter and summer highlights how the dispersion processes vary: in winter (February), dispersion is local, while in summer (August), it is nonlocal. Notably, the kinetic energy spectral slope, β , inferred from the FSLE in February, matches the relative diffusivity. In August, the constant FSLE at scales below 100 km is consistent with the relative diffusivity scaling law.

Since submesoscales are more intense in winter and IGWs are stronger in summer, we aim to understand what drives dispersion in each season and whether IGWs have a prominent effect. This will be further explored in the following section, where we investigate the influence of internal gravity waves on the Eulerian flow properties to better understand their impact on Lagrangian statistics.

6.4 Eulerian Properties

In this section, we explore the Eulerian properties of the flow in the Kuroshio Extension (Fig. 6.3) to identify links between the Lagrangian and Eulerian characteristics and to understand the drivers of the dispersion process in this region. As previously mentioned, LLC4320 models both low- and high-frequency motions, unlike the SQG framework, which accounts only for low-frequency motions.

First, we analyze the $\omega-k$ spectrum to better understand the respective contributions of mesoscale/submesoscale motions and IGWs to the total kinetic energy spectrum $E(k, \omega)$. Figure 6.12 shows frequency-wavenumber spectra of the kinetic energy for February (Fig. 6.12a) and August (Fig. 6.12b). The distinction between mesoscale/submesoscale motions and IGWs is made using the dispersion-relation curve for the 10th vertical mode (dashed-dotted line in Fig. 6.12). Previous studies have shown this to be an effective method for distinguishing between the two [113, 115]. In winter, low-frequency mesoscale/submesoscale motions clearly dominate the flow, whereas, in summer, IGWs become more energetic, with a significant concentration of energy around the M_2 , and submesoscale motions are considerably less energetic. Moreover, it is important to note that in winter, submesoscale motions also encompass high-frequency motions, while in summer, IGWs influence high wavenumbers, reaching up to approximately 50 km.

Using the $\omega-k$ spectra, we compute the wavenumber spectra of kinetic energy as $E(k) = \int E(k, \omega) d\omega$, integrated over all frequencies. These wavenumber spectra are presented in Fig 6.13. The results confirm the inference from the Lagrangian statistics that the flow in February is more energetic than in August, particularly at scales < 100 km. In February, the kinetic energy spectrum follows a k^{-2} scaling, while in summer, the slope steepens to $E(k) \sim k^{-2.3}$. Interestingly, the winter scaling law ($\beta \approx 2$) aligns with the predictions from Lagrangian statistics. Relative dispersion, while suggesting a slightly different scaling of $\beta = 5/3$, is still close to what is observed here and in the other Lagrangian indicators. In summer, $\beta \approx 2.3$, which would typically suggest local dispersion. However, the Lagrangian statistics indicate nonlocal dispersion, prompting us to delve deeper into the Eulerian statistics to better explore the underlying processes.

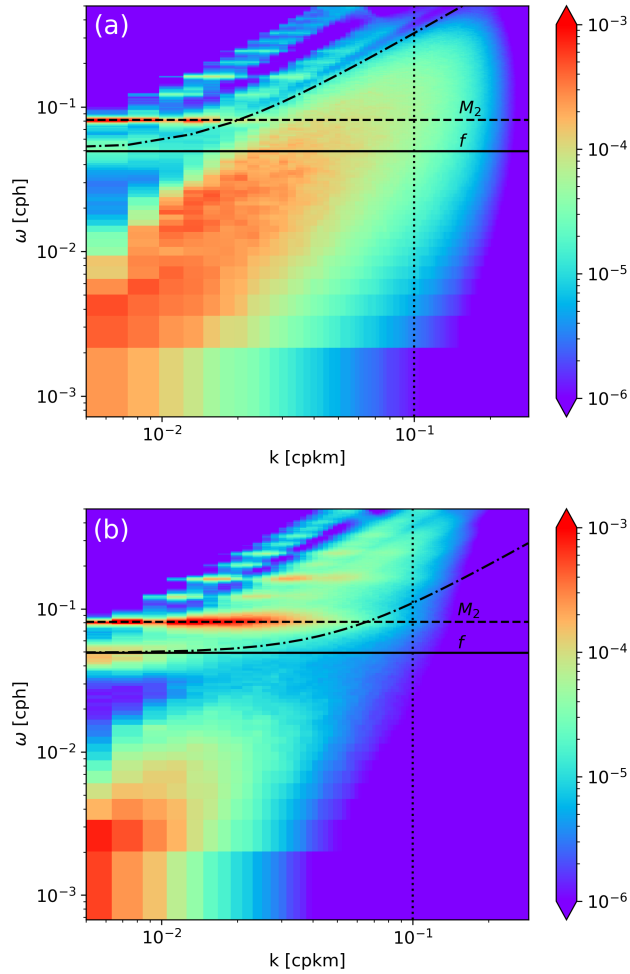


Figure 6.12: Frequency-wave number spectra of kinetic energy $E(k, \omega)$ corresponding to the Kuroshio Extension during February (a) and August (b). The spectra are multiplied by k and ω , indicating the spectra are variance preserved [113]. The solid and dashed lines represent the Coriolis and tidal frequencies, respectively, while the dashed-dotted line represents the dispersion relation of mode-10.

To understand the contribution of IGWs to the total kinetic energy, we separate the energy from mesoscale/submesoscale motions and IGWs. Using the dispersion relation for mode-10 and considering L_R as the 10th baroclinic deformation radius, we partition $E(k, \omega)$ into two sections: $\omega^2 < f^2(1 + L_R^2 k^2)$ for mesoscale/submesoscale motions, and $\omega^2 > f^2(1 + L_R^2 k^2)$ for IGWs. For the remainder of this section, L_R will be considered as the 10th baroclinic deformation radius.

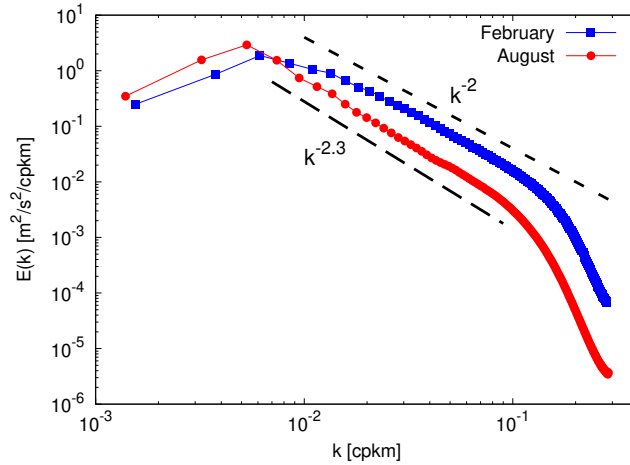


Figure 6.13: Wavenumber spectra of kinetic energy, calculated from the $\omega - k$ kinetic energy spectrum, where $E(k) = \int E(k, \omega) d\omega$, for February (blue) and August (red). The scaling laws k^{-2} and $k^{-2.3}$ represent the fitted slopes for February and August, respectively.

This partitioning reveals that in February (winter; Fig. 6.14a), mesoscale/submesoscale motions account for most of the kinetic energy in the surface flow: the kinetic energy spectrum from these motions is identical to the total kinetic energy spectrum, both following a k^{-2} scaling. IGWs contribute relatively little energy and have a minimal effect on the total energy.

In August (summer; Fig. 6.14b), we observe that at small wavenumbers (i.e., scales > 100 km), mesoscale motions dominate, while at large wavenumbers (i.e., scales < 50 km), submesoscale motions become less energetic and IGWs dominate the flow. In this range, the IGWs' kinetic energy spectrum scales as $k^{-2.3}$, while the mesoscale/submesoscale kinetic energy spectrum essentially follows k^{-3} .

Based on these observed slopes, we can argue that in winter, in the Kuroshio Extension, dispersion is local and primarily driven by mesoscale/submesoscale motions. In summer, dispersion is nonlocal and also primarily driven by mesoscale/submesoscale motions. However, it is important to note that the partitioning was necessary to conclude this, as the full kinetic energy spectrum shows a $k^{-2.3}$ scaling law, which would imply a local dispersion regime based on usual dimensional arguments. By removing the IGW contribution, we retrieve a k^{-3} scaling law, consistent with nonlocal dispersion and the Lagrangian statistics.

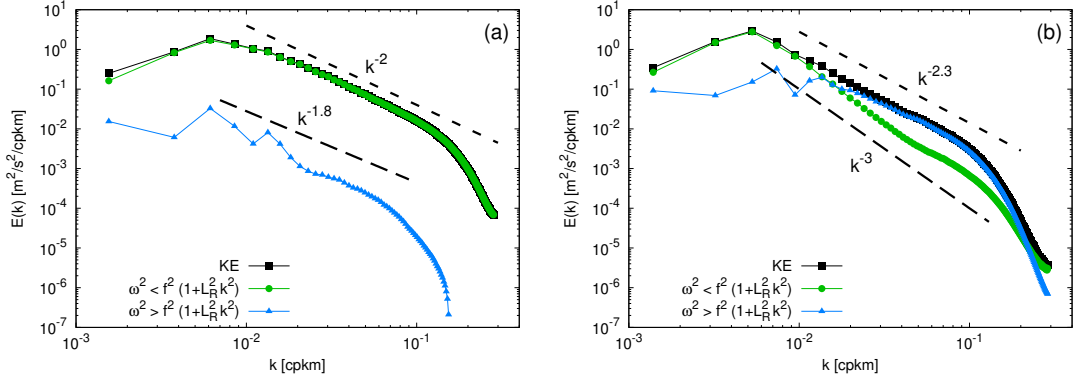


Figure 6.14: Wavenumber spectra of kinetic energy $E(k)$ derived from surface velocities: total kinetic energy (KE in black), and filtered using the mode-10 dispersion relation to isolate mesoscale/submesoscale motions (in green) and IGWs (in blue), for February (a) and August (b). In (a), the scaling laws k^{-2} and $k^{-1.8}$ represent the fitted slopes for mesoscale/submesoscale motions and IGWs, respectively. In (b), the scaling laws k^{-3} and $k^{-2.3}$ represent the fitted slopes for mesoscale/submesoscale motions and IGWs, respectively.

Another method of partitioning the kinetic energy is by decomposing it into rotational (KE_{ζ}) and divergent (KE_{Δ}) components, using Helmholtz decomposition [5]. These components are computed as follows:

$$KE_{\zeta} = \frac{1}{2} \int \frac{|\hat{\zeta}(k, \omega)|^2}{k^2} d\omega \quad (6.5)$$

and

$$KE_{\Delta} = \frac{1}{2} \int \frac{|\hat{\Delta}(k, \omega)|^2}{k^2} d\omega, \quad (6.6)$$

where $\hat{\zeta}(k, \omega)$ and $\hat{\Delta}(k, \omega)$ are the spatiotemporal Fourier transforms of vorticity ζ and divergence Δ , respectively [113].

To link these components to mesoscale motions and IGWs, mesoscale motions are typically assumed to be nondivergent [116]. This assumption is not entirely accurate, as submesoscale motions are known to be divergent [3, 117, 118]; therefore, the divergent component KE_{Δ} accounts for the submesoscale-induced divergence in addition to the IGW-induced divergence. However, several studies have shown that this assumption works well to differentiate between mesoscales and IGWs [109, 113, 116].

To address this limitation, we use the mode-10 dispersion relation and partition

each component into two sections. KE_{ζ}^{-} and KE_{Δ}^{-} represent the section where $\omega^2 < f^2(1 + L_R^2 k^2)$ for mesoscale/submesoscale motions, while KE_{ζ}^{+} and KE_{Δ}^{+} correspond to $\omega^2 > f^2(1 + L_R^2 k^2)$ for IGWs.

Figure 6.15 shows the partitioning for February [panels (a) and (b)] and August [panels (c) and (d)]. In February, the flow is dominated by intense vorticity primarily from mesoscale/submesoscale motions. The divergent component contributes minimally to the total energy, with IGWs having relatively small kinetic energy. Moreover, the divergent component from both motions contributes little to the overall kinetic energy. In August, the situation is different: at large scales (i.e., > 100 km), vorticity from mesoscale/submesoscale motions dominates, while at smaller scales, divergence from IGWs becomes dominant. It is also worth noting that the vorticity spectrum from both mesoscale/submesoscale motions and IGWs is comparable at scales of $O(10)$ km, following a k^{-3} scaling law, again pointing to nonlocal dispersion. From this decomposition, we can conclude that dispersion is driven mainly by the rotational component of the flow, i.e., vorticity, which is primarily due to mesoscale/submesoscale motions in both cases. Notably, in summer, the rotational component associated with IGWs may also play a role at scales of $O(10)$ km, as it shows a similar magnitude and scaling to that of mesoscale/submesoscale motions.

A snapshot of the vorticity field highlights the difference in vorticity intensity between winter and summer. This is evident in Fig 6.16, where panel (a) shows the February vorticity field in the Kuroshio Extension, with vorticity present at both large and small scales, exhibiting relatively large values and sharp gradients. In contrast, panel (b) shows weaker vorticity in August, mostly confined to large-scale structures. Additionally, in February, one can clearly observe submesoscale structures comprising both vortices and filaments, whereas in August, submesoscales are not visible.

So far, we have examined kinetic energy spectra calculated from surface velocity, which account for both geostrophic and ageostrophic velocity components. However, as mentioned in previous chapters, SWOT measures SSH, from which we can calculate the kinetic energy spectrum using the geostrophic

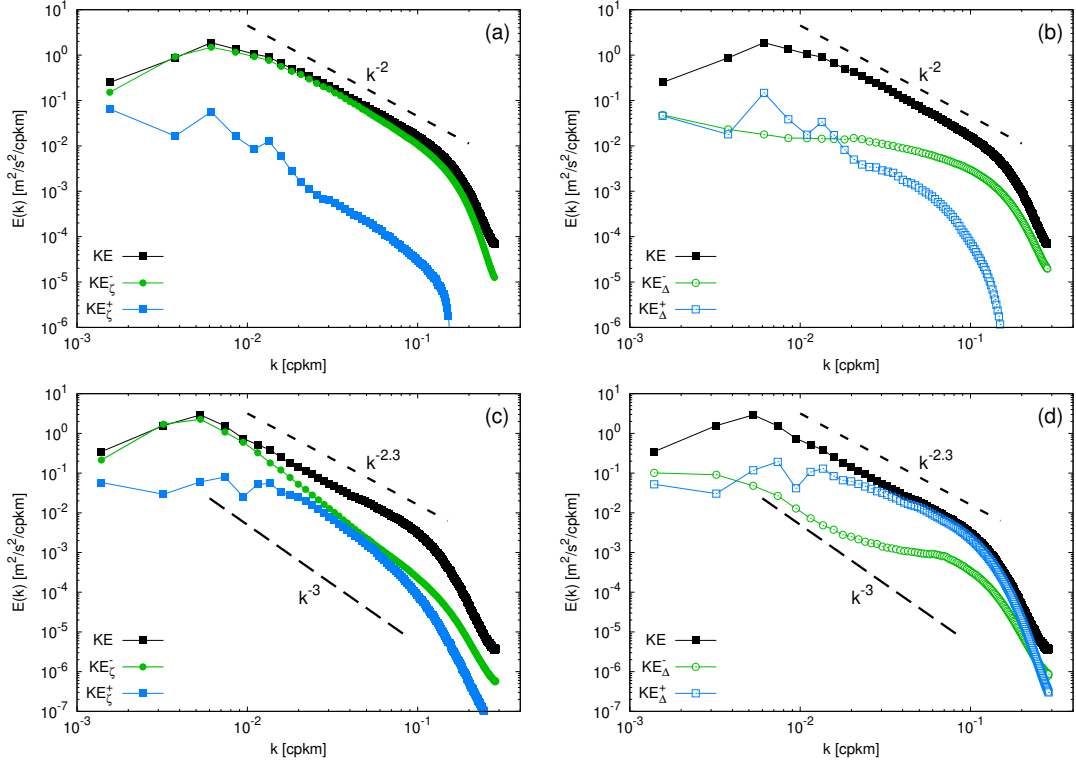


Figure 6.15: Wavenumber spectra of kinetic energy $E(k)$ derived from surface velocities: total kinetic energy KE (in black), the solenoidal component of kinetic energy KE_{ζ}^{-} (filled points), and the divergent component KE_{Δ}^{+} (empty points), partitioned based on $\omega^2 < f^2(1 + L_R^2 k^2)$ and $\omega^2 > f^2(1 + L_R^2 k^2)$, represented by superscripts “-” and “+”, respectively. Panels (a) and (b) correspond to February, and panels (c) and (d) to August. In (a) and (b), the scaling law k^{-2} represents the fitted slope for KE_{ζ}^{-} . In (c) and (d), the scaling laws k^{-3} and $k^{-2.3}$ represent the fitted slopes for KE_{ζ}^{-} and KE_{Δ}^{+} , respectively.

approximation as follows:

$$E(k, \omega) = \frac{1}{2} |\hat{\eta}(k, \omega)|^2 \frac{g^2}{f^2} k^2, \quad (6.7)$$

or by using the dispersion relation for IGWs [119]:

$$E(k, \omega) = \frac{1}{2} |\hat{\eta}(k, \omega)|^2 g^2 f^2 \frac{\omega^2 + f^2}{(\omega^2 - f^2)^2}, \quad (6.8)$$

where $\hat{\eta}(k, \omega)$ is the spatio-temporal Fourier transform of SSH. Integrating the above over all frequencies gives the corresponding wavenumber kinetic energy

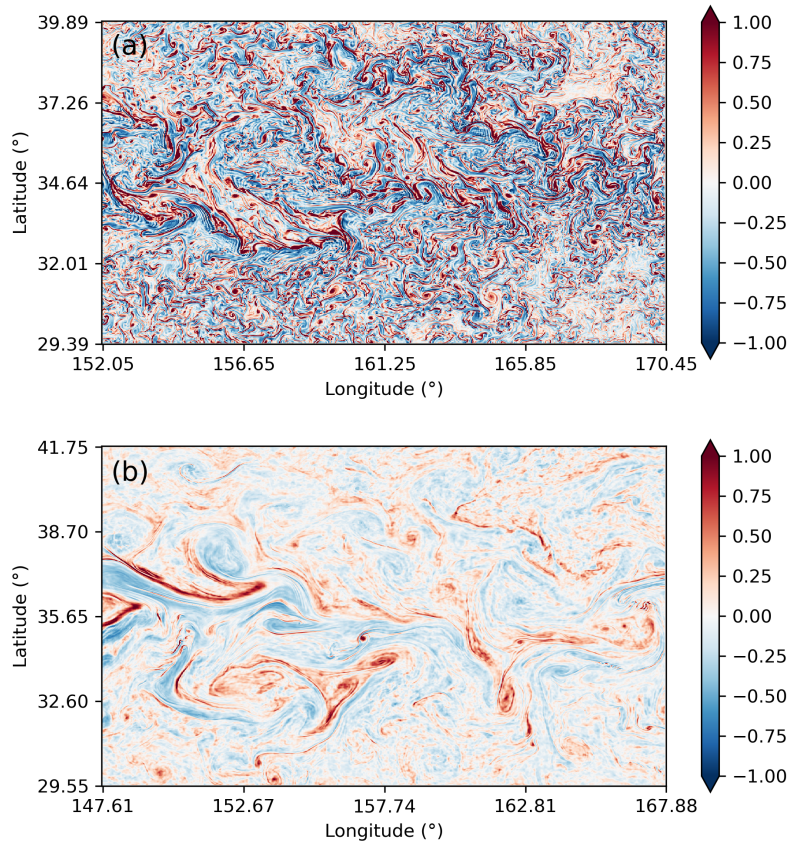


Figure 6.16: Snapshot of the vorticity, normalized by the Coriolis parameter ζ/f , for the studied zone in the Kuroshio Extension, for February 15, 2012 (a) and August 15, 2012 (b).

spectra, as shown in Fig. 6.17. Since the geostrophic approximation is primarily valid at the mesoscale and currently the best available method for submesoscales, we apply Eq. (6.7) for $\omega^2 < f^2(1 + L_R^2 k^2)$, and Eq. (6.8) for $\omega^2 > f^2(1 + L_R^2 k^2)$.

In February, when mesoscale/submesoscale motions dominate, the geostrophic approximation (6.7) provides a reasonable estimate of the kinetic energy spectrum, slightly underestimating the spectral slope (with $\beta \approx 1.8$) and overestimating the kinetic energy (see Fig. 6.17a). This discrepancy arises because geostrophic velocities derived from SSH tend to overestimate surface velocities in cyclonic eddies and underestimate them in anticyclonic eddies. In cyclonic eddies, characterized by depressions in SSH and counterclockwise rotation in the Northern Hemisphere, the SSH gradients are steeper. The geostrophic approximation calculates velocity based on these gradients, leading to higher estimated

velocities and, thus, higher kinetic energy in cyclone-dominated regions. Conversely, anticyclonic eddies exhibit elevated SSH and clockwise rotation with gentler SSH gradients. This results in lower estimated velocities and kinetic energy in anticyclone-dominated areas. The underlying reason is the interaction between the centrifugal and Coriolis forces in these eddies. The centrifugal force, always directed outward and equal in magnitude for both cyclonic and anticyclonic eddies, affects the force balance differently. In cyclonic eddies, the centrifugal force adds to the Coriolis force, requiring a stronger pressure gradient (and greater sea surface depression) to maintain balance. In anticyclonic eddies, the centrifugal force opposes the Coriolis force, resulting in a smaller pressure gradient and a less pronounced sea surface elevation [120]. This phenomenon is illustrated in the schematic of sea level shapes shown in Fig. 6.18. By examining the probability density function of vorticity in February shown in Fig. 6.19a, we observe a cyclonic dominance, with the right tail of the pdf ($\zeta > 0$) being significantly higher than the left ($\zeta < 0$). This cyclonic dominance contributes to overestimating kinetic energy when using the geostrophic approximation.

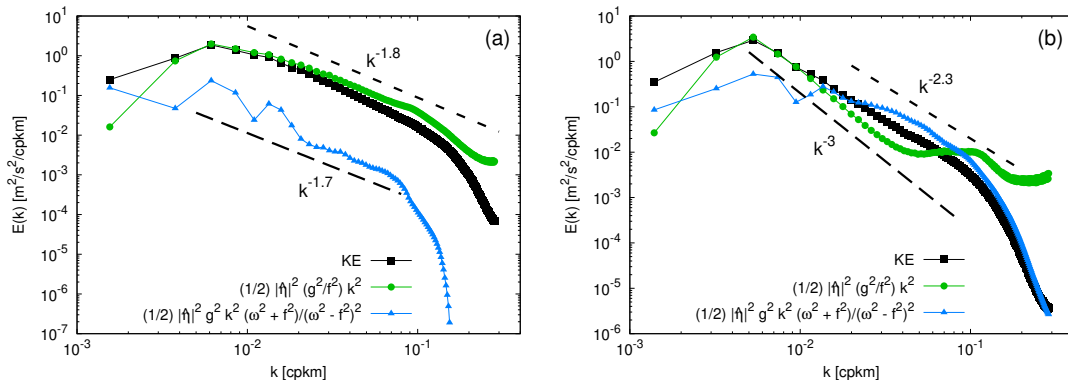


Figure 6.17: Wavenumber spectra of kinetic energy $E(k)$ derived from surface velocities: total kinetic energy (KE in black), from sea surface height η (geostrophic kinetic energy; green), and the kinetic energy of IGWs (blue), for February (a) and August (b). In (a), the scaling laws $k^{-1.6}$ and $k^{-1.7}$ represent the fitted slopes for the geostrophic kinetic energy and the IGWs kinetic energy, respectively. In (b), the scaling laws k^{-3} and $k^{-2.3}$ represent the fitted slopes for the geostrophic kinetic energy and the IGWs kinetic energy, respectively.

For August, at large scales (i.e., > 100 km), the geostrophic approximation estimates the kinetic energy well. At smaller scales (i.e., < 50 km), the dispersion relation best estimates the kinetic energy spectrum slope with $\beta \approx 2.3$ and over-

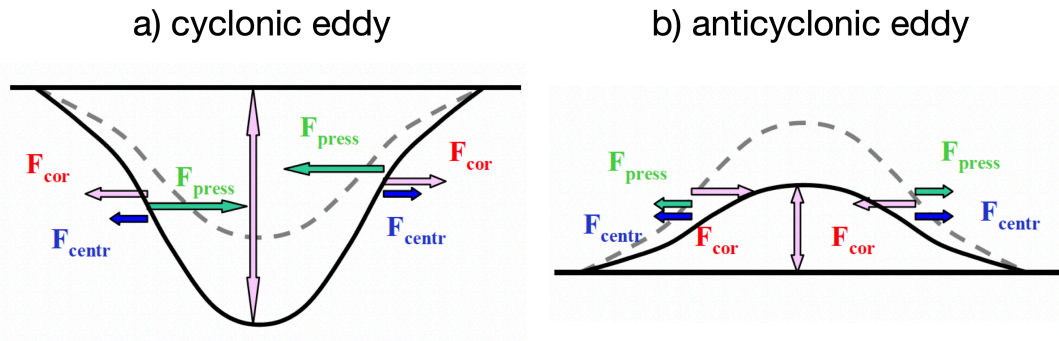


Figure 6.18: Schematics of sea level shape and force balance for cyclonic (a) and anticyclonic (b) Gaussian eddies of the same size (adapted from [120]). The dashed line indicates the geostrophic case. F_{cor} (pink arrows), F_{centr} (blue arrows), and F_{press} (green arrows) represent the Coriolis, centrifugal, and pressure forces, respectively.

estimated energy. In contrast, the geostrophic approximation, at scales between 20 and 50 km, overestimates the slope ($\beta \approx 3$) and underestimates the energy (Fig.6.17b). Interestingly, this scaling ($\beta = 3$) is similar to that obtained from the kinetic energy spectrum of mesoscale/submesoscale motions. A cyclonic dominance is also observed in August, as shown in Fig.6.19b. However, the previous explanation regarding the overestimation and underestimation of velocities from SSH in cyclonic and anticyclonic eddies does not apply when considering kinetic energy derived from the wave dispersion relation, as it is fundamentally based on the geostrophic approximation. Moreover, despite the cyclonic dominance, the underestimation of the geostrophic approximation at intermediate scales may be due to the significant contribution of IGWs to the energy of the flow in summer, in contrast to winter, when their influence is minimal.

We end this section with a final remark on the underestimation of β in February, which may be relevant for SWOT-derived velocities in winter in the Kuroshio Extension. Based on both Lagrangian and Eulerian statistics, we can conclude that the dispersion is local and primarily driven by mesoscale and sub-mesoscale motions. The small-scale pair-separation rate may be overestimated as the SSH-derived kinetic energy spectrum underestimates β .

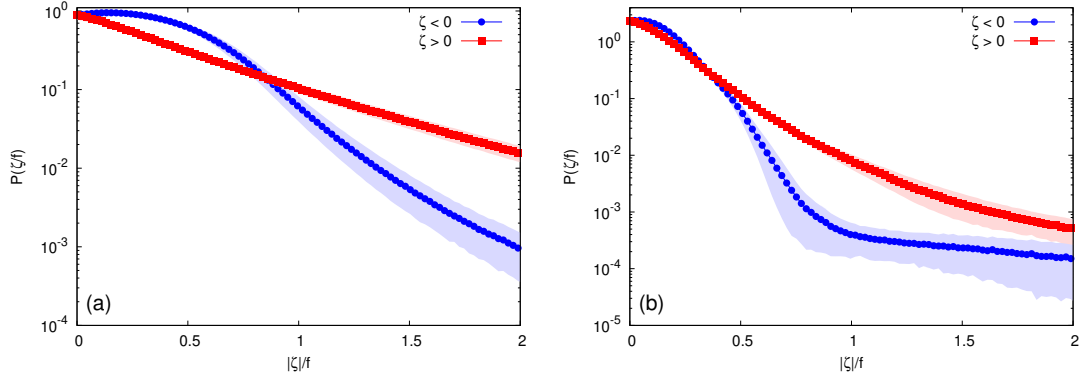


Figure 6.19: Probability density function of vorticity ζ (normalized by the Coriolis parameter f), temporally averaged over 30 days, for February (a) and August (b), with blue dots and red squares indicating $\zeta < 0$ and $\zeta > 0$, respectively. The shaded areas correspond to the standard deviation of the temporal statistics.

6.5 Conclusions

We investigated Lagrangian particle dynamics in the Kuroshio Extension during February and August, using the high-resolution ocean general circulation model, LLC4320, that incorporates internal gravity waves, which are not accounted for in the SQG⁺¹ framework. We focused specifically on particle dispersion and partitioning the flow into mesoscale/submesoscale motions and IGWs to better understand their impact on Lagrangian transport properties.

LLC4320 surface velocities were used to advect Lagrangian tracers over a 30-day period in February and August 2012. First, we investigated single-particle statistics and found that they are only weakly influenced by seasonality. We then moved to two-particle statistics, which provide insight into the pair-dispersion process and can be linked to the Eulerian properties of the flow. To better understand the contributions of the different ocean processes and their relation to the Lagrangian statistics, the frequency-wavenumber analysis of kinetic energy spectra, combined with the dispersion-relation curve, proved to be an effective tool for distinguishing between mesoscale/submesoscale motions and IGWs.

In February, dispersion is local and driven by mesoscale/submesoscale motions, with a kinetic energy spectrum $E(k) \sim k^{-2}$.

In August, the flow is less energetic, with mesoscale/submesoscale motions dominating at larger scales (i.e., > 100 km) and IGWs at smaller scales. Dispersion appears nonlocal and dominated by the mesoscale/submesoscale motions, with $E(k) \sim k^{-3}$.

To our knowledge, the effect of IGWs on Lagrangian tracer dispersion remains open and is not well documented. A study on pair separations in the Gulf of Mexico [75] noted that the FSLE should be affected by inertial oscillations, which is not the case in our study. However, a direct comparison is difficult since the FSLE plot is not shown in [75], and this point is only briefly mentioned in the corresponding text. Another study on dispersion by oceanic internal waves [121] shows that in the presence of mixed layer eddies, these eddies dominate dispersion in the mixed layer. Furthermore, while the FSLE is sensitive to inertial oscillations, this effect is observed at scales smaller than the inertial oscillation scale V/f , where V is the particle speed. In August, this inertial oscillation scale, in our case, is 4.59 km, which is close to the first separation value ($\delta \approx 4.17$ km) in the FSLE shown in Fig. 6.11. To resolve smaller scales, we would need a smaller initial separation between pairs (currently $R_0 \approx 3.48$ km). Resolving these smaller scales would, in fact, require a more refined simulation than LLC4320, as the inertial oscillation scale is close to the grid resolution, where the flow becomes completely smoothed out. Given these limitations, it seems reasonable that the FSLE does not capture the effect of IGWs and that dispersion is instead dominated by large eddies, which have higher energy than IGWs.

After the decomposition of the flow into rotational and divergent components, we found that in summer, in the inertial range (10 to 100 km), both mesoscale/submesoscale motions and IGWs contribute to the rotational component, whereas in winter, only the former does. Disentangling these processes in summer is challenging, as they operate on similar scales with comparable kinetic energy [115].

In relation to SWOT, in February, the geostrophic approximation effectively predicts the kinetic energy spectrum from SSH, with slightly overestimated energy and an underestimated slope. This underestimation of β is likely due to the dominance of cyclonic over anticyclonic vorticity and may lead to an overestimation of the pair-dispersion rates in the submesoscale range [120].

Another factor contributing to this overestimation is the nondivergent nature of SSH-derived flow, which allows pairs to disperse without being trapped in convergence regions that intensify as Ro increases [67]. In August, IGWs play a significant role, and the geostrophic approximation alone is insufficient to accurately estimate the kinetic energy spectrum and surface velocities from SSH. Both the geostrophic approximation and the dispersion relation are needed for accurate results, with the geostrophic approximation working well at large scales and the dispersion relation necessary at smaller scales dominated by IGWs.

A valuable perspective would be to expand this study to other regions and extend it over more months to develop a more comprehensive understanding of particle dispersion processes at global scales. Additionally, the sensitivity of Lagrangian statistics to high-frequency motions and internal gravity waves should be further investigated. An appealing approach that we are currently undertaking is through a toy model based on kinematic flows (see, e.g., [122]) coupled with synthetic wave fields.

Conclusions

In this work, we presented a comprehensive study on Lagrangian particle dispersion in surface ocean turbulence, using numerical simulations of the SQG⁺¹ model and LLC4320 data. We address the question of how ageostrophic motions affect Lagrangian transport in ocean submesoscales by progressively increasing complexity. We begin with an idealized framework, the SQG⁺¹ model, where we vary the Rossby number to investigate the impact of ageostrophic motions on both Eulerian flow properties and Lagrangian statistics. Next, we compare the Lagrangian statistics for tracers advected by the full flow, including both geostrophic and ageostrophic components, and by the geostrophic component alone in the SQG⁺¹ model. This is motivated by the fact that velocity fields obtained via satellite altimetry (including those from SWOT) essentially represent the geostrophic part of the flow. Finally, since the SQG⁺¹ model does not account for high-frequency motions (as IGWs), we use Lagrangian tracers advected by LLC4320 surface velocity fields to assess the significance of IGWs on particle dispersion.

In Part III, we presented the results of this study across three chapters. In the first (Chapter 4), we have shown that the SQG⁺¹ model, in an oceanographic setup, can account for both the Eulerian and Lagrangian properties that characterize ocean submesoscales. We recover kinetic energy spectra with a scaling close to $E(k) \sim k^{-2}$, a behavior consistent with submesoscales and in reasonable agreement with observations [25, 109, 112]. Additionally, we find that its dynamics are characterized by a dominance of cyclones over anticyclones. The intensity of this increases with the Rossby number. Using relative dispersion, kurtosis, and the FSLE, we found that pair-dispersion properties are only marginally affected by Ro and that dispersion is nonlocal in our simulations. However, clustering,

driven by ageostrophic motions, intensifies with Ro , as observed through the computation of the PDF of Voronoï cell areas and the correlation dimension.

In the second chapter (Chapter 5), we adopt again the SQG⁺¹ to explore the accuracy of velocity fields similar to those from satellites like SWOT. We address this by comparing trajectories of particles advected by either the full flow or its geostrophic part only, which should be closer to that measured by satellite altimetry. The results are in agreement with those obtained by comparing particle advection in weakly-ageostrophic-flow simulations at different Rossby numbers in Chapter 4, highlighting the weak effect of ageostrophic velocity on the pair separation process. However, they also reveal that advection by the geostrophic-only flow tends to overestimate the typical pair-separation rate. Moreover, we show that filtering the ageostrophic flow causes a bias on trajectories, whose importance grows with Ro , and we quantify the scale-by-scale dispersion rate between the full and geostrophic-only advection models. We further characterize the temporary particle clusters that form due to ageostrophic motions. In particular, we find that, while compressibility is small in our simulations, the intensity of clustering can be substantial. Our analysis indicates that, in the SQG⁺¹ system, clustering is essentially due to the interplay between the (small) flow compressibility and the existence of long-lived structures that trap particles, increasing their accumulation.

Finally, in the last chapter (Chapter 6), we shift our analysis from an idealized model to a high-resolution general circulation model (LLC4320). Our study focuses on a specific area in the Kuroshio Extension during February and August 2012. This region is particularly interesting because it exhibits energetic submesoscales and is a SWOT crossover region. We begin by examining the dispersion process using single-particle and two-particle statistics. To understand what drives the dispersion process, we analyze the Eulerian flow properties in that region by partitioning motions into slower mesoscale/submesoscale motions and faster IGWs. We find that, in February, dispersion is local and driven by mesoscale/submesoscale motions. This is consistent with previous studies showing that submesoscale motions are intensified in winter [13, 113]. However, in August, dispersion is more likely nonlocal but still driven by mesoscale/submesoscale motions with a steep kinetic energy spectrum,

$E(k) \sim k^{-3}$. Despite the increased intensity of IGWs contributing to the full kinetic energy of the flow (i.e., associated with both slower and faster processes) in August, the dispersion statistics showed no significant sensitivity to IGWs, particularly since the inertial oscillation scale is close to the smallest scale studied (not far from the grid resolution of LLC4320). Finally, we approximated the kinetic energy spectrum from SSH. We found that, in winter, the geostrophic approximation performs reasonably well, though with a slight overestimation of energy and potential overestimation of the pair-separation rate. In summer, as IGWs are intensified, both the dispersion relation of waves and the geostrophic approximation are necessary to achieve a reliable approximation of the kinetic energy spectrum from SSH.

In conclusion, we demonstrate that the SQG⁺¹ model is well suited for modeling ocean submesoscales, as its dynamics exhibit key submesoscale features. The model generates a flow with cyclone-anticyclone asymmetry and divergent horizontal motion. We find that dispersion is driven by large-scale structures in these simulations and is only weakly influenced by ageostrophic motions. Additionally, clustering is attributed to ageostrophic motions and predominantly occurs in cyclonic frontal regions, consistent with drifter observations [18]. Furthermore, after filtering SQG⁺¹ flows and advecting particles, we observe that this filtering results in an increased pair-separation rate compared to particles advected by the full flow. Importantly, filtering out ageostrophic motions eliminates clustering, suggesting caution is needed when using SWOT-derived velocity fields for Lagrangian applications. This clustering is further intensified by the flow's time correlation and persistent strain. Lastly, when considering a general ocean circulation model, we observe a seasonal variability effect: during winter, dispersion is local, whereas in summer, it becomes nonlocal. In both cases, dispersion is driven by mesoscale/submesoscale motions, specifically the rotational flow component (i.e., vorticity).

For future perspectives, we find two possible directions interesting to explore. The first incorporates internal wave dynamics into the QG, or even the SQG⁺¹, model. By integrating IGWs into these models, we could investigate the effects of IGWs within the framework of models that extend the QG approximation. This enhancement would allow us to study the interactions between

IGWs and submesoscale processes more comprehensively. It would also facilitate decoupling their impact from slower ageostrophic motions, enabling a clearer understanding of the respective roles of different dynamical processes in ocean circulation. Such an approach could lead to improved Lagrangian transport and dispersion modeling at submesoscales, providing more accurate predictions crucial for applications like pollutant tracking, search and rescue operations, and understanding nutrient transport in marine ecosystems. The second perspective involves studying more SWOT crossover regions to gain a more global understanding of the dispersion process. By expanding our analysis to multiple SWOT crossover points across different oceanic regions, we can examine clustering and dispersion within a global-scale framework. This broader approach would help identify regional variations and commonalities in submesoscale dynamics, enhancing the generality and applicability of our findings. Additionally, it would contribute to validating and refining our models using high-resolution satellite data, improving their accuracy and reliability. Exploring these additional regions would allow us to capture a wider range of oceanic conditions and processes, thereby enriching our understanding of Lagrangian transport and improving our ability to predict and manage oceanic phenomena on a global scale.

Bibliography

- [1] Annalisa Bracco, Claire B. Paris, Andrew J. Esbaugh, Kaitlin Frasier, Samantha B. Joye, Guangpeng Liu, Kurt L. Polzin, and Ana Carolina Vaz. “Transport, Fate and Impacts of the Deep Plume of Petroleum Hydrocarbons Formed During the Macondo Blowout”. In: *Front. Mar. Sci.* 7 (2020). doi: <https://doi.org/10.3389/fmars.2020.542147>.
- [2] Benjamin A. Storer, Michele Buzzicotti, Hemant Khatri, Stephen M. Griffies, and Hussein Aluie. “Global energy spectrum of the general oceanic circulation”. In: *Nat. Commun.* 13 (2022), p. 5314. doi: <https://doi.org/10.1038/s41467-022-33031-3>.
- [3] J. C. McWilliams. “Submesoscale currents in the ocean”. In: *Proc. R. Soc. A* 472 (2016), p. 20160117. doi: <https://doi.org/10.1098/rspa.2016.0117>.
- [4] C.W Hughes and S.A Carnochan. “Rossby wave propagation from satellite altimetry”. In: *Adv. Space Res.* 22.11 (1998), pp. 1557–1560. doi: [https://doi.org/10.1016/S0273-1177\(99\)00067-8](https://doi.org/10.1016/S0273-1177(99)00067-8).
- [5] G. K. Vallis. *Atmospheric and Oceanic Fluid Dynamics*. Cambridge University Press, New York, USA, 2017. doi: <https://doi.org/10.1017/9781107588417>.
- [6] Raffaele Ferrari and Carl Wunsch. “Ocean Circulation Kinetic Energy: Reservoirs, Sources, and Sinks”. In: *Annu. Rev. Fluid Mech.* 41. Volume 41, 2009 (2009), pp. 253–282. doi: <https://doi.org/10.1146/annurev.fluid.40.111406.102139>.
- [7] Dudley B. Chelton, Michael G. Schlax, and Roger M. Samelson. “Global observations of nonlinear mesoscale eddies”. In: *Prog. Oceanogr.* 91.2 (2011), pp. 167–216. doi: <https://doi.org/10.1016/j.pocean.2011.01.002>.

- [8] Patrice Klein, Guillaume Lapeyre, Lia Siegelman, Bo Qiu, Lee-Lueng Fu, Hector Torres, Zhan Su, Dimitris Menemenlis, and Sylvie Le Gentil. “Ocean-Scale Interactions From Space”. In: *Earth Space Sci.* 6.5 (2019), pp. 795–817. doi: <https://doi.org/10.1029/2018EA000492>.
- [9] Hyodae Seo, Larry W. O’Neill, Mark A. Bourassa, Arnaud Czaja, Kyla Drushka, James B. Edson, Baylor Fox-Kemper, Ivy Frenger, Sarah T. Gille, Benjamin P. Kirtman, Shoshiro Minobe, Angeline G. Pendergrass, Lionel Renault, Malcolm J. Roberts, Niklas Schneider, R. Justin Small, Ad Stoffelen, and Qing Wang. “Ocean Mesoscale and Frontal-Scale Ocean–Atmosphere Interactions and Influence on Large-Scale Climate: A Review”. In: *J. Climate* 36.7 (2023), pp. 1981–2013. doi: [10.1175/JCLI-D-21-0982.1](https://doi.org/10.1175/JCLI-D-21-0982.1).
- [10] Z. Zhang, B. Qiu, P. Klein, and S. Travis. “The influence of geostrophic strain on oceanic ageostrophic motion and surface chlorophyll”. In: *Nat. Commun.* 10 (2019), p. 2838. doi: <https://doi.org/10.1038/s41467-019-10883-w>.
- [11] A. Mahadevan and A. Tandon. “An analysis of mechanisms for submesoscale vertical motion at ocean fronts”. In: *Ocean Model.* 14 (2006), pp. 241–256. doi: <https://doi.org/10.1016/j.ocemod.2006.05.006>.
- [12] M. Lévy, P.J.S. Franks, and K.S. Smith. “The role of submesoscale currents in structuring marine ecosystems”. In: *Nat. Commun.* 9 (2018), p. 4758. doi: <https://doi.org/10.1038/s41467-018-07059-3>.
- [13] Z. Su, J. B. Wang, P. Klein, A. F. Thompson, and D. Menemenlis. “Ocean submesoscales as a key component of the global heat budget”. In: *Nat. Commun.* 9 (2018), p. 775. doi: <https://doi.org/10.1038/s41467-018-02983-w>.
- [14] K. Gallmeier, J. X. Prochaska, P. Cornillon, D. Menemenlis, and M. Kelm. “An evaluation of the LLC4320 global-ocean simulation based on the submesoscale structure of modeled sea surface temperature fields”. In: *Geosci. Model Dev.* 16.23 (2023), pp. 7143–7170. doi: <https://doi.org/10.5194/gmd-16-7143-2023>.
- [15] Jakob Gawlikowski, Patrick Ebel, Michael Schmitt, and Xiao Xiang Zhu. “Explaining the Effects of Clouds on Remote Sensing Scene Classification”. In: *IEEE J. Sel. Top. Appl. Earth Obs. Remote Sens.* 15 (2022), pp. 9976–9986. doi: <https://doi.org/10.1109/JSTARS.2022.3221788>.

- [16] L.-L. Fu, T. Pavelsky, J.-F. Cretaux, R. Morrow, J. T. Farrar, P. Vaze, P. Sengenès, N. Vinogradova-Shiffer, A. Sylvestre-Baron, N. Picot, and G. Dibarboure. “The Surface Water and Ocean Topography Mission: A breakthrough in radar remote sensing of the ocean and land surface water”. In: *Geophys. Res. Lett.* 51.4 (2024), e2023GL107652. doi: <https://doi.org/10.1029/2023GL107652>.
- [17] J. H. LaCasce. “Statistics from Lagrangian observations”. In: *Prog. Oceanogr.* 77 (2008), pp. 1–29. doi: <https://doi.org/10.1016/j.pocean.2008.02.002>.
- [18] E. A. D’Asaro, A. Y. Shcherbina, J. M. Klymak, J. Molemaker, G. Novelli, C. M. Guigand, A. C. Haza, B. K. Haus, E. H. Ryan, G. A. Jacobs, H. S. Huntley, N. J. M. Laxague, S. Chen, F. Judt, J. C. McWilliams, R. Barkan, A. D. Kirwan Jr., A. C. Poje, and T. M. Özgökmen. “Ocean convergence and the dispersion of flotsam”. In: *Proc. Natl. Acad. Sci. U. S. A.* 115 (2018), pp. 1162–1167. doi: <https://doi.org/10.1073/pnas.1718453115>.
- [19] Helga S. Huntley, B. L. Lipphardt Jr., Gregg Jacobs, and A. D. Kirwan Jr. “Clusters, deformation, and dilation: Diagnostics for material accumulation regions”. In: *J. Geophys. Res.* 120.10 (2015), pp. 6622–6636. doi: <https://doi.org/10.1002/2015JC011036>.
- [20] G. A. Jacobs, H. S. Huntley, A. D. Kirwan Jr., B. L. Lipphardt Jr., T. Campbell, T. Smith, K. Edwards, and B. Bartels. “Ocean processes underlying surface clustering”. In: *J. Geophys. Res.* 121 (2016), pp. 180–197. doi: <https://doi.org/10.1002/2015JC011140>.
- [21] M. Berta, A. Griffa, A. C. Haza, J. Horstmann, H. S. Huntley, R. Ibrahim, B. Lund, T. M. Özgökmen, and A. C. Poje. “Submesoscale kinematic properties in summer and winter surface flows in the Northern Gulf of Mexico”. In: *J. Geophys. Res.* 125 (2020), e2020JC016085. doi: <https://doi.org/10.1029/2020JC016085>.
- [22] D. L. Rudnick. “On the skewness of vorticity in the upper ocean”. In: *Geophys. Res. Lett.* 28 (2001), p. 2045. doi: <https://doi.org/10.1029/2000GL012265>.
- [23] G. Rouillet and P. Klein. “Cyclone-anticyclone asymmetry in geophysical turbulence”. In: *Phys. Rev. Lett.* 104 (2010), p. 218501. doi: <https://doi.org/10.1103/PhysRevLett.104.218501>.
- [24] A. Y. Shcherbina, E. A. D’Asaro, C. M. Lee, J. M. Klymak, M. J. Molemaker, and J. C. McWilliams. “Statistics of vertical vorticity, divergence, and strain in a developed submesoscale turbulence field”. In: *Geophys. Res. Lett.* 40 (2013), p. 4706. doi: <https://doi.org/10.1002/grl.50919>.

- [25] Guillaume Lapeyre. “Surface Quasi-Geostrophy”. In: *Fluids* 2.1 (2017). doi: <https://doi.org/10.3390/fluids2010007>.
- [26] A. C. Poje, T. M. Özgökmen, B. L. Lipphardt Jr., B. K. Haus, E. H. Ryan, A. C. Haza, G. A. Jacobs, A. J. H. M. Reniers, M. J. Olascoaga, G. Novelli, A. Griffa, F. J. Beron-Vera, S. S. Chen, E. Coelho, P. J. Hogan, A. D. Kirwan Jr., H. S. Huntley, and A. J. Mariano. “Submesoscale dispersion in the vicinity of the Deepwater Horizon Spill”. In: *Proc. Natl. Acad. Sci. U. S. A.* 111 (2014), pp. 12693–12698. doi: <https://doi.org/10.1073/pnas.1402452111>.
- [27] S. Berti, F. Dos Santos, G. Lacorata, and A. Vulpiani. “Lagrangian drifter dispersion in the Southwestern Atlantic ocean”. In: *J. Phys. Oceanogr.* 41 (2011), pp. 1659–1672. doi: <https://doi.org/10.1175/2011JP04541.1>.
- [28] James C. McWilliams. “A survey of submesoscale currents”. In: *Geosci. Lett.* 6.1 (2019), p. 3. doi: <https://doi.org/10.1186/s40562-019-0133-3>.
- [29] Andrei Nikolaevich Kolmogorov, V. Levin, Julian Charles Roland Hunt, Owen Martin Phillips, and David Williams. “The local structure of turbulence in incompressible viscous fluid for very large Reynolds numbers”. In: *Proc. R. Soc. Lond. A Math. Phys. Sci.* 434.1890 (1991), pp. 9–13. doi: <https://doi.org/10.1098/rspa.1991.0075>.
- [30] Uriel Frisch. *Turbulence: The Legacy of A. N. Kolmogorov*. Cambridge University Press, 1995. doi: <https://doi.org/10.1017/CB09781139170666>.
- [31] Jule G. Charney. “Geostrophic Turbulence”. In: *J. Atmos. Sci.* 28.6 (1971), pp. 1087–1095. doi: [https://doi.org/10.1175/1520-0469\(1971\)028<1087:GT>2.0.CO;2](https://doi.org/10.1175/1520-0469(1971)028<1087:GT>2.0.CO;2).
- [32] Guido Boffetta and Robert E. Ecke. “Two-Dimensional Turbulence”. In: *Annu. Rev. Fluid Mech.* 44. Volume 44, 2012 (2012), pp. 427–451. doi: <https://doi.org/10.1146/annurev-fluid-120710-101240>.
- [33] G. K. Batchelor. “Computation of the Energy Spectrum in Homogeneous Two-Dimensional Turbulence”. In: *Phys. Fluids* 12.12 (1969), pp. II-233–II-239. doi: <https://doi.org/10.1063/1.1692443>.
- [34] Robert H. Kraichnan. “Inertial Ranges in Two-Dimensional Turbulence”. In: *Phys. Fluids* 10.7 (July 1967), pp. 1417–1423. doi: <https://doi.org/10.1063/1.1762301>.
- [35] Robert H. Kraichnan. “Inertial-range transfer in two- and three-dimensional turbulence”. In: *J. Fluid Mech.* 47.3 (1971), pp. 525–535. doi: <https://doi.org/10.1017/S0022112071001216>.

- [36] G. D. Nastrom and K. S. Gage. “A Climatology of Atmospheric Wavenumber Spectra of Wind and Temperature Observed by Commercial Aircraft”. In: *J. Atmos. Sci.* 42.9 (1985), pp. 950–960. DOI: [https://doi.org/10.1175/1520-0469\(1985\)042<0950:ACOWS>2.0.CO;2](https://doi.org/10.1175/1520-0469(1985)042<0950:ACOWS>2.0.CO;2).
- [37] D. K. Lilly and E. L. Petersen. “Aircraft measurements of atmospheric kinetic energy spectra”. In: *Tellus A* 35.5 (1983), pp. 379–382. DOI: <https://doi.org/10.3402/tellusa.v35i5.11448>.
- [38] Erik Lindborg. “Can the atmospheric kinetic energy spectrum be explained by two-dimensional turbulence?” In: *J. Fluid Mech.* 388 (1999), pp. 259–288. DOI: <https://doi.org/10.1017/S0022112099004851>.
- [39] J. G. Charney, Bruce Gilchrist, and F. G. Shuman. “THE PREDICTION OF GENERAL QUASI-GEOSTROPHIC MOTIONS”. In: *J. Atmos. Sci.* 13.5 (1956), pp. 489–499. DOI: [https://doi.org/10.1175/1520-0469\(1956\)013<0489:TPOGQG>2.0.CO;2](https://doi.org/10.1175/1520-0469(1956)013<0489:TPOGQG>2.0.CO;2).
- [40] James C. McWilliams. “Statistical properties of decaying geostrophic turbulence”. In: *J. Fluid Mech.* 198 (1989), pp. 199–230. DOI: <https://doi.org/10.1017/S0022112089000108>.
- [41] Isaac M. Held, Raymond T. Pierrehumbert, Stephen T. Garner, and Kyle L. Swanson. “Surface quasi-geostrophic dynamics”. In: *J. Fluid Mech.* 282 (1995), pp. 1–20. DOI: <https://doi.org/10.1017/S0022112095000012>.
- [42] K. S. Smith, G. Boffetta, C. C. Henning, I. N. Marinov, C. Y. Tam, I. M. Held, and G. K. Vallis. “Turbulent diffusion in the geostrophic inverse cascade”. In: *J. Fluid Mech.* 469 (2002), pp. 14–47. DOI: <https://doi.org/10.1017/S0022112002001763>.
- [43] X. Capet, P. Klein, B. L. Hua, G. Lapeyre, and J. C. McWilliams. “Surface kinetic and potential energy transfer in SQG dynamics”. In: *J. Fluid Mech.* 604 (2008), pp. 165–174. DOI: <https://doi.org/10.1017/S0022112008001110>.
- [44] C. Perruche, P. Rivière, G. Lapeyre, X. Carton, and P. Pondaven. “Effects of Surface Quasi-Geostrophic turbulence on phytoplankton competition and coexistence”. In: *J. Mar. Res.* 69 (2011), pp. 105–135. DOI: https://elischolar.library.yale.edu/journal_of_marine_research/297.
- [45] D. J. Muraki, C. Snyder, and R. Rotunno. “The next-order corrections to quasigeostrophic theory”. In: *J. Atmos. Sci.* 56 (1999), p. 1547. DOI: [https://doi.org/10.1175/1520-0469\(1999\)056%3C1547:TNOCTQ%3E2.0.CO;2](https://doi.org/10.1175/1520-0469(1999)056%3C1547:TNOCTQ%3E2.0.CO;2).

- [46] J. B. Weiss. “Point-vortex dynamics in three-dimensional ageostrophic balanced flows”. In: *J. Fluid Mech.* 936 (2022), A19. doi: <https://doi.org/10.1017/jfm.2022.55>.
- [47] G. J. Hakim, C. Snyder, and D. J. Muraki. “A new surface model for cyclone–anticyclone asymmetry”. In: *J. Atmos. Sci.* 59 (2002), p. 2405. doi: [https://doi.org/10.1175/1520-0469\(2002\)059%3C2405:ANSMFC%3E2.0.CO;2](https://doi.org/10.1175/1520-0469(2002)059%3C2405:ANSMFC%3E2.0.CO;2).
- [48] Francesco Ragone and Gualtiero Badin. “A study of surface semi-geostrophic turbulence: freely decaying dynamics”. In: *J. Fluid Mech.* 792 (2016), pp. 740–774. doi: <https://doi.org/10.1017/jfm.2016.116>.
- [49] X. Yu, A. L. Ponte, S. Elipot, D. Menemenlis, E. D. Zaron, and R. Abernathey. “Surface kinetic energy distributions in the global oceans from a high-resolution numerical model and surface drifter observations”. In: *Geophys. Res. Lett.* 46 (2019), pp. 9757–9766. doi: <https://doi.org/10.1029/2019GL083074>.
- [50] H. Wang, N. Grisouard, H. Salehipour, A. Nuz, M. Poon, and A. L. Ponte. “A deep learning approach to extract internal tides scattered by geostrophic turbulence”. In: *Geophys. Res. Lett.* 49 (2022), e2022GL099400. doi: <https://doi.org/10.1029/2022GL099400>.
- [51] B. K. Arbic, S. Elipot, J. M. Brasch, D. Menemenlis, A. L. Ponte, J. F. Shriver, X. Yu, E. D. Zaron, M. H. Alford, M. C. Buijsman, R. Abernathey, D. Garcia, L. Guan, P. E. Martin, and A. D. Nelson. “Near-surface oceanic kinetic energy distributions from drifter observations and numerical models”. In: *J. Geophys. Res.* 127 (2022), e2022JC018551. doi: <https://doi.org/10.1029/2022JC018551>.
- [52] A. Foussard, S. Berti, X. Perrot, and G. Lapeyre. “Relative dispersion in generalized two-dimensional turbulence”. In: *J. Fluid Mech.* 821 (2017), pp. 358–383. doi: <https://doi.org/10.1017/jfm.2017.253>.
- [53] Lewis Fry Richardson and Gilbert Thomas Walker. “Atmospheric diffusion shown on a distance-neighbour graph”. In: *Proc. R. Soc. Lond. A* 110.756 (1926), pp. 709–737. doi: <https://doi.org/10.1098/rspa.1926.0043>.
- [54] AM Obukhov. “On the energy distribution in the spectrum of a turbulent flow”. In: *Dokl. Akad. Nauk SSSR*. Vol. 32. 1941, pp. 19–21.
- [55] G. Boffetta and I. M. Sokolov. “Relative Dispersion in Fully Developed Turbulence: The Richardson’s Law and Intermittency Corrections”. In: *Phys. Rev. Lett.* 88 (9 2002), p. 094501. doi: <https://doi.org/10.1103/PhysRevLett.88.094501>.

- [56] M. Bourgoïn, N. T. Ouellette, H. Xu, J. Berg, and E. Bodenschatz. “The role of pair dispersion in turbulent flow”. In: *Science* 311 (2006), pp. 835–838. DOI: <https://doi.org/10.1126/science.1121726>.
- [57] G. K. Batchelor. “The application of the similarity theory of turbulence to atmospheric diffusion”. In: *Q. J. R. Meteorol. Soc.* 551 (1950), pp. 133–146. DOI: <https://doi.org/10.1002/qj.49707632804>.
- [58] M. Cencini, F. Cecconi, and A. Vulpiani. *Chaos: from simple models to complex systems*. World Scientific, Singapore, 2010. DOI: <https://doi.org/10.1142/7351>.
- [59] M. Cencini and A. Vulpiani. “Finite size Lyapunov exponent: review on applications”. In: *J. Phys. A: Math. Theor.* 46 (2013), p. 254019. DOI: <https://doi.org/10.1088/1751-8113/46/25/254019>.
- [60] V. Artale, G. Boffetta, A. Celani, M. Cencini, and A. Vulpiani. “Dispersion of passive tracers in closed basins: beyond the diffusion coefficient”. In: *Phys. Fluids A* 9 (1997), pp. 3162–3171. DOI: <https://doi.org/10.1063/1.869433>.
- [61] S. Berti and G. Lapeyre. “Lagrangian reconstructions of temperature and velocities at submesoscales”. In: *Ocean Model.* 76 (2014), pp. 59–71. DOI: <https://doi.org/10.1016/j.ocemod.2014.02.003>.
- [62] S. Berti and G. Lapeyre. “Lagrangian pair dispersion in upper-ocean turbulence in the presence of mixed-layer instabilities”. In: *Phys. Fluids* 33 (2021), p. 036603. DOI: <https://doi.org/10.1063/5.0041036>.
- [63] Jr. Patterson G. S. and Steven A. Orszag. “Spectral Calculations of Isotropic Turbulence: Efficient Removal of Aliasing Interactions”. In: *Phys. Fluids* 14.11 (Nov. 1971), pp. 2538–2541. DOI: <https://doi.org/10.1063/1.1693365>.
- [64] Stephen B. Pope. *Turbulent Flows*. Cambridge University Press, 2000. DOI: <https://doi.org/10.1017/CB09780511840531>.
- [65] B. L. Hua. “The conservation of potential vorticity along Lagrangian trajectories in simulations of eddy-driven flows”. In: *J. Phys. Oceanogr.* 24 (1994), pp. 498–508. DOI: [https://doi.org/10.1175/1520-0485\(1994\)024%3C0498:TCOPVA%3E2.0.CO;2](https://doi.org/10.1175/1520-0485(1994)024%3C0498:TCOPVA%3E2.0.CO;2).
- [66] N. Zouari and A. Babiano. “Expériences numériques lagrangiennes à partir de modèles eulériens”. In: *Atmos.–Ocean* 28 (1990), pp. 345–364. DOI: <https://doi.org/10.1080/07055900.1990.9649382>.

- [67] Michael Maalouly, Guillaume Lapeyre, Bastien Cozian, Gilmar Mompéan, and Stefano Berti. “Particle dispersion and clustering in surface ocean turbulence with ageostrophic dynamics”. In: *Phys. Fluids* 35.12 (2023), p. 126601. doi: <https://doi.org/10.1063/5.0174665>.
- [68] A. Celani, M. Cencini, A. Mazzino, and M. Vergassola. “Active and passive fields face to face”. In: *New J. Phys.* 6 (2004), p. 72. doi: <https://doi.org/10.1088/1367-2630/6/1/072>.
- [69] G. Lapeyre, P. Klein, and B. L. Hua. “Oceanic Restratification Forced by Surface Frontogenesis”. In: *J. Phys. Oceanogr.* 36 (2006), pp. 1577–1590. doi: <https://doi.org/10.1175/JP02923.1>.
- [70] W. K. Dewar and G. R. Flierl. “Some effects of the wind on rings”. In: *J. Phys. Oceanogr.* 17 (1987), pp. 1653–1667. doi: [https://doi.org/10.1175/1520-0485\(1987\)017%3C1653:SEOTW0%3E2.0.CO;2](https://doi.org/10.1175/1520-0485(1987)017%3C1653:SEOTW0%3E2.0.CO;2).
- [71] L. Zavala Sansón, I.M. García-Martínez, and J. Sheinbaum. “Nonlinear surface Ekman effects on cyclonic and anticyclonic vortices”. In: *J. Fluid Mech.* 971 (2023), A35. doi: <https://doi.org/10.1017/jfm.2023.688>.
- [72] G. J. Hakim and A. K. Canavan. “Observed Cyclone–Anticyclone Tropopause Vortex Asymmetries”. In: *J. Atmos Sci.* 62 (2005), pp. 231–240. doi: <https://doi.org/10.1175/JAS-3353.1>.
- [73] J. H. LaCasce. “Relative displacement probability distribution functions from balloons and drifters”. In: *J. Mar. Res.* 68 (2010), pp. 433–457. doi: https://elischolar.library.yale.edu/journal_of_marine_research/274.
- [74] J. H. LaCasce and Thomas Meunier. “Relative dispersion with finite inertial ranges”. In: *J. Fluid Mech.* 932 (2022), A39. doi: <https://doi.org/10.1017/jfm.2021.1050>.
- [75] F. J. Beron-Vera and J. H. LaCasce. “Statistics of simulated and observed pair separations in the Gulf of Mexico”. In: *J. Fluid Mech.* 46 (2016), pp. 2183–2199. doi: <https://doi.org/10.1175/JPO-D-15-0127.1>.
- [76] L. Z. Sansón, P. Pérez-Brunius, and J. Sheinbaum. “Surface relative dispersion in the Southwestern Gulf of Mexico”. In: *J. Phys. Oceanogr.* 47 (2017), pp. 387–403. doi: <https://doi.org/10.1175/JPO-D-16-0105.1>.
- [77] A. Dhanagare, S. Musacchio, and D. Vincenzi. “Weak-strong clustering transition in renewing compressible flows”. In: *J. Fluid Mech.* 761 (2014), pp. 431–442. doi: <https://doi.org/10.1017/jfm.2014.634>.

- [78] G. Boffetta, J. Davoudi, Bruno B. Eckhardt, and J. Schumacher. “Lagrangian tracers on a surface flow: the role of time correlations”. In: *Phys. Rev. Lett.* 93 (2004), p. 134501. doi: <https://doi.org/10.1103/PhysRevLett.93.134501>.
- [79] R. Monchaux, M. Bourgoïn, and A. Cartellier. “Preferential concentration of heavy particles: a Voronoï analysis”. In: *Phys. Fluids* 22 (2010), p. 103304. doi: <https://doi.org/10.1063/1.3489987>.
- [80] Y. Tagawa, J. M. Mercado, V. N. Prakash, E. Calzavarini, C. Sun, and D. Lohse. “Three-dimensional Lagrangian Voronoï analysis for clustering of particles and bubbles in turbulence”. In: *J. Fluid Mech.* 693 (2012), pp. 201–215. doi: <https://doi.org/10.1017/jfm.2011.510>.
- [81] A. Okabe, B. Boots, K. Sugihara, and S. N. Chiu. *Spatial tessellations*. Wiley, New York, USA, 2000. ISBN: 978-0-471-98635-5. URL: <https://www.wiley.com/en-us/Spatial+Tessellations%3A+Concepts+and+Applications+of+Voronoi+Diagrams%2C+2nd+Edition-p-9780471986355>.
- [82] J.-S. Ferenc and Z. Néda. “On the size distribution of Poisson Voronoï cells”. In: *Physica A* 385 (2007), pp. 518–526. doi: <https://doi.org/10.1016/j.physa.2007.07.063>.
- [83] D. Elhmaïdi, A. Provenzale, and A. Babiano. “Elementary topology of two-dimensional turbulence from a Lagrangian viewpoint and single-particle dispersion”. In: *J. Fluid Mech.* 257 (1993), pp. 533–558. doi: <https://doi.org/10.1017/S0022112093003192>.
- [84] P. Grassberger and I. Procaccia. “Characterization of Strange Attractors”. In: *Phys. Rev. Lett.* 50 (1983), pp. 346–349. doi: <https://doi.org/10.1103/PhysRevLett.50.346>.
- [85] A. Okubo. “Horizontal dispersion of floatable particles in the vicinity of velocity singularities such as convergences”. In: *Deep-Sea Res.* 17 (1970), pp. 445–454. doi: [https://doi.org/10.1016/0011-7471\(70\)90059-8](https://doi.org/10.1016/0011-7471(70)90059-8).
- [86] J. Weiss. “The dynamics of enstrophy transfer in two-dimensional hydrodynamics”. In: *Physica D* 48 (1991), pp. 273–294. doi: [https://doi.org/10.1016/0167-2789\(91\)90088-Q](https://doi.org/10.1016/0167-2789(91)90088-Q).
- [87] G. Lapeyre, B. L. Hua, and P. Klein. “Dynamics of orientation of gradients of active and passive scalars in two-dimensional turbulence”. In: *Phys. Fluids A* 13 (2001), pp. 251–264. doi: <https://doi.org/10.1063/1.1324705>.

- [88] P. Klein, B. L. Hua, and G. Lapeyre. “Alignment of tracer gradient vectors in 2D turbulence”. In: *Physical D* 146 (2000), pp. 246–260. doi: [https://doi.org/10.1016/S0167-2789\(00\)00119-6](https://doi.org/10.1016/S0167-2789(00)00119-6).
- [89] G. Lapeyre, P. Klein, and B. L. Hua. “Does the tracer gradient vector align with the strain eigenvectors in 2-D turbulence?” In: *Phys. Fluids A* 11 (1999), pp. 3729–3737. doi: <https://doi.org/10.1063/1.870234>.
- [90] D. Balwada, Q. Xiao, S. Smith, R. Abernathey, and A. R. Gray. “Vertical fluxes conditioned on vorticity and strain reveal submesoscale ventilation”. In: *J. Phys. Oceanogr.* 51 (2021), pp. 2883–2901. doi: <https://doi.org/10.1175/JPO-D-21-0016.1>.
- [91] L. Wang, J. Gula, J. Collin, and L. Mémerly. “Effects of mesoscale dynamics on the path of fast-sinking particles to the deep ocean: a modeling study”. In: *J. Geophys. Res.* 127 (2022), e2022JC018799. doi: <https://doi.org/10.1029/2022JC018799>.
- [92] C. Vic, S. Hascoët, J. Gula, T. Huck, and C. Maes. “Oceanic mesoscale cyclones cluster surface Lagrangian material”. In: *Geophys. Res. Lett.* 49 (2022), e2021GL097488. doi: <https://doi.org/10.1029/2021GL097488>.
- [93] P. Klein, B. L. Hua, G. Lapeyre, X. Capet, S. LeGentil, and H. Sasaki. “Upper ocean turbulence from high-resolution 3D simulations”. In: *J. Phys. Oceanogr.* 38 (2008), pp. 1748–1763. doi: <https://doi.org/10.1175/2007JP03773.1>.
- [94] X. Capet, J. C. McWilliams, M. Molemaker, and A. Shchepetkin. “Mesoscale to submesoscale transition in the California current system. Part I: flow structure, eddy flux and observational tests”. In: *J. Phys. Oceanogr.* 38 (2008), pp. 29–43. doi: <https://doi.org/10.1175/2007JP03671.1>.
- [95] D. Balwada, K. S. Smith, and R. Abernathey. “Submesoscale vertical velocities enhance tracer subduction in an idealized Antarctic Circumpolar Current”. In: *Geophys. Res. Lett.* 45 (2018), pp. 9790–9802. doi: <https://doi.org/10.1029/2018GL079244>.
- [96] Victor Onink, David Wichmann, Philippe Delandmeter, and Erik van Sebille. “The Role of Ekman Currents, Geostrophy, and Stokes Drift in the Accumulation of Floating Microplastic”. In: *J. Geophys. Res. Oceans* 124.3 (2019), pp. 1474–1490. doi: <https://doi.org/10.1029/2018JC014547>.
- [97] F. J. Beron-Vera, M. J. Ollascoaga, and P. Miron. “Building a Maxey-Riley framework for surface ocean inertial particle dynamics”. In: *Phys. Fluids* 31 (2019), p. 096602. doi: <https://doi.org/10.1063/1.5110731>.

- [98] R. Morrow, L.-L. Fu, F. Ardhuin, M. Benkiran, B. Chapron, E. Cosme, F. d'Ovidio, J. T. Farrar, S. T. Gille, G. Lapeyre, P.-Y. Le Traon, A. Pascual, A. Ponte, B. Qiu, N. Raschle, C. Ubelmann, J. Wang, and E. D. Zaron. "Global observations of fine-scale ocean surface topography with the surface water and ocean topography (SWOT) mission". In: *Front. Mar. Sci.* 6 (2019), p. 232. doi: <https://doi.org/10.3389/fmars.2019.00232>.
- [99] Michael Maalouly, Guillaume Lapeyre, and Stefano Berti. "Impact of ageostrophic dynamics on the predictability of Lagrangian trajectories in surface-ocean turbulence". In: *Phys. Rev. Fluids* 9 (2024), p. 104503. doi: <https://doi.org/10.1103/PhysRevFluids.9.104503>.
- [100] G. Boffetta, A. Celani, G. Lacorata, and A. Vulpiani. "The predictability problem in systems with an uncertainty in the evolution law". In: *J. Phys. A: Math. Gen.* 33 (2000), pp. 1313–1324. doi: <https://doi.org/10.1088/0305-4470/33/7/302>.
- [101] G. Lacorata, R. Corrado, F. Falcini, and R. Santoleri. "FSLE analysis and validation of Lagrangian simulations based on satellite-derived GlobCurrent velocity data". In: *Remote Sens. Environ.* 221 (2019), pp. 136–143. doi: <https://doi.org/10.1016/j.rse.2018.11.013>.
- [102] G. Lapeyre. "Characterization of finite-time Lyapunov exponents and vectors in two-dimensional turbulence". In: *Chaos* 12 (2002), pp. 688–698. doi: <https://doi.org/10.1063/1.1499395>.
- [103] G. Benettin, L. Galgani, A. Giorgilli, and J.-M. Strelcyn. "Lyapunov characteristic exponents for smooth dynamical systems and for Hamiltonian systems; a method for computing all of them. Part 1: Theory". In: *Meccanica* 15 (1980), pp. 9–20. doi: <https://doi.org/10.1007/BF02128236>.
- [104] J. R. Cressman, J. Davoudi, W. I. Goldburg, and J. Schumacher. "Eulerian and Lagrangian studies in surface flow turbulence". In: *New J. Phys.* 6 (2004), p. 53. doi: <https://doi.org/10.1088/1367-2630/6/1/053>.
- [105] A. Pumir. "Structure of the velocity gradient tensor in turbulent shear flows". In: *Phys. Rev. Fluids* 2 (2017), p. 074602. doi: <https://doi.org/10.1103/PhysRevFluids.2.074602>.
- [106] P.-F. Yang, J. Fang, L. Fang, A. Pumir, and H. Xu. "Low-order moments of the velocity gradient in homogeneous compressible turbulence". In: *J. Fluid Mech.* 947 (2022), R1. doi: <https://doi.org/10.1017/jfm.2022.622>.

- [107] A. Sinha, D. Balwada, N. Tarshish, and R Abernathey. “Modulation of lateral transport by submesoscale flows and inertia-gravity waves”. In: *J. Adv. Mod. Earth Syst.* 11 (2019), pp. 1039–1065. doi: <https://doi.org/10.1029/2018MS001508>.
- [108] R. Morrow, L.-L. Fu, M.-H. Rio, Richard R. Ray, P. Prandi, P.-Y. Le Traon, and J. Benveniste. “Ocean circulation from space”. In: *Surv. Geophys.* 44.5 (2023), pp. 1243–1286. doi: <https://doi.org/10.1007/s10712-023-09778-9>.
- [109] C. B. Rocha, T. K. Chereskin, S. T. Gille, and D. Menemenlis. “Mesoscale to submesoscale wavenumber spectra in Drake passage”. In: *J. Phys. Oceanogr.* 46 (2016), pp. 601–620. doi: <https://doi.org/10.1175/JPO-D-15-0087.1>.
- [110] Jinbo Wang, Lee-Lueng Fu, Bo Qiu, Dimitris Menemenlis, J. Thomas Farrar, Yi Chao, Andrew F. Thompson, and Mar M. Flexas. “An Observing System Simulation Experiment for the Calibration and Validation of the Surface Water Ocean Topography Sea Surface Height Measurement Using In Situ Platforms”. In: *J. Atmos. Oceanic Technol.* 35.2 (2018), pp. 281–297. doi: <https://doi.org/10.1175/JTECH-D-17-0076.1>.
- [111] Anna C. Savage, Brian K. Arbic, Matthew H. Alford, Joseph K. Ansong, J. Thomas Farrar, Dimitris Menemenlis, Amanda K. O’Rourke, James G. Richman, Jay F. Shriver, Gunnar Voet, Alan J. Wallcraft, and Luis Zamudio. “Spectral decomposition of internal gravity wave sea surface height in global models”. In: *J. Geophys. Res. Oceans* 122.10 (2017), pp. 7803–7821. doi: <https://doi.org/10.1002/2017JC013009>.
- [112] Jörn Callies and Raffaele Ferrari. “Interpreting Energy and Tracer Spectra of Upper-Ocean Turbulence in the Submesoscale Range (1–200 km)”. In: *J. Phys. Oceanogr.* 43.11 (2013), pp. 2456–2474. doi: <https://doi.org/10.1175/JPO-D-13-063.1>.
- [113] Hector S. Torres, Patrice Klein, Dimitris Menemenlis, Bo Qiu, Zhan Su, Jinbo Wang, Shuiming Chen, and Lee-Lueng Fu. “Partitioning Ocean Motions Into Balanced Motions and Internal Gravity Waves: A Modeling Study in Anticipation of Future Space Missions”. In: *J. Geophys. Res. Oceans* 123.11 (2018), pp. 8084–8105. doi: <https://doi.org/10.1029/2018JC014438>.
- [114] Bruce R. Sutherland. *Internal Gravity Waves*. Cambridge University Press, 2010. doi: <https://doi.org/10.1017/CB09780511780318>.

- [115] Hector S. Torres, Patrice Klein, Eric D’Asaro, Jinbo Wang, Andrew F. Thompson, Lia Siegelman, Dimitris Menemenlis, Ernesto Rodriguez, Alexander Wineteer, and Dragana Perkovic-Martin. “Separating Energetic Internal Gravity Waves and Small-Scale Frontal Dynamics”. In: *Geophys. Res. Lett.* 49.6 (2022), e2021GL096249. doi: <https://doi.org/10.1029/2021GL096249>.
- [116] Oliver Bühler, Jörn Callies, and Raffaele Ferrari. “Wave–vortex decomposition of one-dimensional ship-track data”. In: *J. Fluid Mech.* 756 (2014), pp. 1007–1026. doi: <https://doi.org/10.1017/jfm.2014.488>.
- [117] P. Klein and G. Lapeyre. “The oceanic vertical pump induced by mesoscale and submesoscale turbulence”. In: *Annu. Rev. Mar. Sci.* 1 (2009), pp. 351–375. doi: <https://doi.org/10.1146/annurev.marine.010908.163704>.
- [118] John R. Taylor and Andrew F. Thompson. “Submesoscale Dynamics in the Upper Ocean”. In: *Annu. Rev. Fluid Mech.* 55. Volume 55, 2023 (2023), pp. 103–127. doi: <https://doi.org/10.1146/annurev-fluid-031422-095147>.
- [119] Bo Qiu, Shuiming Chen, Patrice Klein, Jinbo Wang, Hector Torres, Lee-Lueng Fu, and Dimitris Menemenlis. “Seasonality in Transition Scale from Balanced to Unbalanced Motions in the World Ocean”. In: *J. Phys. Oceanogr.* 48.3 (2018), pp. 591–605. doi: <https://doi.org/10.1175/JPO-D-17-0169.1>.
- [120] N. A. Maximenko and P. P. Niiler. “Mean Surface Circulation of the Global Ocean Inferred from Satellite Altimeter and Drifter Data”. In: *ESA Special Publication*. Vol. 614. July 2006, p. 113. URL: <https://ui.adsabs.harvard.edu/abs/2006ESASP.614E.113M>.
- [121] Peng Wang, Tamay M. Özgökmen, and Angelique C. Haza. “Material dispersion by oceanic internal waves”. In: *Environ. Fluid Mech.* 18.1 (2018), pp. 149–171. doi: <https://doi.org/10.1007/s10652-016-9491-y>.
- [122] Giovanni La Forgia, Davide Cavaliere, Stefania Espa, Federico Falcini, and Guglielmo Lacorata. “Numerical and experimental analysis of Lagrangian dispersion in two-dimensional chaotic flows”. In: *Sci. Rep.* 12.1 (2022), p. 7461. doi: <https://doi.org/10.1038/s41598-022-11350-1>.

Lyapunov exponents' spectrum

Lyapunov's theory of dynamical systems [58] can be applied to the evolution equation of Lagrangian tracer particles

$$\frac{d\mathbf{x}}{dt} = \mathbf{u}(\mathbf{x}(t), t). \quad (\text{A.1})$$

The linearized version of Eq. (A.1), in tangent space, is just

$$\frac{d\mathbf{w}}{dt} = [\nabla\mathbf{u}](\mathbf{x}(t), t) \mathbf{w}. \quad (\text{A.2})$$

The above equation is integrated along the Lagrangian path $\mathbf{x}(t)$; here $[\nabla\mathbf{u}](\mathbf{x}(t), t)$ is the velocity gradient tensor at position \mathbf{x} at time t . Equation (A.2) can be viewed as the equation for the separation $\delta\mathbf{x}$ between two (infinitesimally) close Lagrangian trajectories [102].

The Lyapunov spectrum is related to the asymptotic exponential growth rate of \mathbf{w} and is computed as follows [58, 103]. Given an arbitrary unitary initial vector $\mathbf{w}_1(t_0)$, the first exponent is computed as

$$\lambda_1 = \lim_{t \rightarrow \infty} \frac{1}{t - t_0} \ln \left(\frac{|\mathbf{w}_1(t)|}{|\mathbf{w}_1(t_0)|} \right), \quad (\text{A.3})$$

The second exponent is computed using a second vector $\mathbf{w}_2(t)$, initially unitary and orthogonal to the first one, evolving according to the same equation. The area $A(t)$ of the parallelogram defined by $\mathbf{w}_1(t)$ and $\mathbf{w}_2(t)$ at each time t allows to introduce Λ such that

$$\Lambda = \lim_{t \rightarrow \infty} \frac{1}{t - t_0} \ln \left[\frac{A(t)}{A(t_0)} \right]. \quad (\text{A.4})$$

Once Λ is known, λ_2 can be computed as

$$\lambda_2 = \Lambda - \lambda_1, \tag{A.5}$$

More details about the implementation of this method can be found in [58]. Note that using an ensemble of particles, we obtain values of λ_i ($i = 1, 2$) for each trajectory, which should be the same assuming ergodicity. In practice, λ_i values are further averaged over all trajectories.

Compressibility ratio

The compressibility ratio of Eq. (5.7), $\mathcal{C} = \langle (\nabla \cdot \mathbf{u})^2 \rangle / \langle (\nabla \mathbf{u})^2 \rangle$, accounts for the relative strength of divergence and strain. Considering that

$$(\nabla \mathbf{u})^2 = (\partial_x u)^2 + (\partial_x v)^2 + (\partial_y u)^2 + (\partial_y v)^2,$$

$$\Delta^2 \equiv (\nabla \cdot \mathbf{u})^2 = (\partial_x u)^2 + (\partial_y v)^2 + 2 \partial_x u \partial_y v,$$

$$\zeta^2 = (\partial_x v)^2 + (\partial_y u)^2 - 2 \partial_x v \partial_y u,$$

one has $\Delta^2 + \zeta^2 = (\nabla \mathbf{u})^2 + 2(\partial_x u \partial_y v - \partial_x v \partial_y u)$. Therefore, the compressibility ratio can also be written as

$$\mathcal{C} = \frac{\langle \Delta^2 \rangle}{\langle \Delta^2 \rangle + \langle \zeta^2 \rangle - 2 \left(\langle \partial_x u \partial_y v \rangle - \langle \partial_x v \partial_y u \rangle \right)}. \quad (\text{B.1})$$

To further simplify Eq. (B.1), one needs to estimate the correlations of velocity gradients appearing in the last parenthesis in the denominator. This problem was addressed in [106] in a broader context to characterize the low-order moments of velocity gradients of 3D compressible flows. Here, we recall some of the main points of the reasoning and adapt them to our 2D case. Specifically, we define $A_{ijkl}^{(2)} = \langle \partial_j u_i \partial_l u_k \rangle$, where clearly $i, j, k, l = 1, 2$ (indices 1 and 2 corresponding to the x and y directions, respectively) in 2D. As shown in [106], assuming statistical homogeneity ($\partial_i \langle \dots \rangle = 0$) one has

$$A_{ijji}^{(2)} = \langle \partial_j u_i \partial_i u_j \rangle = \langle \partial_i u_i \partial_j u_j \rangle = A_{iijj}^{(2)}, \quad (\text{B.2})$$

where repeated indices are summed over. For isotropic flows, the velocity-

gradient correlation tensor can be expressed as

$$A_{ijkl}^{(2)} = \alpha \delta_{ij} \delta_{kl} + \beta \delta_{ik} \delta_{jl} + \gamma \delta_{il} \delta_{jk}, \quad (\text{B.3})$$

with α , β , γ some constants and δ_{ij} indicating the Kronecker tensor. Using Eq. (B.3), one gets that $A_{ijji}^{(2)} = 2\alpha + 2\beta + 4\gamma$ and $A_{iijj}^{(2)} = 4\alpha + 2\beta + 2\gamma$, implying $\alpha = \gamma$ thanks to the constraint in Eq. (B.2). This last relation has the following important consequence:

$$\langle \partial_1 u_1 \partial_2 u_2 \rangle = A_{1122}^{(2)} = A_{1221}^{(2)} = \langle \partial_2 u_1 \partial_1 u_2 \rangle, \quad (\text{B.4})$$

since $A_{1122}^{(2)} = \alpha$ and $A_{1221}^{(2)} = \gamma$, from Eq. (B.3). Coming back to our original notation, this means that

$$\langle \partial_x u \partial_y v \rangle - \langle \partial_x v \partial_y u \rangle = 0. \quad (\text{B.5})$$

The above relation is very well verified in our numerical simulations for all Rossby numbers (Fig. B.1) and allows us to write the compressibility ratio as $\mathcal{C} = \langle \Delta^2 \rangle / (\langle \Delta^2 \rangle + \langle \zeta^2 \rangle)$, i.e. as in Eq. (5.8).

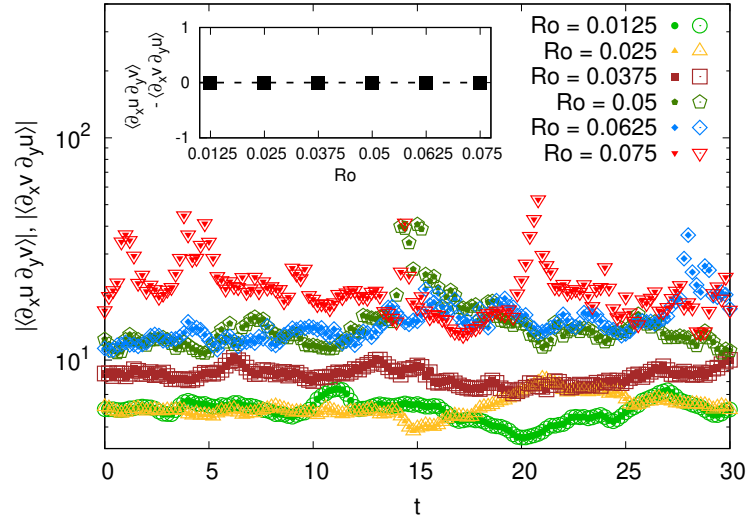


Figure B.1: Velocity-gradient correlations $\langle \partial_x u \partial_y v \rangle$ (filled points) and $\langle \partial_x v \partial_y u \rangle$ (empty points) as a function of time for the full SQG⁺¹ turbulent flow and different Rossby numbers (different point types). Inset: $\langle \partial_x u \partial_y v \rangle - \langle \partial_x v \partial_y u \rangle$, temporally averaged in the statistically steady state of the flow, as a function of the Rossby number.

Further Data and Figures

In this annex, we present supplementary figures that provide additional insights and support to the discussions and analyses detailed in the main chapters of this thesis. These figures are referenced within the main text but are included here to ensure the main manuscript remains concise and focused.

Figure C.1 presents the average Eulerian mean divergence conditionally averaged over vorticity and strain for $Ro = 0.0125$, $Ro = 0.0375$, $Ro = 0.05$, and $Ro = 0.075$. At the smallest Ro [panel (a)], the characteristic asymmetric and elongated, boomerang-like shape is not visible due to the low skewness of vorticity statistics (see inset of Fig. 4.3). As Ro increases, the boomerang shape becomes more pronounced. Across all Ro values, convergence is predominantly observed in cyclonic frontal regions. This figure also confirms that the averaged quantity exhibits the same features as those observed at a single time in Fig. 4.12a.

Figure C.2 presents the average Lagrangian mean divergence conditionally averaged over vorticity and strain for $Ro = 0.075$. This figure shows that the averaged quantity exhibits the same features as those observed at a single time in Fig. 4.12b.

Figure C.3 shows the energy spectra of the full, filtered, and SQG flows at all the Rossby numbers studied, ranging from 0.0125 to 0.075. The inset presents the spectra compensated by a power-law ($k^{-\beta}$) best fit. The spectral exponents are in the range $2.2 \lesssim \beta \lesssim 2.7$. At the smallest Rossby numbers, $Ro = 0.0125$ [panel (a)], 0.025 [panel (b)], and 0.0375 [panel (c)], the spectra overlap, indicating that Ro is too small to visibly affect the full flow in terms of kinetic energy spectra. At larger Ro , the differences between the three spectra become more pronounced, with the full and filtered flow spectra remaining more similar to each other than to the SQG flow. These differences increase as Ro grows.

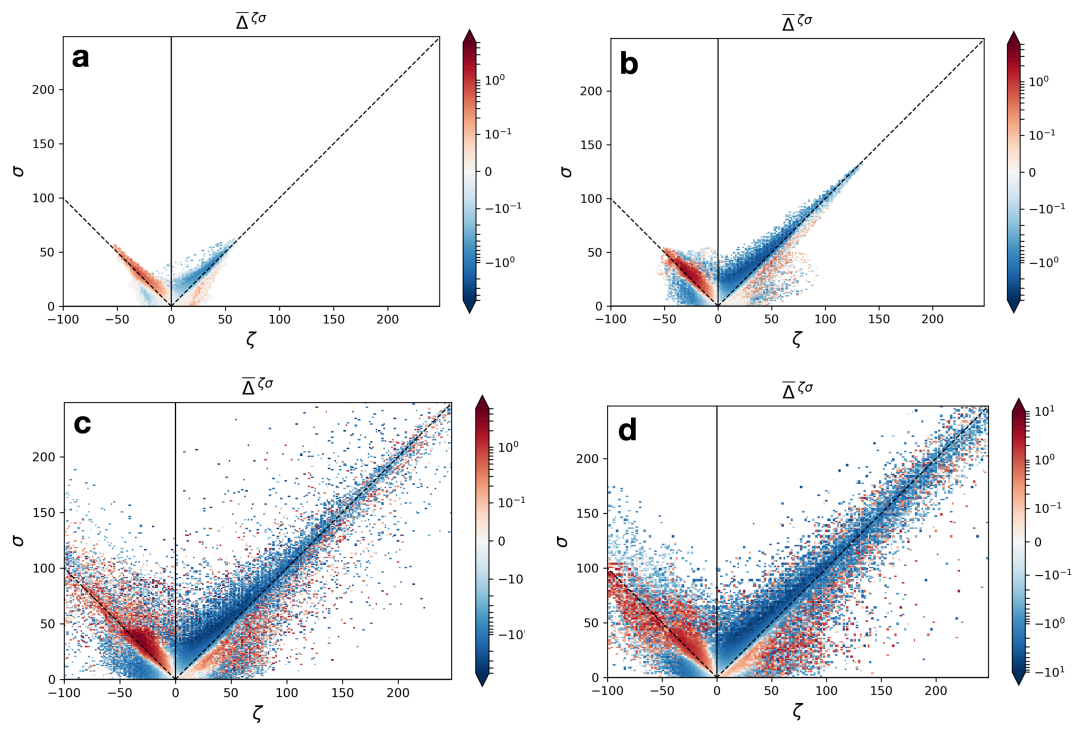


Figure C.1: Eulerian mean divergence $\overline{\Delta^{\zeta\sigma}}$ conditionally averaged over vorticity (ζ) and strain (σ), averaged over several flow realizations in statistically steady conditions, for $Ro = 0.0125$ (a), $Ro = 0.0375$ (b), $Ro = 0.05$ (c) and $Ro = 0.075$ (d).

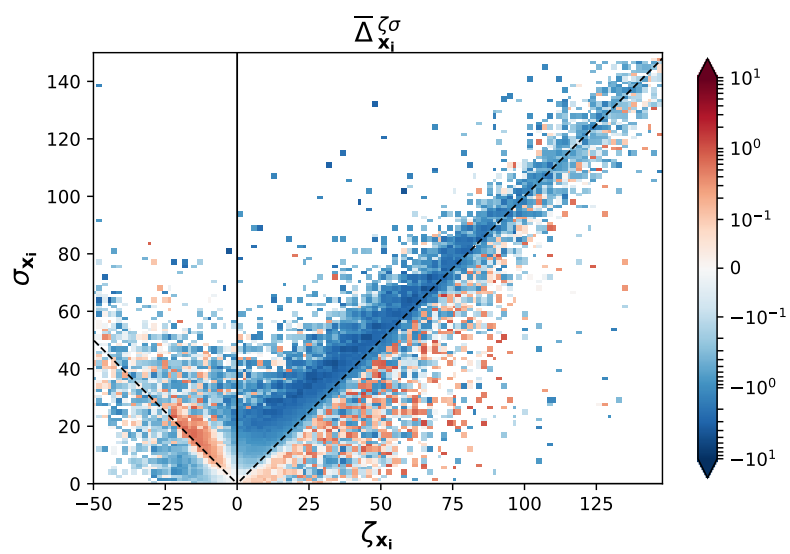


Figure C.2: Lagrangian Mean divergence $\bar{\Delta}_{x_i}^{\zeta\sigma}$ conditionally averaged over vorticity (ζ_{x_i}) and strain (σ_{x_i}) at particle positions x_i , averaged over several flow realizations in statistically steady conditions, for $Ro = 0.075$.

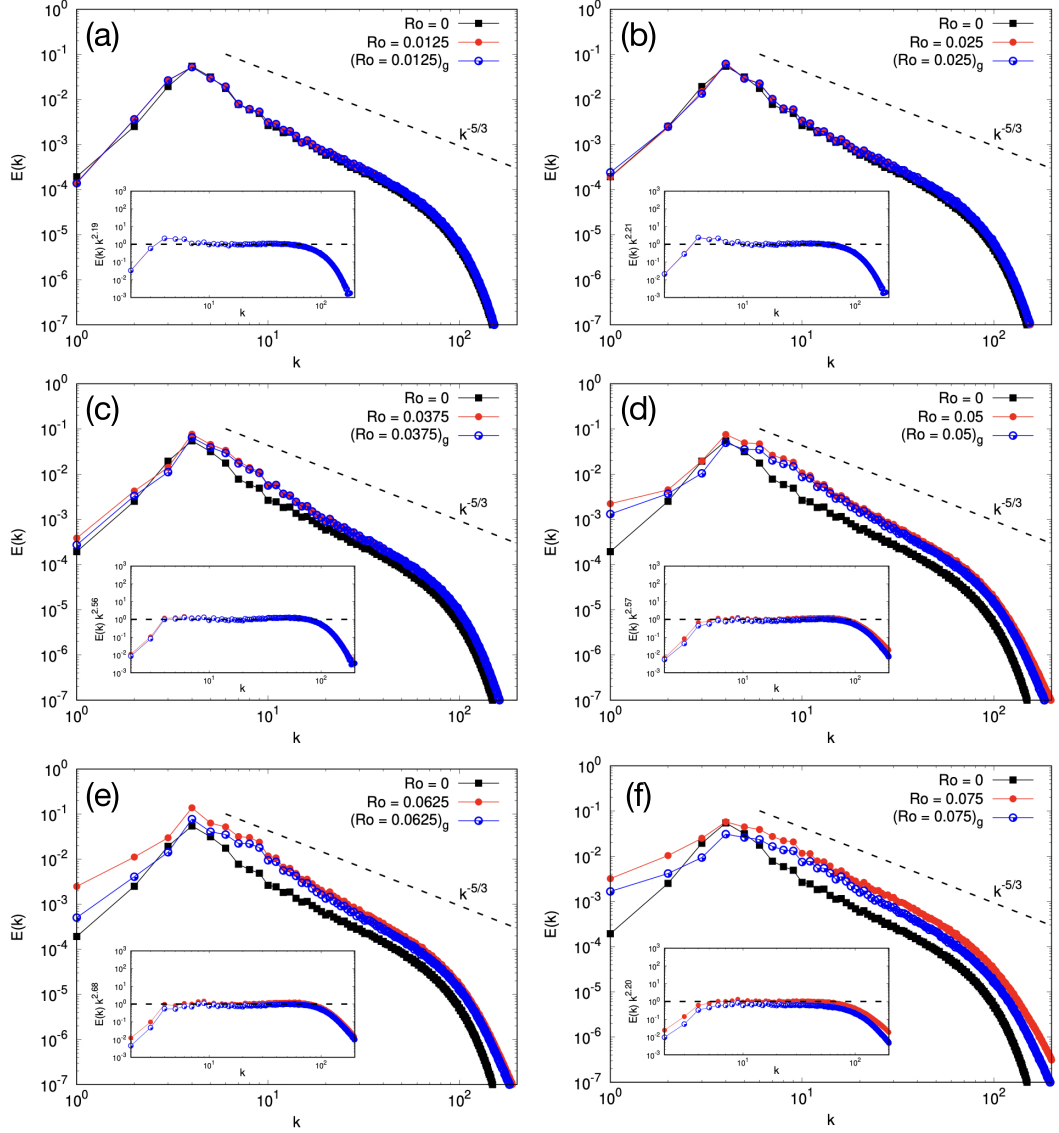


Figure C.3: Kinetic energy spectra temporally averaged over several flow realizations in the statistically steady state for SQG, SQG⁺¹ and (SQG⁺¹)_g (i.e., for the geostrophic component of the SQG⁺¹ simulation). Panels (a) to (f) show the spectra for Rossby numbers from 0.0125 to 0.075. The dashed black line corresponds to $k^{-5/3}$, the expected spectrum for SQG turbulence. Inset: the same spectra compensated by the best-fit power law $k^{-\beta}$ and rescaled with a coefficient such that the scaling range corresponds to the wavenumbers for which $E(k)k^\beta \simeq 1$

